

NOMENCLATURE

LATIN SYMBOLS

a	leaf area density	$\text{m}^2 \text{ m}^{-3}$
A	area	m^2
A_f	frontal area	m^2
A_L	net leaf area	m^2
A_n	assimilation rate	$\text{mol m}^{-2} \text{ s}^{-1}$
b	Vogel exponent	-
c_d	leaf drag coefficient	-
C_d	drag coefficient	-
c_p	specific heat (at constant pressure)	$\text{J kg}^{-1} \text{ K}^{-1}$
c_a^*	reference CO ₂ concentration	mol mol^{-1}
C	aerodynamic resistance coefficient	$\text{s}^{0.5} \text{ m}^{-1}$
$C_{o,a}$	oxygen concentration	mol mol^{-1}
D	diameter	m
D	vapor pressure deficit	kPa
D	vapor pressure deficit	$\text{Pa Pa}^{-1}, \text{ mol mol}^{-1}$
e_m	maximum quantum efficiency of the leaf	-
E	leaf transpiration flux	kg s^{-1}
f_c	CO ₂ assimilation (photosynthesis) rate	$\text{mol m}^{-2} \text{ s}^{-1}$
f_v	transpiration rate	$\text{mol m}^{-2} \text{ s}^{-1}$
F	force	N
F_d	drag force	N
g	gravitational acceleration	$\text{m}^2 \text{ s}^{-1}$
g_l	liquid water flux	$\text{kg m}^{-2} \text{ s}^{-1}$
g_v	water vapor flux	$\text{kg m}^{-2} \text{ s}^{-1}$
$g_{v,leaf}$	water vapor mass flux	$\text{kg m}^{-2} \text{ s}^{-1}$
$g_{v,root}$	root water uptake	$\text{kg m}^{-2} \text{ s}^{-1}$
$G_{v,root}$	net root water uptake	kg s^{-1}
$G_{v,xylem}$	net xylem water flux	kg s^{-1}
h	enthalpy	J kg^{-1}
$h_{c,h}$	convective heat transfer coefficient	$\text{W m}^{-2} \text{ K}^{-1}$

$h_{c,m}$	convective mass transfer coefficient	m s^{-1}
H	height	m
HU	Hounsfield units	-
I	turbulence intensity	%
k	turbulent kinetic energy	$\text{m}^2 \text{s}^{-2}$
k_{st}	stomatal conductance	$\text{mol m}^{-2} \text{s}^{-1}$
k_{st}^*	effective stomatal conductance	$\text{mol m}^{-2} \text{s}^{-1}$
K	permeability	m^2
K	hydraulic conductivity	m s^{-1}
K_{lp}	liquid water permeability	s
K_{vp}	water vapor permeability	s
K_{vT}	water vapor permeability due to temperature	s
K_c	Michaelis constant for CO_2	???
K_o	Michaelis constant for O_2	???
l	length	m
l	characteristic leaf size	m
\mathcal{L}	Lagrangian	-
L_v	latent heat of vaporization for water ($= 2.5 \times 10^6$)	J kg^{-1}
m	mass	kg
M	molar mass	kg mol^{-1}
M_a	molar mass of dry air ($= 0.028966$)	kg mol^{-1}
M_v	molar mass of water vapor ($= 0.01801534$)	kg mol^{-1}
n	Van Genuchten parameter	-
p_c	capillary pressure	Pa
p_l	liquid pressure	Pa
p_t	gas phase pressure	Pa
p_v	partial vapor pressure	Pa
$p_{v,i}$	intercellular vapor pressure	Pa
$p_{v,sat}$	saturation vapor pressure	Pa
P	pressure	Pa
Pr	Prandtl number	-
Fr_t	turbulent Prandtl number	-
\mathbf{q}	heat flux	W m^{-2}
$q_{lat,lat}$	latent heat flux from leaf	W m^{-2}
q_r	net radiative heat flux	W m^{-2}
$q_{r,sw}$	short-wave radiative heat flux	W m^{-2}
$q_{r,lw}$	long-wave radiative heat flux	W m^{-2}

$q_{rad,lat}$	radiative heat flux into leaf	W m^{-2}
$q_{sen,lat}$	sensible heat flux from leaf	W m^{-2}
Q_p	flux of incoming PAR	???
r	root area density	$\text{m}^2 \text{m}^{-3}$
r_a	aerodynamic resistance	s m^{-1}
r_s	stomatal resistance	s m^{-1}
R	universal gas constant ($= 8.3144598$)	$\text{J mol}^{-1} \text{K}^{-1}$
RAI	root area index	$\text{m}^2 \text{m}^{-2}$
Re	Reynolds number	-
R_v	specific gas constant of dry air ($= 287.042$)	$\text{J kg}^{-1} \text{K}^{-1}$
R_v	specific gas constant of water vapor ($= 461.524$)	$\text{J kg}^{-1} \text{K}^{-1}$
Sc_t	turbulent Schmidt number	-
s_e	volumetric TDR source	$\text{W m}^{-3} \text{s}^{-1}$
s_ρ	volumetric mass source	$\text{kg m}^{-3} \text{s}^{-1}$
s_k	volumetric TKE source	W m^{-3}
$s_{q,r}$	volumetric radiative source	W m^{-3}
s_r	volumetric root water uptake source	$\text{kg m}^{-3} \text{s}^{-1}$
s_T	volumetric temperature source	K m^{-3}
s_u	volumetric momentum source	N m^{-3}
s_w	volumetric humidity source	$\text{kg kg}^{-1} \text{s}^{-1}$
S_l	liquid saturation	-
t	time	s
T	temperature	K
T_g	ground temperature	K
T_L	leaf temperature	K
T_{sky}	sky temperature	K
TR	net hourly transpiration rate	g h^{-1}
u	velocity	m s^{-1}
u_*	friction velocity	m s^{-1}
U	mean wind speed	m s^{-1}
U_{ref}	reference velocity	m s^{-1}
$UTCI$	universal thermal climate index	$^{\circ}\text{C}$
V_{cmax}	maximum carboxylation capacity	???
w	moisture content	kg m^{-3}
w_a	dry air content	kg m^{-3}
w_{cap}	capillary moisture content	kg m^{-3}
w_l	liquid water content	kg m^{-3}

w_s	solid matrix water content	kg m^{-3}
w_v	water vapor content	kg m^{-3}
z	vertical height	m
z_0	aerodynamic roughness height	m

GREEK SYMBOLS

α	aerodynamic porosity	-
α^{2D}	2D aerodynamic porosity	-
α_p	leaf absorptivity of PAR	-
β	optical porosity	-
β	volumetric thermal expansion coefficient	K^{-1}
β_p	fraction of MKE converted to TKE	-
β_d	fraction of TKE shortcut to TDR	-
γ	apparent quantum yield	-
δ_v	water vapor diffusion coefficient	s
ε	turbulent kinetic energy dissipation rate	$\text{m}^2 \text{s}^{-3}$
κ	von Kármán constant ($= 0.41$)	-
λ	thermal conductivity	$\text{W m}^{-1} \text{K}^{-1}$
λ	Lagrange multiplier	mol mol^{-1}
μ	attenuation coefficient	m^{-1}
μ	chemical potential	J mol^{-1}
μ	dynamic viscosity	$\text{kg m}^{-1} \text{s}^{-1}$
ν	kinematic viscosity	$\text{m}^2 \text{s}^{-1}$
ν_t	turbulent viscosity	$\text{m}^2 \text{s}^{-1}$
ρ	density	kg m^{-3}
ρ_a	density of air	kg m^{-3}
ρ_l	density of liquid water ($= 1000$)	kg m^{-3}
ρ_s	density of solid matrix	kg m^{-3}
σ_v	Schmidt number	-
σ_{ν_t}	turbulent Schmidt number	-
ϕ_o	open porosity	$\text{m}^3 \text{m}^{-3}$
ψ	shelter parameter	-
ψ_g	gravitational potential	Pa
ψ_L	leaf water potential	Pa
ψ_R	root water potential	Pa

ψ_s	soil water potential	Pa
Ω	domain	-
Ω_a	air domain	-
Ω_s	soil domain	-

SUBSCRIPTS

eff	effective
g	gas
g	ground
i	intercellular
l	liquid (water)
lw	long-wave
L	leaf
o	open
$pore$	pore
ref	reference
$root$	root
sat	saturated
R	root
s	solid
s	soil
sky	sky
sw	short-wave
t	time
v	vapor
$xylem$	xylem

ACRONYMS

ABL	atmospheric boundary layer
CFD	computational fluid dynamics
CHTC	convective heat transfer coefficient
CMTA	convective mass transfer coefficient

CT	computational tomography
DEHS	Di-Ethyl-Hexyl-Sebacat
DIG	diagonal-based incomplete Cholesky
DNS	direct numerical simulation
ETHZ	Eidgenössische Technische Hochschule Zürich
FOV	field of view
FFT	fast Fourier transformation
FVM	finite volume method
HPC	high performance computing
LAI	leaf area index
LAI	leaf area density
LDPE	low-density Polyethylene
LES	large eddy simulation
LHS	left hand side
MOE	modulus of elasticity
PAR	photosynthetically active radiation
PCG	preconditioned conjugate gradient
PIV	particle image velocimetry
PPM	parts per million
RAI	root area index
REV	representative elementary volume
RANS	Reynolds-averaged Navier-Stokes
RHS	right hand side
ROI	region of interest
SPIV	stereoscopic particle image velocimetry
TDR	turbulent dissipation rate
TKE	turbulent kinetic energy
UHI	urban heat island

UTCI universal thermal climate index

WUE water use efficiency

CONTENTS

Nomenclature	i
1 Parametric study of impact of vegetation	1
1.1 Introduction	1
1.2 Generalized governing equation of moist flow	1
1.3 Turbulence modeling	3
1.4 Incompressible conservation equations of mean flow of moist air	3
1.5 Source terms for vegetation	5
1.6 Energy balance of a leaf	6
1.7 Radiation within vegetation	8
1.8 Numerical model	9
1.8.1 Simulation domain	9
1.8.2 Boundary conditions	10
1.8.3 Numerical solution procedure	11
1.9 Validation of vegetation model	12
1.10 Impact of row of trees on the microclimate	14
1.10.1 Impact on energy balance at the leaf surface	16
1.10.2 Influence of vegetation on the flow field	17
1.10.3 Transpirative cooling effect of a row of trees	17
1.11 Influence of environmental factors	23
1.11.1 Influence of wind speed	23
1.11.2 Influence of relative humidity and air temperature	25
1.11.3 Influence of solar radiation intensity	26
1.11.4 Summary on the impact of environmental factors	27
1.12 Influence of tree properties	28
1.12.1 Influence of leaf size	28
1.12.2 Influence of stomatal resistance	28
1.12.3 Influence of leaf area density	29
1.12.4 Summary on the influence of tree properties	29
1.13 Influence of vegetation size	30
1.13.1 Influence of number of tree rows	31
1.13.2 Influence of tree height	33
1.13.3 Summary on the influence of vegetation size	33
1.14 Conclusion	34
2 Comparison of wind tunnel measurement and CFD of a small plant	37
2.1 Simulation domain and boundary condition	37
2.1.1 Numerical domain	37
2.1.2 Boundary conditions	38
2.1.3 Leaf area density	39
2.1.4 Numerical solution	39

2.2	Isothermal case	40
2.2.1	Influence of heterogeneity in leaf area density distribution	42
2.2.2	Influence of plant drag coefficient	44
2.2.3	Influence of turbulence model	44
2.3	Non-isothermal case	47
3	Numerical model for modeling vegetation in urban area	51
3.1	Introduction	51
3.2	Governing equations of coupled heat and moisture transport	51
3.2.1	Composition of the porous material	51
3.2.2	Water potential	52
3.2.3	Coupled transport of heat and mass	53
3.2.4	Linearized heat and mass transport equation	55
3.3	Soil-Plant-Atmospheric Continuum	57
3.3.1	Water transport in soil-root system	57
3.3.2	Water transport in xylem-leaf system	58
3.3.3	Water transport from leaf to air	59
3.3.4	Improved stomatal model	60
3.3.5	Marginal water use	64
3.3.6	Numerical method for determining leaf water potential	65
3.3.7	Solution strategy for coupling	65
	Bibliography	69

1

PARAMETRIC STUDY OF IMPACT OF VEGETATION

This chapter is based on paper Manickathan et al. (2018).

1.1 INTRODUCTION

In this chapter, a parametric study of the influence of environmental factors and tree properties on the transpirative cooling effect of a single row of trees is presented. The environmental factors investigated are wind speed, relative humidity, air temperature and solar radiation. The tree properties investigated are stomatal resistance, leaf size and leaf area density. In addition, the influence of vegetation size in the domain is studied by varying tree height and number of tree rows. The study aims at answering the following key questions: How does the climate influence the transpirative cooling effect of a single row of trees? Which features of the trees improve its cooling performance? Does increasing the size of the vegetated volume consistently improve the cooling of the environment? These findings can then assist in developing specific guidelines for effective UHI mitigation measures. To the author's knowledge, few rigorous studies have been performed to investigate the cooling effect of individual trees.

1.2 GENERALIZED GOVERNING EQUATION OF MOIST FLOW

The governing equation consists of conservation of mass, momentum, energy and species. The conservation equations are given in differential form in a Cartesian coordinate system described by the triplet $\mathbf{x} = (x, y, z)$. The conservation of mass for compressible moist flow is given as:

$$\frac{\partial \rho}{\partial t} + \nabla \cdot (\rho \mathbf{u}) = 0 \quad (1.1)$$

where ρ is the fluid density (kg m^{-3}), and $\mathbf{u} = (u, v, w)$ is the fluid velocity (m s^{-1}). A detailed derivation is given in appendix ?? and ??.

The conservation of momentum is given as:

$$\frac{\partial \rho \mathbf{u}}{\partial t} + \nabla \cdot (\rho \mathbf{u} \mathbf{u}) = -\nabla p + \mu \nabla^2 \mathbf{u} + \rho \mathbf{g} + \mathbf{s}_u \quad (1.2)$$

where p is the pressure (Pa), μ the dynamic viscosity ($\text{kg m}^{-1} \text{s}^{-1}$), \mathbf{g} the gravitational acceleration (m s^{-2}). The source of momentum \mathbf{s}_u is:

$$\mathbf{s}_u = -\rho a c_d |\mathbf{u}| \mathbf{u} \quad (1.3)$$

where a is the leaf area density ($\text{m}^2 \text{m}^{-3}$), and c_d is the leaf drag coefficient ($c_d = 0.2$).

The conservation of energy is given as:

$$\frac{\partial \rho h}{\partial t} + \nabla \cdot (\rho h \mathbf{u}) = -\nabla \cdot \mathbf{q} + s_h \quad (1.4)$$

where

$$\mathbf{q} = -\lambda \nabla T \quad (1.5)$$

is the Fourier's law of heat conduction, with:

$$\mathbf{q} = -\frac{c_p \mu}{\text{Pr}} \nabla T \quad (1.6)$$

The conservation of species i is given as:

$$\frac{\partial \rho x_i}{\partial t} + \nabla \cdot (\rho x_i \mathbf{u}) = \nabla \cdot \mathbf{g}_i + s_i \quad (1.7)$$

where x_i is the concentration of species i , \mathbf{g}_i is the flux of species, and s_i is the source term.

Assumption: We assume that moist air is composed of dry air and water vapor.

The mass fraction of each component is:

$$x_a = \frac{\rho_a}{\rho} \quad (1.8)$$

and

$$x_v = \frac{\rho_v}{\rho} \quad (1.9)$$

where ρ_a and ρ_v are partial density of dry air and water vapour (kg m^{-3}) and ρ is density of gas mixture and results in:

$$x_a + x_v = 1 \quad (1.10)$$

and

$$\rho_a + \rho_v = \rho \quad (1.11)$$

The enthalphy of dry air and water vapor are:

$$h_a = c_{p,a} (T - T_{ref}) \quad (1.12)$$

and

$$h_v = c_{p,v} (T - T_{ref}) + L_v (x_v - x_{v,ref}) \quad (1.13)$$

The total enthalpy of moist air is:

$$h = h_a \cdot x_a + h_v \cdot x_v \quad (1.14)$$

and so:

$$\rho h = \rho_a c_{p,a} (T - T_{ref}) + \rho_v c_{p,v} (T - T_{ref}) + \rho_v L_v \quad (1.15)$$

1.3 TURBULENCE MODELING

The Reynolds decomposition splits the instantaneous velocity into mean and fluctuating component:

$$\mathbf{u}(\mathbf{x}, t) = \bar{\mathbf{u}}(\mathbf{x}) + \mathbf{u}'(\mathbf{x}, t). \quad (1.16)$$

Applying this averaging operator to the NS equations, resulting Reynolds-Averaged Navier-Stokes (RANS) equation is given as:

$$\frac{\partial \bar{\rho}}{\partial t} + \nabla \cdot (\bar{\rho} \bar{\mathbf{u}}) = 0, \quad (1.17)$$

$$\frac{\partial \bar{\rho} \bar{\mathbf{u}}}{\partial t} + \nabla \cdot (\bar{\rho} \bar{\mathbf{u}} \bar{\mathbf{u}}) = -\nabla \bar{p} + \mu \nabla^2 \bar{\mathbf{u}} - \nabla \cdot (\bar{\rho} \mathbf{u}' \mathbf{u}') + \rho \mathbf{g} + s_u \quad (1.18)$$

where $\bar{\rho} \mathbf{u}' \mathbf{u}'$ is the Reynolds stresses. The Reynolds stresses are modelled using Boussinesq eddy-viscosity assumption:

$$-\bar{\rho} \mathbf{u}' \mathbf{u}' = \mu_t (\nabla \mathbf{u} + \nabla \mathbf{u}^T) - \frac{2}{3} \rho k \mathbf{I} \quad (1.19)$$

where:

$$\mu_t = \rho C_\mu \frac{k^2}{\epsilon} \quad (1.20)$$

1.4 INCOMPRESSIBLE CONSERVATION EQUATIONS OF MEAN FLOW OF MOIST AIR

A computation fluid dynamics (CFD) model is used to determine the interaction between the environment and vegetation. The mean flow of moist air is modeled using the Reynolds-averaged Navier-Stokes (RANS) equations, where vegetation is modeled as porous media. The mean flow of humid air (i.e. binary mixture of water vapour and dry air) through and around vegetation is modeled using Reynolds-averaged Navier-Stokes (RANS) equations with the realizable $k - \epsilon$ turbulence closure model. Wilson and Shaw (1977) developed a mathematical model for turbulent airflow around tree canopies with closure for mean momentum, turbulent kinetic energy (TKE) and turbulent dissipation rate (TDR). Using this approach, vegetation is modeled as a porous medium, where the impact of vegetation on airflow is modeled using source terms in the conservation equations. The buoyancy force is also taken into account where the Boussinesq

approximation is used for air density variations. The equations consist of conservation of mass, momentum, temperature, humidity and the turbulence model, respectively:

$$\nabla \cdot \bar{\mathbf{u}} = s_\rho, \quad (1.21)$$

$$\frac{\partial \bar{\mathbf{u}}}{\partial t} + \bar{\mathbf{u}} \cdot \nabla \bar{\mathbf{u}} = -\frac{1}{\rho} \nabla \bar{P} + \nabla \cdot [2(v + v_t) \mathbf{S}] - \frac{2}{3} \nabla k - g\beta (\bar{T} - \bar{T}_0) + \frac{1}{\rho} s_u, \quad (1.22)$$

$$\frac{\partial \bar{T}}{\partial t} + \bar{\mathbf{u}} \cdot \nabla \bar{T} = \nabla \cdot \left[\left(\frac{v}{Pr} + \frac{v_t}{Pr_t} \right) \nabla \bar{T} \right] + s_T, \quad (1.23)$$

$$\frac{\partial \bar{w}}{\partial t} + \bar{\mathbf{u}} \cdot \nabla \bar{w} = \nabla \cdot \left[\left(\frac{v}{\sigma_v} + \frac{v_t}{\sigma_{v_t}} \right) \nabla \bar{w} \right] + s_w, \quad (1.24)$$

$$\frac{\partial k}{\partial t} + \bar{\mathbf{u}} \cdot \nabla k = \nabla \cdot \left[\left(v + \frac{v_t}{\sigma_k} \right) \nabla k \right] + P_k - \varepsilon + \frac{1}{\rho} s_k, \quad (1.25)$$

$$\frac{\partial \varepsilon}{\partial t} + \bar{\mathbf{u}} \cdot \nabla \varepsilon = \nabla \cdot \left[\left(v + \frac{v_t}{\sigma_\varepsilon} \right) \nabla \varepsilon \right] + C_{1\varepsilon} P_k \frac{\varepsilon}{k} - C_{2\varepsilon} \frac{\varepsilon^2}{k + \sqrt{v\varepsilon}} + \frac{1}{\rho} s_\varepsilon, \quad (1.26)$$

where $\bar{\mathbf{u}}$ (m s^{-1}) is the mean velocity, \bar{P} (Pa) the mean hydrostatic pressure, \bar{T} (K) the mean air temperature, \bar{w} (kg kg^{-1}) the mean humidity ratio (i.e. the ratio of water vapor mass to dry air mass), k ($\text{m}^2 \text{s}^{-2}$) the turbulent kinetic energy (TKE) and ε ($\text{m}^2 \text{s}^{-3}$) the TKE dissipation rate (TDR). The Reynolds stresses are closed using Boussinesq eddy-viscosity assumption,

$$v_t = C_\mu \frac{k^2}{\varepsilon} \quad (1.27)$$

where the turbulent viscosity is closed using realizable $k - \varepsilon$ turbulence model. The mean strain-rate \mathbf{S} is defined as

$$\mathbf{S} = \frac{1}{2} (\nabla \bar{\mathbf{u}} + \nabla \bar{\mathbf{u}}^T) \quad (1.28)$$

and

$$P_k = 2v_t |\mathbf{S}|^2 \quad (1.29)$$

is the TKE production rate. The environmental constants are the density of air $\rho = 1.225 \text{ kg m}^{-3}$, the kinematic viscosity of air $v = 1.45 \times 10^{-5} \text{ m}^2 \text{s}^{-1}$, the gravitational acceleration $\mathbf{g} = (0, 0, -9.81)^T \text{ m s}^{-2}$, the thermal expansion coefficient $\beta = 3 \times 10^{-3} \text{ K}^{-1}$ and the specific heat capacity of air $c_p = 1003.5 \text{ J kg}^{-1} \text{ K}^{-1}$. The Prandtl number, Schmidt number, turbulent Prandtl number, turbulent Schmidt number are $Pr = 0.9$, $\sigma_v = 0.9$, $Pr_t = 0.7$ and $\sigma_{v_t} = 0.7$, respectively. The turbulence model constants are $C_{2\varepsilon} = 1.92$, $\sigma_k = 1.0$ and $\sigma_\varepsilon = 1.2$. The remaining coefficients C_μ and $C_{1\varepsilon}$ in the realizable $k - \varepsilon$ model are determined from velocity gradients and TKE production-dissipation ratio (Shih et al. 1995). Vegetation introduces the source for mass s_ρ , momentum s_u , temperature s_T , humidity ratio s_w , TKE s_k and TDR s_ε in the conservation equations.

1.5 SOURCE TERMS FOR VEGETATION

Vegetation is also discretized into finite volumes, where the leaf area density a ($\text{m}^2 \text{ m}^{-3}$), defined as the one-sided leaf surface area in a given volume, quantifies the spatial distribution of the vegetation in the environment. In literature, a is reported to range from 0.35 to $35 \text{ m}^2 \text{ m}^{-3}$ (Kenjereš and Ter Kuile 2013; Liang et al. 2006). The source terms in the conservation equations, Eqs. (1.21) to (1.26), describe the influence of vegetation on the different aspects of air motion. The source of mass in the air due to vegetation s_ρ ($\text{kg m}^{-3} \text{ s}^{-1}$) is:

$$s_\rho = a g_{v,leaf} \quad (1.30)$$

where $g_{v,leaf}$ ($\text{kg m}^{-2} \text{ s}^{-1}$) is the water vapor mass flux from the leaf into the air (Hiraoka 2005). The momentum source term s_u (N m^{-3}) is given as:

$$s_u = -\rho c_d a |\bar{\mathbf{u}}| \bar{\mathbf{u}} \quad (1.31)$$

where $c_d = 0.2$ is the leaf drag coefficient (Wilson and Shaw 1977). For turbulent flows, the viscous drag can be assumed to be negligible compared to the form drag (Judd et al. 1996; Li et al. 1990; Liu et al. 1996). Furthermore, the momentum exerted by transpiration is also assumed to be negligible compared to the vegetation drag force (Hiraoka 2005). Therefore, the momentum transport equation can be solved using the divergence-free constraint, $\nabla \cdot \bar{\mathbf{u}} = 0$. The temperature source term s_T (K s^{-1}) is given as:

$$s_T = a \frac{q_{sen,leaf}}{\rho c_p} \quad (1.32)$$

where $q_{sen,leaf}$ (W m^{-2}) is the sensible heat flux from the leaf into the air (Bruse and Fleer 1998; Hiraoka 2005). The sensible heat exchange between water vapor and air is assumed negligible compared to the sensible heat exchange between the leaf and the air. Furthermore, the latent heat flux from the leaves does not directly change the air temperature but it results in cooling of leaf which in turn causes the change in air temperature by sensible heat (Hiraoka 2005). The humidity ratio source term s_w ($\text{kg kg}^{-1} \text{ s}^{-1}$) is given as:

$$s_w = a \frac{g_{v,leaf}}{\rho} \quad (1.33)$$

In the present study we use a realizable $k - \epsilon$ turbulence closure model for the Reynolds stresses. The TKE source s_k (W m^{-3}) is given as:

$$s_k = \rho c_d a \left(\beta_p |\bar{\mathbf{u}}|^3 - \beta_d |\bar{\mathbf{u}}| k \right) \quad (1.34)$$

and the TDR source term s_ϵ ($\text{W m}^{-3} \text{ s}^{-1}$) is given as:

$$s_\epsilon = \rho c_d a \left(\beta_p C_{4\epsilon} |\bar{\mathbf{u}}|^3 \frac{\epsilon}{k} - \beta_d C_{5\epsilon} |\bar{\mathbf{u}}| \epsilon \right) \quad (1.35)$$

with model constants $C_{4\epsilon} = 0.9$ and $C_{5\epsilon} = 0.9$ (Katul, Mahrt, et al. 2004; Kenjereš and Ter Kuile 2013; Sanz 2003). The constants $\beta_p = 1.0$ is the fraction of mean kinetic energy converted into

turbulent kinetic energy and $\beta_d = 5.1$ describes the reduction in TKE and TDR due to vegetation (Sanz 2003). Kenjereš and Ter Kuile (2013) compared various RANS model coefficients for vegetation in an urban area and found the coefficients provided by Katul, Mahrt, et al. (2004) to be reasonably accurate and the coefficients show good numerical stability. Therefore, these parameters are used in the present study.

1.6 ENERGY BALANCE OF A LEAF

The heat and mass exchanges between the tree canopy and the air are simulated using a leaf energy model. The heat and mass exchanges between the tree canopy and the air are simulated using a leaf energy balance as shown in Fig. 1.1. We assume a stationary leaf energy balance and that the dynamic thermal storage of heat in leaves can be neglected.

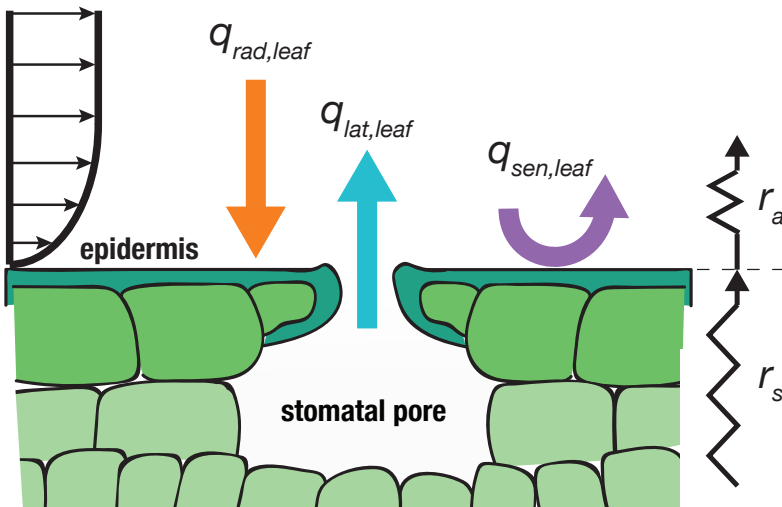


Figure 1.1: Schematic representation of leaf surface with energy balance as given by Eq. (1.36). The radiative flux $q_{rad,leaf}$ absorbed by the leaf is balanced by the sensible $q_{sen,leaf}$ and the latent heat flux $q_{lat,leaf}$ leaving the leaf surface. The stomatal resistance r_s influences the latent heat flux and the aerodynamic resistance r_a influences both the sensible and the latent heat fluxes.

The stationary energy balance is given as:

$$q_{rad,leaf} - q_{lat,leaf} - q_{sen,leaf} = 0 \quad (1.36)$$

where $q_{rad,leaf}$ (W m^{-2}) is the radiative flux, $q_{sen,leaf}$ (W m^{-2}) is the sensible heat flux and $q_{lat,leaf}$ (W m^{-2}) is the latent heat flux (Bruse and Fleer 1998; Dauzat et al. 2001; Hiraoka 2005; Majdoubi et al. 2009). Positive sensible and latent heat fluxes are defined as heat transfer from the

leaf into the air. The sensible heat flux due to convective heat transfer from leaf surface to the air is given as:

$$q_{sen,leaf} = h_{c,h} (T_{leaf} - T) = \frac{2\rho c_p}{r_a} (T_{leaf} - T) \quad (1.37)$$

where $h_{c,h}$ ($\text{W m}^{-2} \text{K}^{-1}$) is the convective heat transfer coefficient (CHTC), T_{leaf} (K) is the leaf surface temperature, T (K) is the air temperature and r_a (s m^{-1}) is the aerodynamic resistance of the boundary layer around the leaf. A factor 2 is present in the equation as the sensible heat flux occurs on both sides of the leaf. The aerodynamic resistance r_a (s m^{-1}) is given as (Dauzat et al. 2001; Robitu et al. 2006):

$$r_a = C \left(\frac{l}{|\bar{u}|} \right)^{1/2} \quad (1.38)$$

where $C = 130 \text{ s}^{0.5} \text{ m}^{-1}$ is the proportionality factor and l (m) is the characteristic leaf size ranging from 0.02 m for conifers and up to 0.5 m for tropical plants (Bruse and Fleer 1998). The latent heat flux from leaf to air due to transpiration is defined as:

$$q_{lat,leaf} = L_v g_{v,leaf} \quad (1.39)$$

where $L_v = 2.5 \times 10^6 \text{ J kg}^{-1}$ is latent heat of vaporization. The water vapor mass flux $g_{v,leaf}$ from leaf into the air is given as:

$$g_{v,leaf} = h_{c,m} (p_{v,leaf} - p_v) = \frac{\rho R_a}{p R_v} \frac{1}{r_a + r_s} (p_{v,leaf} - p_v) \quad (1.40)$$

where $h_{c,m}$ (s m^{-1}) is the convective mass transfer coefficient (CMTC), $p_{v,leaf}$ [Pa] is the vapor pressure at the leaf, p_v (Pa) is the vapor pressure of the air above the leaf boundary layer, r_s (s m^{-1}) is the stomatal resistance and $R_a = 287.042 \text{ J kg}^{-1} \text{ K}^{-1}$ and $R_v = 461.524 \text{ J kg}^{-1} \text{ K}^{-1}$ are the gas constants of dry air and water vapor, respectively. In the present study, we assume that there is no condensation or rain on the leaf surface and so evapotranspiration is only due to transpiration through the leaf stomata. Therefore, the vapor pressure at the leaf is the vapour pressure within the leaf stomata which is close to the saturation vapor pressure at the leaf temperature, thereby we can assume

$$p_{v,leaf} = p_{vsat,stom} (T_{leaf}) \quad (1.41)$$

The additional resistance r_s is due to the stomatal regulatory control of the leaf. In the present study, the stomatal resistance is modeled as a function of climatic conditions: $q_{r,sw}$ the short-wave radiative flux in the air and D (kPa) the vapor pressure deficit in the air, the difference between the saturation vapor pressure and the vapor pressure of the air

$$D \equiv p_{vsat} - p_v \quad (1.42)$$

The stomatal resistance is given as:

$$r_s = r_{s,min} f_1(q_{r,sw}) f_2(D) \quad (1.43)$$

where $r_{s,min}$ (s m^{-1}) is the minimal stomatal resistance and

$$f_1 = \frac{a_1 + q_{r,sw}}{a_1 + q_{r,sw}} \quad (1.44)$$

$$f_2 = 1 + a_3(D - D_0)^2 \quad (1.45)$$

are multiplicative functions describing the stomatal resistance change due to short-wave radiation and vapor pressure deficit in the air, respectively. The constants of the empirical functions are $a_1 = 169 \text{ W m}^{-2}$, $a_2 = 18 \text{ W m}^{-2}$, $a_3 = 0.005 \text{ kPa}^{-2}$ and $D_0 = 1.2 \text{ kPa}$ (Kichah et al. 2012). The minimum stomatal resistance $r_{s,min}$, the resistance when the stomata are fully open, depends on the plant type: e.g. 150 s m^{-1} for impatiens, 200 s m^{-1} for grass, 400 s m^{-1} for gloxinia and deciduous plants (Baille et al. 1994; Bruse and Fleer 1998). It must be noted that various other models exist in literature for the stomatal resistance and an overview is given by Damour et al. (2010). The present model is chosen as it is a simple model which can be used to consider the influence of environmental conditions. The energy balance (Eq. (1.36)) is solved once the leaf surface temperature T_{leaf} is known. Combining Eqs. (1.36), (1.37) and (1.39), the leaf temperature is given as:

$$T_{leaf} = T + \frac{q_{rad,leaf} - q_{lat,leaf}}{h_{c,h}} \quad (1.46)$$

where the equation is solved iteratively as $q_{lat,leaf}$ is dependent on the leaf temperature.

1.7 RADIATION WITHIN VEGETATION

The net radiative flux field q_r (W m^{-2}) in the air domain is the sum of short-wave and long-wave radiative fluxes:

$$q_r = q_{r,sw} + q_{r,lw} \quad (1.47)$$

where $q_{r,sw}$ (W m^{-2}) is the short-wave radiative flux and $q_{r,lw}$ (W m^{-2}) is the long-wave radiative flux. The source or sink of the radiative flux in the air is equal to the divergence of the net radiative flux:

$$\nabla \cdot q_r = \nabla \cdot q_{r,sw} + \nabla \cdot q_{r,lw} \quad (1.48)$$

and is due to the absorption and emission of radiation by the equivalent leaf area of the vegetation:

$$s_{q,r} = a q_{rad,leaf} \quad (1.49)$$

where $q_{rad,leaf}$ (W m^{-2}) is the net radiative flux at the leaf surface. Substituting Eqs. (1.47) and (1.48) into Eq. (1.49), we can determine the net radiative flux absorbed by the leaf:

$$q_{rad,leaf} = \frac{\nabla \cdot q_{r,sw} + \nabla \cdot q_{r,lw}}{a} \quad (1.50)$$

In this study, we simplify the formulation of radiation within vegetation according to the studies of plants in greenhouses (Boulard and Wang 2002; Fatnassi et al. 2006; Kichah et al. 2012; Majdoubi et al. 2009). The approach employs a simplified empirical formulation of radiation distribution within vegetation. The advantage of this approach is that radiation within vegetation

can be determined with a very low computational expense while providing sufficient accuracy. Such an approach is ideal for a parametric study on the dominant factors driving the transpirative cooling effect of vegetation. However, the downside of the model is that the long-wave radiation exchanges between surroundings cannot be evaluated.

The short-wave radiative flux $q_{r,sw}$ within a vegetation volume is determined using Beer-Lambert law:

$$q_{r,sw}(z) = q_{r,sw,0} \exp \left\{ -\beta \int_z^H a(z) dz \right\} \quad (1.51)$$

where $q_{r,sw,0}$ (W m^{-2}) is the short-wave radiative flux hitting the top of the vegetation and $\beta = 0.78$ is the extinction coefficient for short-wave radiation. The integral defines the net density of leaves that is present from the top of the vegetation canopy to the height where the short-wave radiative flux is evaluated. The simplification we consider in this study is that the sun is positioned directly above vegetation, i.e. mid-day condition with a solar altitude $\phi = 90^\circ$. A model with varying solar conditions is part of future research. The long-wave radiative flux is modelled empirically, as a function of the downward long-wave radiative flux, i.e. from the sky. It is given by:

$$\nabla \cdot q_{r,lw} = C_{lw} \frac{q_{r,lw,\downarrow}}{H} \quad (1.52)$$

where $C_{lw} = 0.04$ is an empirical constant for quantifying the net absorption of long-wave radiation (Kichah et al. 2012). Using this approach, the thermal emission of the leaves can be empirically modeled. The downward long-wave radiative flux is taken to be the long-wave radiative flux from sky, i.e. $q_{r,lw,\downarrow}$ with a sky temperature of $T_{sky} = 15^\circ\text{C}$ (Saneinejad et al. 2014).

1.8 NUMERICAL MODEL

The vegetation model, described in Sections 1.4 to 1.7, is implemented into the OpenFOAM finite volume solver (Weller et al. 1998). The steady-state velocity field is solved using the SIMPLE pressure-velocity coupling algorithm. A second-order central difference scheme is used for the gradient operator and a second-order linear upwind differencing scheme for the convective terms. The convergence criterion for the residuals is set to 10^{-8} based on sensitivity analysis. The computational domain size and the numerical scheme are chosen based on CFD best practices (Blocken 2015; Franke et al. 2007; Tominaga et al. 2008).

1.8.1 *Simulation domain*

The simulation of single row of trees is represented by a 2D porous domain ($x \times z$ axis) consisting of a $1 \times 1 \text{ m}^2$ ($x \times z$ axis) porous vegetation region as shown in Fig. 1.2, while infinitely long in the y -direction, where the source terms (Eqs. (1.30) to (1.35)) are non-zero. The computational domain is $35 \times 11.5 \text{ m}^2$ ($x \times z$ axis) and the mesh resolution is determined by performing a grid sensitivity analysis. The domain is discretized into a regular grid with 40 000 rectangular cuboidal cells. The smallest cell is at the edge of the tree row ($\Delta x = \Delta z = 0.01 \text{ m}$) and the expansion ratio to the outflow, inlet, ground and top boundaries are 1.05, 1.05, 1.05, and 1.15, respectively.

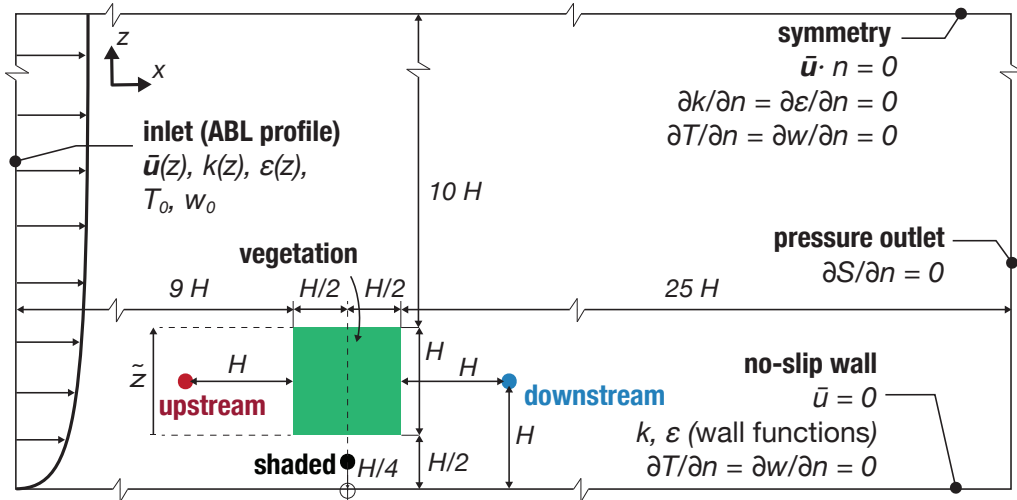


Figure 1.2: Simulation domain of the reference case with $H = 1$ m with description of the domain and the boundary conditions. The porous vegetation region is indicated in green (■) where leaf area density $a = 10 \text{ m}^2 \text{ m}^{-3}$ and zero everywhere else. The red point (●) indicate the upstream ($x = -1.5H, y = H$), blue (●) indicate the downstream ($x = 1.5H, y = H$), and black (●) indicate the shaded ($x = 0, y = H/4$) data sampling location.

The environmental factors that are varied for the parametric study are wind speed, ambient air temperature, relative humidity (RH) and solar radiation intensity. The environmental factors are tabulated in Table 1.1. Similarly, the properties of the vegetation are tabulated in `creftab:plantcond` and the parameters that are varied are leaf area density, stomatal resistance, leaf size, tree height and number of tree rows, which are presumed to have an influence on the transpirative cooling effect of vegetation. The upper and lower bounds of the parameters are chosen based on values from literature. The reference tree is chosen to be a densely foliated garden hedgerow in a midday conditions.

1.8.2 Boundary conditions

An atmospheric boundary layer (ABL) profile is prescribed at the inlet (Richards and Hoxey 1993):

$$\bar{u}(z) = \frac{u_*}{\kappa} \ln \left(\frac{z + z_0}{z_0} \right) \quad (1.53)$$

$$k = \frac{u_*^2}{\sqrt{C_\mu}} \quad (1.54)$$

$$\varepsilon = \frac{u_*^3}{\kappa(z + z_0)} \quad (1.55)$$

Table 1.1: Environmental factors varied in the parametric study

Parameter	Range	Reference
Solar radiation, $q_{r,sw,0}$	[100, 400, 800, 1000]	800
Wind speed, U_{ref}	[0.1, 0.25, 0.5, 0.75, 1, 2, 3, 5]	1
Air temperature, T_0	[20, 30]	30
Relative humidity, RH	[20, 30, 40, 50, 60, 70, 80]	60

Table 1.2: Plant properties varied in the parametric study

Parameter	Range	Reference
Leaf area density, a	[1, 3, 5, 7, 10]	10
Wind speed, $r_{s,min}$	[50, 100, 125, 150, 175, 200, 250, 300]	150
Leaf size, l	[0.01, 0.05, 0.1, 0.2, 0.3, 0.4]	0.1
Tree height, nH	[1, 2, 3, 5, 10]	1
\mathcal{N}^o of tree rows, n	[1, 2, 5, 10]	1

where $\bar{u}(z)$ (m s^{-1}) is the horizontal inlet velocity at height z , u_* (m s^{-1}) is the friction velocity, $\kappa = 0.41$ is von Kármán constant, $z_0 = 0.0217$ m is the aerodynamic roughness height and $C_\mu = 0.09$. The inlet boundary conditions for air temperature T and humidity ratio w are for simplicity uniform profiles, $T(z) = T_0$ and $w(z) = w_0$ and varied individually during the parametric study as tabulated in Table 1.1.

The ground is modeled using standard wall functions and is considered to be adiabatic. This ensures that the thermal influence of the ground is not present when measuring the cooling effect of vegetation on air. Even though, in reality, the thermal influence of the ground on the air temperature is an important factor, in the present study this simplification was chosen to isolate the influence of transpirative cooling of vegetation. A zero normal gradient boundary condition is applied for the humidity ratio. At the top, a slip velocity boundary condition is used and the temperature and humidity ratio are prescribed a zero normal gradient boundary condition. The outlet of the domain is set to a pressure outlet. The boundary conditions for T and w at outlet are zero normal gradient boundary conditions.

1.8.3 Numerical solution procedure

In the present study, the following strategy is used for solving the coupled vegetation-air problem:

1. Solve the energy balance at the leaf surface:
 - a) Determine the radiative flux $q_{rad,leaf}$ using Eq. (1.50).
 - b) Calculate the stomatal and aerodynamic resistances r_a and r_s using Eq. (1.38) and Eq. (1.43), respectively.

- c) Perform an initial estimate of leaf temperature $T_{leaf} = T$.
 - d) Calculate the saturated vapor pressure at the leaf surface $p_{vsat,leaf} = f(T_{leaf})$.
 - e) Calculate the latent heat flux $q_{lat,leaf}$ using Eq. (1.39).
 - f) Correct the leaf temperature T_{leaf} using Eq. (1.46).
 - g) Repeat steps (d) to (f) until the leaf temperature has converged with a convergence criterion of 10^{-8} .
2. Calculate all vegetation source terms s_ρ , s_u , s_T , s_w , s_k and s_e using Eqs. (1.30) to (1.35).
 3. Solve for the steady-state flow field, Eqs. (1.21) to (1.26).
 4. Repeat steps (1) to (3) until residuals of Eqs. (1.21) to (1.26) have reached the convergence limit of 10^{-8} .

The algorithm of the vegetation model is implemented as an OpenFOAM C++ library. To satisfy the energy balance problem, the leaf temperature is determined iteratively using Eq. (1.46), with the air temperature as an initial guess for leaf temperature. The energy balance is satisfied once the leaf temperature converges. The numerical model is validated and is used thereafter to investigate the influence of environmental factors and tree properties on the transpirative cooling effect.

1.9 VALIDATION OF VEGETATION MODEL

The vegetation model is first validated against the numerical and experiment study of Kichah et al. (2012). The study provides measurement and numerical (CFD) results of flow through impatiens (jewelweed) plants in a greenhouse. The study investigates the heat and moisture exchanges between vegetation and the air and provides a comprehensive dataset of the response of vegetation to environmental conditions. The simulation domain is adapted according to the study, where the impatiens plants are placed on a table, Fig. 1.3.

The plants and the pots are both modeled as porous medium with different drag coefficients. The drag coefficient of the plant and pot are $c_d = 0.32$ and $c_d = 1$, respectively. The table is modeled as an internal wall (i.e. baffle) that enforces a standard wall boundary condition. The boundary condition of the ground is $T = T_g$ and standard wall functions are used. The top boundary is a symmetry plane. The outlet is taken to be far enough to ensure zero-normal gradient for all variables and a zero pressure is imposed. The inlet boundary conditions are tabulated in Table 1.3, corresponding to a greenhouse in a sunny day on 15th July 2009 at 14:00. Based on a mesh sensitivity analysis, a regular grid discretization is chosen with smallest cells at the edge of the vegetation ($\Delta x = 0.01$, $\Delta y = 0.0055$) and a total number of cells of 24000. The grid expansion ratio from the vegetation edges to the outflow, inlet, ground and top boundaries are 1.05, 1.11, 1.13 and 1.15, respectively.

Fig. 1.4 shows the leaf temperature T_{leaf} distribution of the vegetation and is compared with numerical results from the original study (Kichah et al. 2012). We see that the temperature ranges (between 25 °C and 31 °C) are in good agreement. However, the leaf temperature contours are

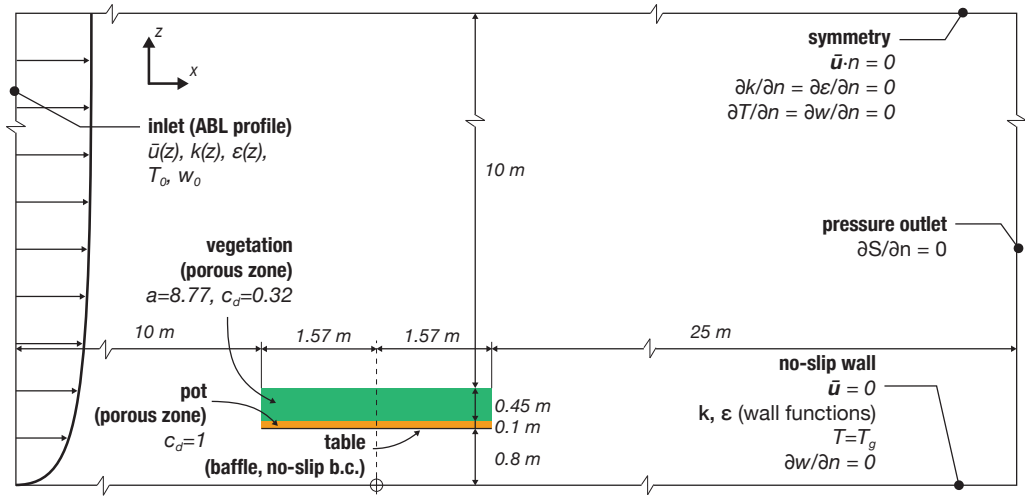


Figure 1.3: Simulation domain and boundary conditions for the validation case Kichah et al. (2012). The impatiens plant in indicated in green (■) and plant plot in orange (□). Both are regions are modeled as porous zone with drag coefficients $c_d = 0.32$ and $c_d = 1$, respectively. The boundary conditions of the simulation are tabulated in Table 1.3 and correspond to 14:00 on June 15th, 2009.

different between the two simulations. The general trend in vertical temperature distribution is in agreement, with peak temperatures appearing close to the top of the vegetation due to radiation absorption. The difference observed between the present model and Kichah et al. (2012) could be due to the use of a turbulence model as the turbulence production and dissipation due to vegetation (Eqs. (11) and (12)) is not done in Kichah et al. (2012). However, it is shown by Sanz (2003) that the influence of vegetation on turbulence has to be modeled to ensure physically accurate turbulence characteristics. Moreover, we employ the realizable $k - \epsilon$ turbulence closure in contrast to the standard $k - \epsilon$ used by Kichah et al. (2012). The realizable $k - \epsilon$ model is chosen as it provides more accurate wake characteristics leeward of a porous medium (Santiago et al. 2007; Shih et al. 1995). The choice of turbulence model is known to have an impact on parameters such as recirculation length (Santiago et al. 2007) and this could result in some difference in the leaf temperature contours.

Furthermore, the validation is performed by comparing the leaf and air temperatures with the numerical and experimental results from Kichah et al. (2012). The numerical and experimental values of leaf temperature T_{leaf} values are obtained for three positions: “bottom” ($x = 0, z = 0.9$), “middle” ($x = 0, z = 1.125$) and “top” ($x = 0, z = 1.35$). The numerical and experimental values of the air temperature T_{leaf} at position “middle” are also compared, as shown in Table 1.4. The comparison shows that the numerical results from the present study are in better agreement with the experiments than the numerical results of Kichah et al. (2012). At the top of the vegetation, the difference between the numerical and experimental results are the highest with $T^{num} - T^{exp} = 1.0^\circ\text{C}$ for both the present study and Kichah et al. (2012). The deviation on the top between the predicted and the measured temperatures could be due to the simplification in the leaf distribution.

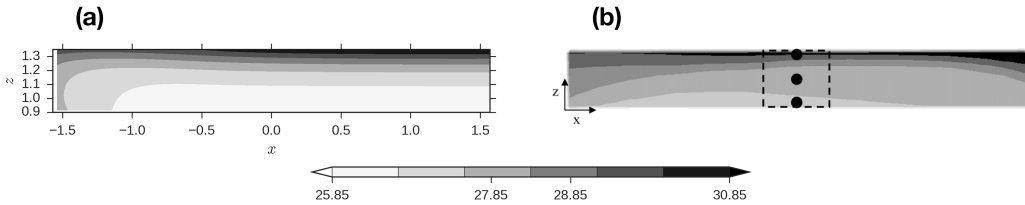


Figure 1.4: Comparison of leaf temperature T_{leaf} ($^{\circ}\text{C}$) within vegetation ($-1.5 \leq x \leq 1.5$) and ($0.9 \leq z \leq 1.35$): (a) present study and (b) numerical simulation results from (Kichah et al. 2012). The three dots (bottom: $z = 0.9$ m, middle: $z = 1.125$ m and top: $z = 1.35$ m) indicate the temperature probe positions, Table 1.4.

The numerical models assume the leaf area density to be homogeneously distributed, however, in reality, it varies in height. This influences the radiation absorption within vegetation and will impact the heat and mass exchanges. Generally, the leaf temperature trend is seen to be slightly overestimated and the air temperature to be slightly underestimated. However, as the deviation is only within 1.0 $^{\circ}\text{C}$, we consider the predicted results to be sufficiently accurate.

1.10 IMPACT OF ROW OF TREES ON THE MICROCLIMATE

The developed numerical model is first used to understand the impact of a single row of trees on the surrounding microclimate. The transpirative cooling effect of vegetation is determined as the change in the Universal Thermal Climate Index (*UTCI*). Thereafter, a parametric study is performed to determine the impact of different environmental factors, tree properties and vegetation. The simulation domain described in Fig. 1.2 is used as the reference case for the parametric study. The environmental boundary conditions are given in Table 1.1 and the tree properties are tabulated in Table 1.2. To ensure fair comparison in the parametric study, the stomatal resistance is fixed to the minimum stomatal resistance $r_s = r_{s,min}$ and is assumed to be independent of the radiation and humidity levels of the environment. The influence of the stomatal model is investigated separately. As mentioned above, the study assumes that the ground is adiabatic to isolate the influence of transpirative cooling effect of the tree row on the air. To study the impact of a

Table 1.3: Environmental conditions used in Kichah et al. (2012). Data obtained for condition at 14:00 on June 15th, 2009.

Parameter	Value
Air temperature, T_0	32 $^{\circ}\text{C}$
Ground temperature T_g	24 $^{\circ}\text{C}$
Humidity ratio w_0	6.21 g kg^{-1}
Solar radiation, $q_{r,sw,0}$	99 W m^{-2}
Long-wave radiation, $q_{r,lw,\downarrow}$	522 W m^{-2}

Table 1.4: Comparison of leaf temperature T_{leaf} at various heights and air temperature T in the middle of vegetation. Experimental and numerical data obtained from (Kichah et al. 2012).

Parameter	Experimental (Kichah et al. 2012)	Numerical (Kichah et al. 2012)	Present	(Kichah et al. 2012)	$T^{num} - T^{exp}$
				$T^{present} - T^{exp}$	
Leaf temperature T_{leaf} ($^{\circ}\text{C}$)					
<i>top</i> ($z = 1.35 \text{ m}$)	29.5	30.5	30.5	1.0	1.0
<i>middle</i> ($z = 1.125 \text{ m}$)	26.7	28.0	27.0	1.3	0.3
<i>bottom</i> ($z = 0.9 \text{ m}$)	26.1	27.6	26.2	1.5	0.1
Air temperature T ($^{\circ}\text{C}$)					
<i>middle</i> ($z = 1.125 \text{ m}$)	28.11	28.5	27.9	-0.4	-0.2

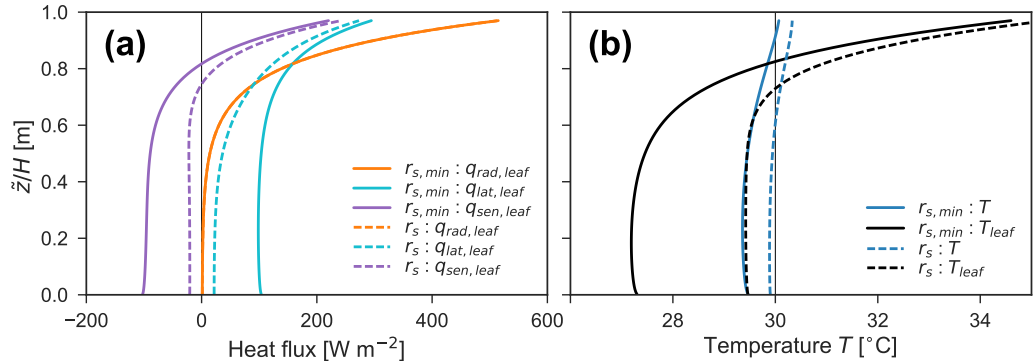


Figure 1.5: Vertical distribution at centre-line of the tree row with height $\tilde{z} = 0$ at bottom of the vegetation volume and $\tilde{z} = 1$ at top of the trees: (a) heat fluxes at the leaf surface (Eq. (1.36)) and (b) temperature profiles of leaf temperature T_{leaf} ($^{\circ}\text{C}$) and air temperature T ($^{\circ}\text{C}$).

single row of trees on the microclimate, the energy balance at the leaf surface and its implication on the flow field are studied first.

1.10.1 Impact on energy balance at the leaf surface

The energy balance at the leaf surface is defined by Eq. (1.36), where the absorbed radiative heat flux is converted into latent and sensible heat fluxes. The average radiative flux into the leaf is $\langle q_{rad,leaf} \rangle = 77 \text{ W m}^{-2}$ for both cases. In the case of constant stomatal resistance, $r_s = r_{s,\min}$, the average sensible flux is $\langle q_{sen,leaf} \rangle = -50 \text{ W m}^{-2}$ (negative sign indicates cooling of the air) and the average latent heat flux is $\langle q_{lat,leaf} \rangle = 127 \text{ W m}^{-2}$ used to evaporate water. In the case of varying stomatal resistance Eq. (1.43), the average sensible and latent heat fluxes are 9 W m^{-2} and 68 W m^{-2} , respectively. To better understand how the radiative heat is converted, the heat flux distribution and the leaf temperature distribution within the foliage are studied. Fig. 1.5 shows the vertical distribution of heat fluxes and temperature along the vertical centre line within the centre of the foliage. Fig. 1.5a shows that the heat fluxes are maximum at the top of the trees, where solar radiation is mostly absorbed due to the high density of vegetation with $a = 10 \text{ m}^2 \text{ m}^{-3}$. A high absorbed radiative heat results in a positive sensible heat flux (indicating heat is leaving the leaf and entering air) leading to an increase of the air temperature, as seen in Fig. 1.5b. The latent heat flux is also positive due to transpiration at the leaf, Eq. (1.39). At lower heights, the radiation decays exponentially given the prior absorption of the short-wave radiation, Eq. (1.51), resulting also in an exponential decay of the latent and sensible heat fluxes. At the bottom of the foliage, the sensible heat flux is negative as the radiation is low but transpiration still occurs, leading to cooling of the air.

In the case of environmentally dependent stomatal resistance, the stomatal resistance is higher than minimum stomatal resistance, when the stomata are fully open. As stomatal resistance is inversely proportional to incident short-wave radiation (Eq. (1.43)), this resistance is low at the top of the trees and high at the bottom of the trees. A higher stomatal resistance means that

the CMTC is lower (Eq. (1.40)) and so the water vapor mass flux due to transpiration reduces. The reduced transpiration leads to higher leaf temperature and therefore lower cooling of the air provided by vegetation (Fig. 1.5). With a minimum stomatal resistance, the average air temperature is 29.6 °C. Whereas, with higher stomatal resistances, the transpiration is reduced and the higher leaf temperature results in an average air temperature of 30.0 °C. To further understand the impact of stomatal resistance, the change in flow conditions due to vegetation is studied.

1.10.2 *Influence of vegetation on the flow field*

The heat, mass and momentum exchanges between the trees and the air determine the distribution of velocity, temperature and humidity. Furthermore, the turbulence intensity is increased due to the foliage. Fig. 1.6a shows the normalized velocity magnitude \bar{u}/U_{ref} , which shows the influence of momentum drag of the trees. The dashed box in the figure indicates the porous region where the source terms for vegetation are present. The figure shows that the wind speed is reduced by 50% behind the tree row. Furthermore, we see that the flow is slightly accelerated below the tree row between the tree bottom and the ground due to the blockage effect present in below a row of trees. Fig. 1.6b shows the increase in the turbulence intensity $TI = (2/3k)/\bar{u}$ due to the trees as it converts the mean kinetic energy into the turbulence kinetic energy. The TI inside the porous region is approximately 20% higher than the freestream flow. However, we see that the highest TI is observed in the wake region, $TI \approx 50\%$, where the mean velocity is lowest and the TKE is high. Therefore, the impact of vegetation on the turbulence characteristics in a microclimate is not negligible.

Fig. 1.6c shows the influence of a single row of trees on the air temperature. We observe that the highest cooling is at the bottom of the trees, where the absorbed radiation is lowest. The temperature is also lower towards the wake of the trees where the velocity is lower. Such “oasis” effect of cool temperature region in the vicinity of vegetation has also been observed in various field measurements (Kurn et al. 1994; Taha 1997; Wong et al. 2003) and numerical studies (Dimoudi and Nikolopoulou 2003; Gromke 2011). At the top of the tree foliage, we observe a higher air temperature due to higher absorption solar radiation but the temperature is only marginally higher than the ambient temperature. The air temperature increases because the leaf temperature is higher than the windward air temperature (Fig. 1.5b). Fig. 1.6d shows that the humidity ratio increases and the highest humidity is at the top-downstream region of the trees. The figure shows that maximum transpiration occurs at the top of the trees, since solar radiation absorption is highest at the top of the trees and transpiration is also the process used by the trees to dissipate the absorbed radiative heat. The increase of humidity ratio towards the downstream region of the trees is due to the wind convecting the humidity towards the leeward side of the trees.

1.10.3 *Transpirative cooling effect of a row of trees*

A quantitative analysis of the transpirative cooling effect of a single row of trees and its impact on thermal comfort is possible by investigating the Universal Thermal Comfort Index (UTCI). The comfort index is expressed as an equivalent temperature and is determined from a human

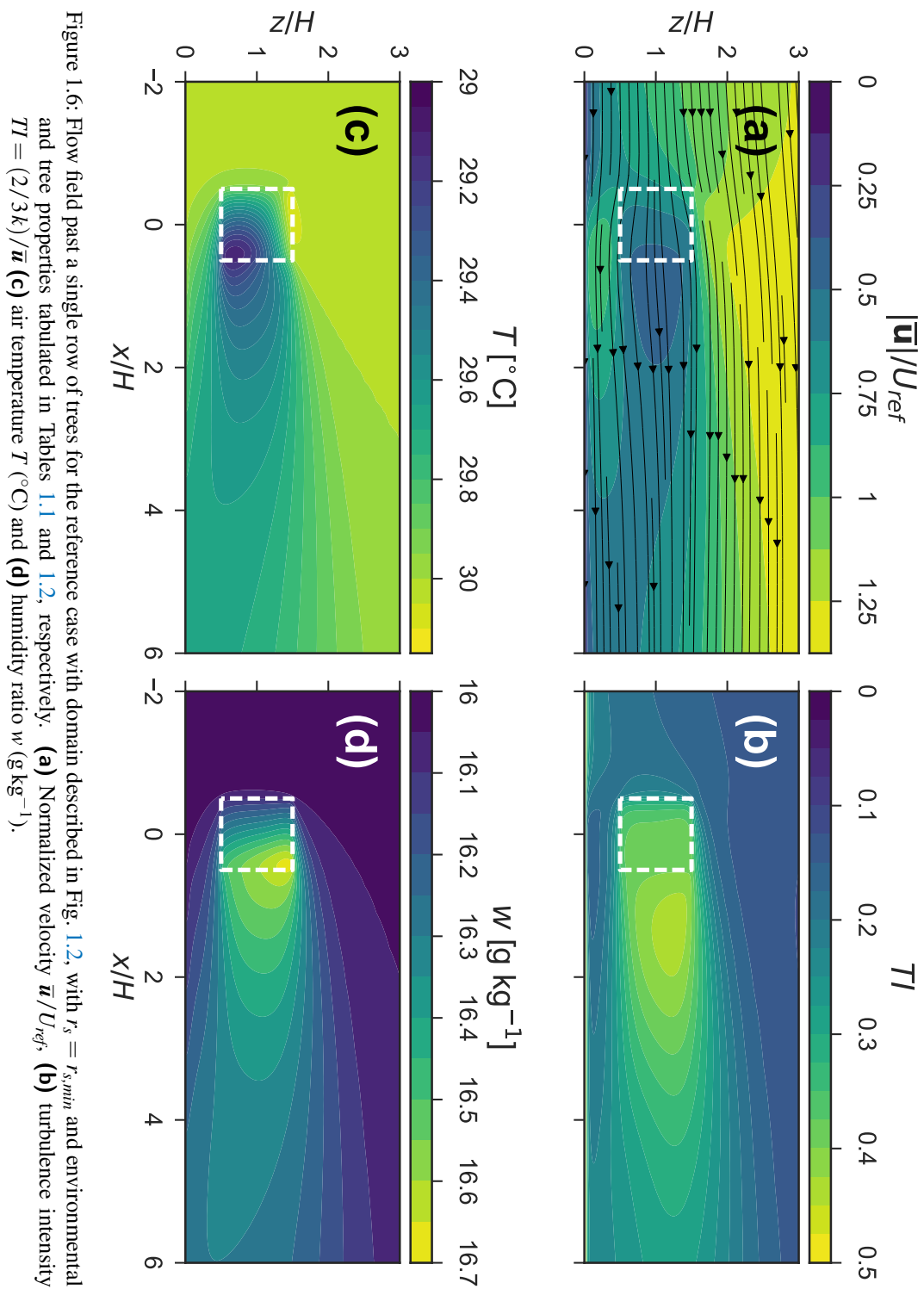


Figure 1.6: Flow field past a single row of trees for the reference case with domain described in Fig. 1.2, with $r_s = r_{s,min}$ and environmental and tree properties tabulated in Tables 1.1 and 1.2, respectively. (a) Normalized velocity $\bar{\mathbf{u}}/U_{ref}$, (b) turbulence intensity $TI = (2/3k)/\bar{u}$ (c) air temperature T ($^{\circ}\text{C}$) and (d) humidity ratio w (g kg^{-1}).

thermoregulatory response model coupled with a clothing model (Fiala et al. 2001). The equivalent temperature is dependent on the air temperature, humidity, wind speed and radiation and represents the temperature of a reference environment that would provide the same response for the reference person as it would in the actual environment. It is designed as an outdoor comfort index and is seen to outperform similar other comfort indices such as Perceived Temperature (PT), Physiological Equivalent Temperature (PET) and OUT_SET* (Jendritzky et al. 2012). Furthermore, it can be used as an international standard for all assessments of the outdoor thermal conditions in various fields such as public weather services, public health systems and climate impact research. Therefore, the UTCI is used in this study to provide an indication of the comfort for a pedestrian in vicinity of trees. The UTCI is implemented in the BioKlima 2.6 software package and is calculated as ($^{\circ}\text{C}$):

$$\text{UTCI} = T + f(T, T_{mrt}, |\mathbf{u}|, RH) \quad (1.56)$$

where it is a function of air temperature T , the mean radiant temperature T_{mrt} , wind speed $|\mathbf{u}|$ and relative humidity RH . The mean radiant temperature T_{mrt} is influenced by the long-wave and the short-wave radiation, which is a function of direct solar radiation $q_{r,sw}$ and the solar altitude ϕ . However, in this study we ignore the long-wave radiation component in the UTCI as the main goal of the study is to isolate the influence of transpirative cooling effect on the air and determine the influence of wind speed, temperature, RH, solar radiation and tree properties on the transpiration rate. By modeling the ground as an adiabatic surface, the soil heat storage could be decoupled from the interaction of transpirative cooling. We remark that, in the present study, diffuse solar radiation and long-wave radiation are not considered in the determination of mean radiant temperature for UTCI. These radiation components will be determined in future analysis for a more accurate assessment of pedestrian comfort, especially in the vicinity of buildings. The UTCI provides an indication of the thermal stress experienced by a pedestrian, as tabulated in Table 1.5. The UTCI values that lie between $18\ ^{\circ}\text{C}$ and $26\ ^{\circ}\text{C}$ comply as “*thermal comfort zone*” (Marshall 1987). A UTCI value in the range of a moderate heat stress (HS) level can result in sweating for the reference person after 30 minutes, where fatigue is possible after prolonged exposure or physical activity (Blazejczyk et al. 2012; Błazejczyk et al. 2013). A UTCI value in the range of a strong HS level results in an instantaneous change in skin temperature and introduces the risk for sunstroke and muscle cramp after prolonged exposure. A very strong HS level is considered dangerous showing increase in internal body temperature within 30 minutes with high possibility of sunstroke and muscle cramp after prolonged exposure. An extreme HS level is considered highly dangerous with high likeliness of heat stroke.

Fig. 1.7 shows the transpirative cooling effect of a tree row for fixed and varying stomatal resistance conditions. The figure compares transpiring (when stomata are open and transpiration from trees is enabled) and non-transpiring conditions (when stomata are closed and transpiration from trees is disabled). Fig. 1.7a shows the UTCI ($^{\circ}\text{C}$) distribution during non-transpiring condition. As transpiration does not occur, the UTCI is the same for fixed and varying stomatal resistance. The figure shows that at the upstream region, where the flow is unaffected by the tree ($x/H = -2\text{ m}$), the UTCI reduces with height. The decrease of the UTCI with height is caused by the increase of wind speed with height. The figure also shows that the lowest value of the UTCI occurs inside and below the trees as it provides shading from the sun. The UTCI drops

Table 1.5: UTCI thermal heat stress categories (Bröde et al. 2012; Oke et al. 2017).

UTCI (°C)	Thermal stress categories	Physiological responses
> 46	Extreme heat stress (HS)	Increase in core temperature
38 to 46	Very strong HS	Small core to skin temperature gradient (< 1 K), Sweat rate increase ($> 650 \text{ g h}^{-1}$ at limit)
32 to 38	Strong HS	Sweat rate $> 200 \text{ g h}^{-1}$
26 to 32	Moderate HS	Increased rate of sweating and skin temperature
9 to 26	No thermal stress	Comfortable, sweat rate $< 100 \text{ g h}^{-1}$

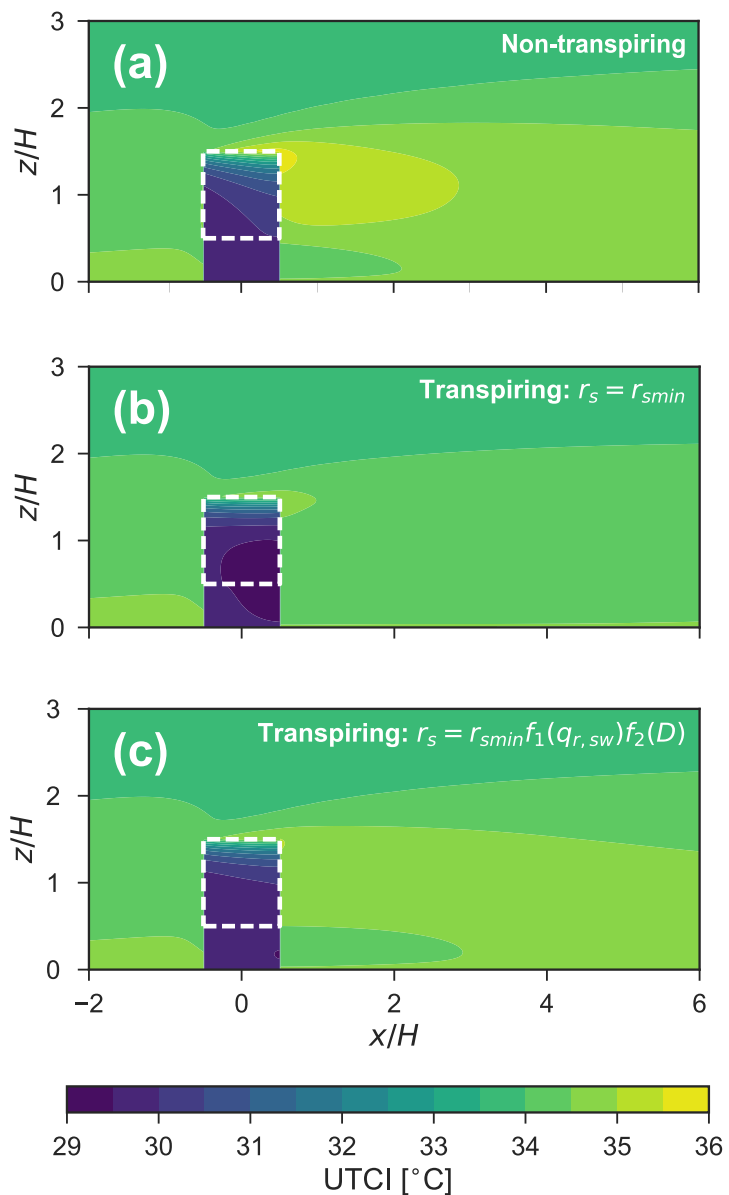


Figure 1.7: Transpirative cooling effect of a single row of trees. The influence of the trees on the Universal Thermal Comfort Index (UTCI) ($^{\circ}\text{C}$) for (a) in non-transpiring condition (NT); in transpiring condition (T) for (b) constant stomatal resistance, $r_{s,min}$ and (c) for varying stomatal resistance $r_s = r_{s,min}f(q_{r,sw})f(D)$.

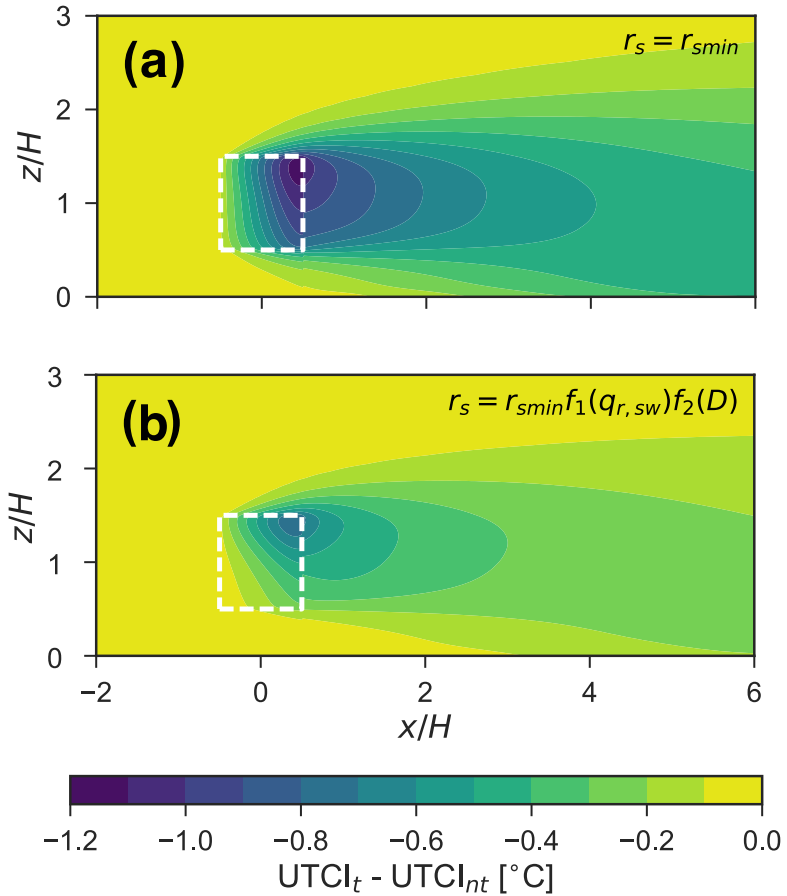


Figure 1.8: UTCI difference between transpiring and non-transpiring conditions, $UTCI_t - UTCI_{nt}$ (°C), for **(a)** constant stomatal resistance and **(b)** varying stomatal resistance.

from 36 °C, a regime of strong heat stress, to 29 °C where the heat stress is moderate. Therefore, the trees have a large influence on the UTCI due to the shadowing effect from the solar radiation. This observation is in good agreement with field measurements of a rooftop garden in Singapore by Wong et al. (2003) where a large reduction in air temperature due to shading is also observed directly below the foliage. In the non-transpiring condition, we see that downstream of the trees, the UTCI increases, especially near the top region of the trees where most solar radiation is absorbed and the air temperature leaving the trees is higher. The absorbed radiation is balanced only with the sensible heat flux. The trees dissipate the energy simply through thermal exchanges leading to an increase in UTCI. Therefore, in an environmental condition such as drought, trees are unable to provide cooling through transpiration. Water availability is a key aspect for trees to form an effective cooling measure in urban areas. This can be challenging for cities as regular irrigation in summer, especially during heat waves, can further exacerbate the water demand and additionally, increase the cost of maintenance.

Fig. 1.7b and Fig. 1.7c show the UTCI during the transpiring condition for fixed and varying stomatal resistances, respectively. We see that, for both cases, transpiration from the trees is beneficial as it reduces the UTCI compared to the non-transpiring condition. Fig. 1.8 shows the difference in UTCI between transpiring and non-transpiring conditions by calculating $UTCI_t - UTCI_{nt}$ (°C). Comparing the fixed and varying stomatal resistance cases, Fig. 1.8a and Fig. 1.8b respectively, we see that the varying stomatal case provides slightly less reduction in UTCI. Referring to the energy balance, and its results on Fig. 1.5, the stomatal resistance is seen to increase towards the bottom of the foliage thereby reducing transpiration and increasing the leaf temperature. The region with the most transpirative cooling is the near-downstream region of the trees. This correlates with the observation of temperature and humidity distribution observed in Fig. 1.6. At higher stomatal resistance, the transpirative cooling is reduced due to the reduced latent heat flux. In the end, we see that the factor most contributing to improve pedestrian comfort is the shadowing provided by the trees, providing much lower UTCI than the transpirative cooling effect.

1.11 INFLUENCE OF ENVIRONMENTAL FACTORS

A parametric study is performed on the influence of environmental conditions on the transpirative cooling effect of a single row of trees. The influence of environmental factors, i.e. wind speed U_{ref} , air temperature T , relative humidity RH and solar radiation $q_{r,sw}$ is studied by varying them independently Table 1.1. The impact of these environmental factors are determined by studying the energy exchanges at the leaf surface, the air temperature and the UTCI. The air temperature T and the UTCI are evaluated at three distinct locations: *upstream*, *downstream* and in the *shaded* region, as depicted in Fig. 1.2. The upstream region is unaffected by the trees, the downstream region is only affected by the transpiration and, finally, the shaded region shows the influence of shading from sun.

1.11.1 Influence of wind speed

The wind speed has a direct influence on the convective transfer coefficients at the leaf surface. Due to this, wind speed also has an impact on the cooling effect of the trees. Therefore, the heat

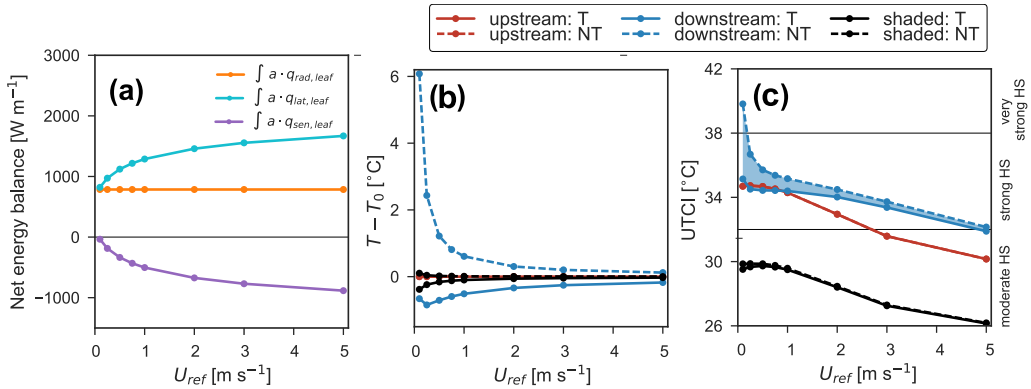


Figure 1.9: Influence of wind speed (m s^{-1}) on (a) on the net energy balance of radiation, sensible and latent heat fluxes at the trees, $\int a \cdot (q_{rad,leaf} - q_{sen,leaf} - q_{lat,leaf}) dA = 0$ (W m^{-2}), (b) on air temperature $T - T_0$ ($^{\circ}\text{C}$), and (c) on UTCI ($^{\circ}\text{C}$). Point measurement of air temperature and UTCI at three locations as shown in Fig. 1.2: upstream (red), downstream (blue) and shaded (black) for transpiring (T) (solid, —) and non-transpiring (NT) conditions (dashed, - - -).

exchanges and the resulting cooling of the environment is studied for various wind speeds. The influence of wind speed on the net energy at the leaf is shown in Fig. 1.9a. A negative sensible heat flux indicates that heat is being extracted from the air and, therefore, cooling of the air occurs. The figure shows that the magnitude of the heat fluxes is increasing with wind speed. At high wind speed, the aerodynamic resistance (Eq. (15)) reduces and leads to an increase in CHTC (Eq. (1.37)) and CMTC (Eq. (1.39)). We also observe that, at high wind speeds, the heat fluxes become less sensitive to wind speed. Therefore, it indicates that cooling by the trees becomes less sensitive to wind speed at higher wind speeds due to the power-law relation of CHTC and wind speed.

Fig. 1.9b shows the air temperature difference between the inlet and three distinct locations ($T - T_0$): *upstream*, *downstream* and *shaded*, as depicted in Fig. 1.2. In addition, the air temperature is compared for the transpiring (T) and non-transpiring (NT) conditions, to indicate the influence of transpirative cooling. The upstream region is unaffected by the trees and remains constant for transpiring and non-transpiring conditions. In the shaded region, the transpirative cooling has only a small influence as there is no cold air transported downwards from the trees. For the non-transpiring condition, the air temperature increases slightly at lower wind speeds. For the transpiring condition, the air temperature reduces by 0.4 °C. In the downstream region, the influence of the trees on the air temperature is clearly visible, with a large increase in air temperature for the non-transpiring condition, up to 6 °C, and significant drop in air temperature for the transpiring condition, approximately -0.9 °C at the wind speed of 0.25 m s⁻¹. Fig. 1.9b also shows that air cooling downstream of the trees decreases with increasing wind speed. Dimoudi and Nikolopoulou (2003) also provide similar finding in their CFD study of vegetation in urban environment, where the effect of vegetation seems to decrease with increasing wind speed. This occurs as, for higher wind speeds, the trees extract a similar amount of heat per second from a

larger air volume, resulting in a smaller overall temperature reduction. At low wind speeds, the heat extraction is done over a small volume of air, i.e., a lower flow rate, providing a larger temperature reduction. Similarly, during non-transpiring conditions, the air temperature substantially increases near the trees, since in this case the radiative heat is not converted into latent heat, but convected as sensible heat into the air domain. Therefore, when the goal is to provide maximum reduction in air temperature in the vicinity of the tree row, lower wind speeds are preferable. As such, at low wind speeds, a local cool region is created around the vegetation. However, at higher wind speeds, the total amount of sensible heat that is extracted from the flow by transpiration is larger. Thus, for global heat island mitigation, high wind speeds are more beneficial, while low wind speeds are favorable to improve the local thermal comfort around a tree.

Fig. 1.9c shows the UTCI in transpiring and non-transpiring conditions. For both conditions, the UTCI reduces with increasing wind speed at all locations, as expected. The upstream probe point shows that high wind speeds result in a reduced UTCI as wind speed has a direct influence on the comfort. The heat stress levels reduce from strong heat stress (HS) to moderate HS. This characteristic is also visible for the downstream and the shaded probe point. However, the shaded probe point is always in moderate HS levels for all wind speeds. This is due to the reduced radiation levels, indicating the importance of shading provided by the trees yielding a 4 – 6 °C reduction in the UTCI. The impact of transpirative cooling is visible by studying the difference between transpiring and non-transpiring conditions, $UTCI_t - UTCI_{nt}$ (indicated in shaded area). The figure shows that the transpirative cooling provided by the trees, i.e. $UTCI_t - UTCI_{nt}$, only has an impact downstream of the tree row as it is negligible at both upstream and shaded regions. At low wind speeds, the transpirative cooling is the largest whereas, at higher wind speeds, the impact of transpirative cooling on the UTCI is negligible. This indicates that a pedestrian downstream of a tree row only notices the benefit of transpirative cooling when wind speeds are low. However, vegetation extracts more heat from the environment when wind speeds are higher.

1.11.2 Influence of relative humidity and air temperature

The vapor pressure varies depending on relative humidity (RH) and air temperature T . A variation in vapor pressure of the air has a direct influence on the rate of transpiration, since mass flux from leaf surface is driven by the gradient in vapor pressure between the leaf surface and the ambient air. As a result, RH and ambient air temperature have a direct influence on the cooling power of the tree row. Fig. 1.10a shows the influence of RH and air temperature on the heat exchanges. We observe that, at low RH, the magnitudes of the latent and sensible heat fluxes are high. This indicates high transpiration rate and similarly large cooling, as indicated by the downstream probe point in transpiring conditions, as seen in Fig. 1.10b. However, at high RH, the transpiration is much lower and results in a higher leaf temperature leading to heating of the air. This is due to air vapor pressure approaching saturation resulting in a reduced capacity for air to take up additional humidity from the leaves. At lower air temperature, $T = 20$ °C, the saturation vapor pressure of the air is lower and, therefore, the air has less capacity to take in the humidity from the leaves. With a reduced transpiration rate, the latent heat flux is reduced, leading to higher air temperature (Fig. 1.10b). Thus, we see that the trees provide the maximum

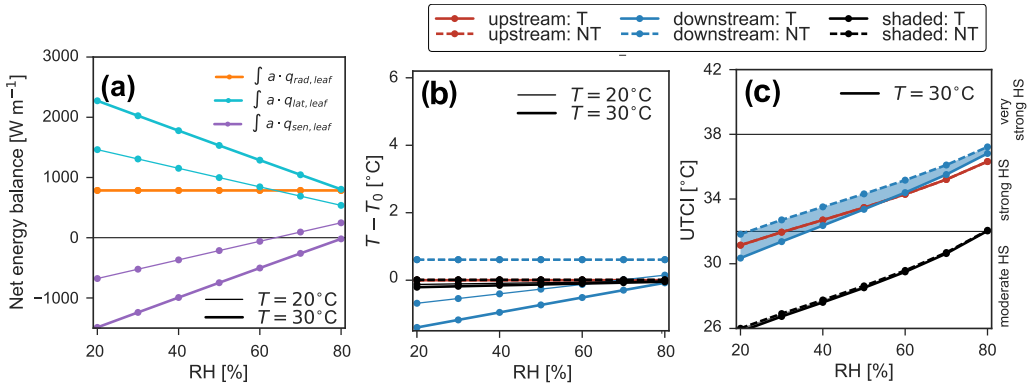


Figure 1.10: Influence of relative humidity RH (%) at air temperature $T = 20^\circ\text{C}$ (thin) and $T = 30^\circ\text{C}$ (thick) on (a) on the net energy balance of radiation, sensible and latent heat fluxes at the trees, $\int a \cdot (q_{rad,leaf} - q_{sen,leaf} - q_{lat,leaf}) dA = 0$ (W m^{-2}), (b) on air temperature $T - T_0$ ($^\circ\text{C}$), and (c) on $UTCI$ ($^\circ\text{C}$). Point measurement of air temperature and $UTCI$ at three locations as shown in Fig. 1.2: upstream (red), downstream (blue) and shaded (black) for transpiring (T) (solid, —) and non-transpiring (NT) conditions (dashed, - - -).

cooling during hot dry conditions providing approximately 4.5 times larger air temperature drop (at $T = 30^\circ\text{C}$ and $RH = 20\%$) than the colder humid condition (at $T = 20^\circ\text{C}$ and $RH = 80\%$).

Fig. 1.10c shows the influence of RH on thermal comfort at $T = 30^\circ\text{C}$. With increasing RH from dry to humid conditions, the $UTCI$ increases from a moderate to a strong heat stress regime. This effect is independent of the trees as RH and temperature play themselves also a direct role on the thermal comfort as high humidity results in lower comfort for a pedestrian. Studying the influence of transpirative cooling, we see that the shaded and upstream locations are unaffected, showing a negligible $UTCI_t - UTCl_{nt}$. However, we note that transpirative cooling consistently improves thermal comfort in the downstream region, with a greater influence in the dry condition. At higher RH, even though transpiration reduces the $UTCI$, the $UTCI$ downstream of the tree row is higher than the upstream region. However, this does not indicate that the presence of trees is detrimental, as the thermal influence of the ground is not modeled in the present study. The trees provide shading to the ground and we recall that the resulting additional cooling due to lower ground temperature is not taken into account in the present study.

1.11.3 Influence of solar radiation intensity

The net absorbed solar radiation, $\int a q_{rad,leaf} dV$, has a direct influence on the transpiration rate from the leaves. Fig. 1.11a shows the influence of solar radiation on the energy balance. The magnitude of the latent heat flux increases with increasing solar radiation. However, we notice that, even though there is a higher transpiration rate from the trees (as CMTC is constant), the sensible heat flux becomes more positive resulting in less cooling, as depicted in Fig. 1.11b. This indicates that, at high solar radiation, the transpiration rate is not sufficiently high to ensure

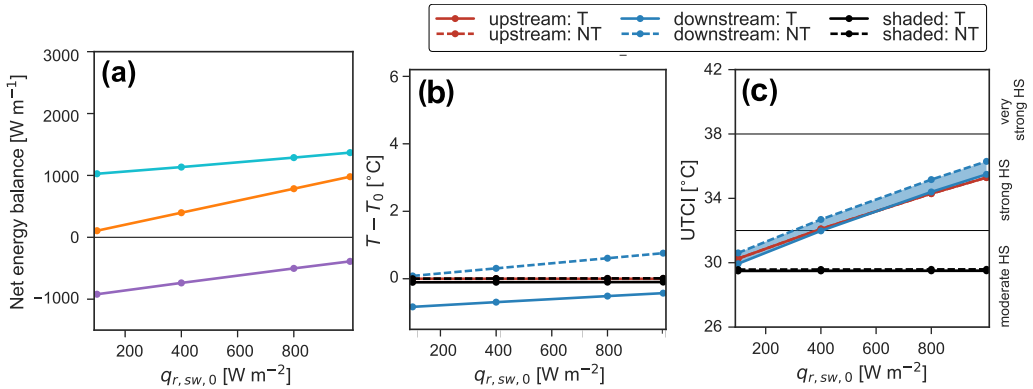


Figure 1.11: Influence of solar radiation $q_{r,sw,0}$ (W m^{-2}) on (a) on the net energy balance of radiation, sensible and latent heat fluxes at the trees, $\int a \cdot (q_{rad,leaf} - q_{sen,leaf} - q_{lat,leaf}) dA = 0$ (W m^{-1}), (b) on air temperature $T - T_0$ ($^{\circ}\text{C}$), and (c) on $UTCIf - UTCI_{nt}$ ($^{\circ}\text{C}$). The shaded region shows the difference $UTCIf - UTCI_{nt}$ ($^{\circ}\text{C}$). Point measurement of air temperature and $UTCIf$ at three locations as shown in Fig. 1.2: upstream (red), downstream (blue) and shaded (black) for transpiring (T) (solid, —) and non-transpiring (NT) conditions (dashed, - - -).

cooler leaves as seen in the low radiation intensity case. Studying the temperature variations in the upstream and the shaded regions, no influence of radiation on transpirative cooling is seen.

Fig. 1.11c shows the influence of solar radiation on thermal comfort. The UTCI in both the downstream region and the upstream regions is almost similar. At both locations, the UTCI increases from moderate HS to strong HS simply due to the higher value of solar radiation. The transpirative cooling effect, indicated by $UTCIf - UTCI_{nt}$, is nearly constant at all solar radiation levels. Therefore, we see that the transpirative cooling provided by the trees is weakly dependent on the solar radiation. In the shaded region indicated by the black line, the UTCI is much lower and is independent of the solar radiation due to the shadowing effect.

1.11.4 Summary on the impact of environmental factors

For this case study, the transpirative cooling effect of a single row of trees is highest at lower wind speed when $U < 1 \text{ m s}^{-1}$. At higher wind speed, the impact of wind speed on latent and sensible heat fluxes becomes weak and a non-linear dependency is only observed for wind speed (Fig. 1.9a). This also results in very small changing air temperature at higher wind speeds (Fig. 1.9b). Relative humidity and solar radiation result in a rather linear change in air temperature. We observe that a pedestrian locally notices the benefit of transpirative cooling when wind speeds are low as indicated by UTCI. However, the trees extract the maximum heat from the environment at high wind speeds. Thus, policies focused on mitigation of the citywide heat island effect should ensure that only trees with low blockage effect are planted and in well-ventilated areas. Whereas, policies aimed at creating oasis of cool areas should focus on making dense vegetation areas such as parks that can substantially reduce the wind speed. Furthermore, we

also observe that the trees provide the largest cooling effects during hot conditions with low RH. However, to ensure this transpirative cooling, the plants need to be well irrigated, which can be difficult in hot and dry cities. Therefore, in such climatic conditions, cities can focus on developing parks and similar dense localized vegetated areas that not only create oases of cool and humid areas but also the irrigation of such areas can be more efficient. Whereas, in humid conditions, the transpirative cooling effect is negligible and the comfort is only improved by the shadowing effect. Therefore, cities with hot and humid conditions should focus on integrating tall-wide canopy trees that can maximize the shadowing effect.

1.12 INFLUENCE OF TREE PROPERTIES

The influence of tree properties on the transpirative cooling effect of a tree row is investigated by varying the leaf size l , minimum stomatal resistance $r_{s,min}$ and the leaf area density a .

1.12.1 *Influence of leaf size*

Fig. 1.12a shows the impact of leaf size on the energy balance. The figure shows that the sensible and latent fluxes reduces in strength with increasing leaf size. The behavior is due to inverse relation of CHTC (Eq. (1.37)) and CMTC (Eq. (1.39)) with leaf size. A large leaf size results in reduced heat and mass fluxes from the trees, yielding the reduced cooling seen in Fig. 1.12b. The highest cooling effect is observed when leaf size is small since CHTC and CMTC are then higher, when convective transfer is more efficient. This is also evident from field measurements of forest trees where smaller-leaves species is observed to be cooler(Leuzinger and Körner 2007; Leuzinger, Vogt, et al. 2010). The influence of transpirative cooling is negligible in the upstream and shaded region and the thermal comfort, indicated by UTCI is nearly unaffected by the leaf size, Fig. 1.12c. Even though there is a variation in the air temperature (Fig. 1.12b), the UTCI is relatively unaffected as there is also an increase in humidity downstream of the trees, counteracting the benefit provided by the reduced air temperature. The use of leaf size in determining CHTC and CMTC shows that a higher developing length, resulting in a larger aerodynamic resistance over the leaf surface, reduces convective exchanges.

1.12.2 *Influence of stomatal resistance*

The stomatal resistance has a larger influence on the heat and mass fluxes than the leaf sizes as shown in Fig. 1.13a. As CMTC is inversely dependent on the stomatal resistance, increasing the stomatal resistance causes the transpiration from the leaf to decrease. Less transpiration leads to less heat removal causing an increase of leaf temperature and a reduced cooling effect, as shown in Fig. 1.13b. Therefore, plants with low stomatal resistance such as the impatiens plant or grass can provide more cooling than deciduous plant, for similar leaf sizes and leaf area densities. Fig. 1.13c shows that stomatal resistance has a weak influence on the UTCI. As seen with leaf size, a stomatal resistance variation results in a negligible change in UTCI downstream of the trees as the lower air temperature is counter-balanced with higher air humidity. However

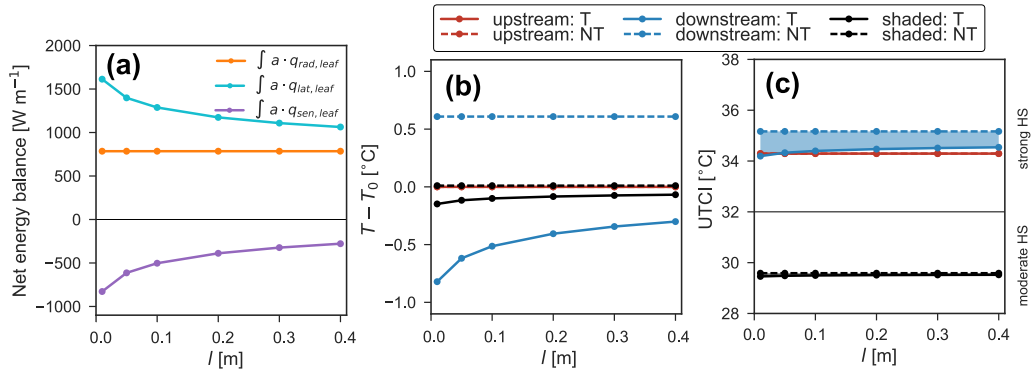


Figure 1.12: Influence of leaf size l (m) **(a)** on the net energy balance of radiation, sensible and latent heat fluxes at the trees, $\int a \cdot (q_{rad,leaf} - q_{sen,leaf} - q_{lat,leaf}) dA = 0 \text{ W m}^{-1}$, **(b)** on air temperature $T - T_0$ ($^{\circ}\text{C}$), and **(c)** $UTCI$ ($^{\circ}\text{C}$). Point measurement of air temperature and $UTCI$ at three locations as shown in Fig. 1.2: upstream (red), downstream (blue) and shaded (black) for transpiring (T) (solid, —) and non-transpiring (NT) conditions (dashed, - - -).

comparing the transpiring and non-transpiring cases, we see that transpiration still provides an improvement in thermal comfort showing a positive difference $UTCI_t - UTCI_{nt}$, Fig. 1.13c.

1.12.3 Influence of leaf area density

Fig. 1.14a shows that, when leaf area density is low, the net radiation absorbed by vegetation is lower due to the lack of leaf surfaces to absorb the radiation, which means more solar radiation can pass through the vegetation. Fig. 1.14b shows that there is a decrease in the $UTCI$ in the shaded region with higher leaf density, which increases shading of solar radiation. In the case of low leaf area density, more leaf surfaces are exposed to a higher solar radiation over the whole volume of vegetation, resulting in higher air temperature while the transpiration rate is not sufficient to cool the leaves, Fig. 1.14c. Hiraoka (2005) also observes that, for a single tree with leaf area density $a = 1$, at environmental condition of $T = 30 \text{ } ^{\circ}\text{C}$ and $RH = 80 \%$, sensible heat is added to the air domain. However, with a higher leaf area density, more solar radiation is absorbed at the top of the vegetation, shading the lower regions from the solar radiation. This is beneficial as leaf surfaces at lower regions are then able to dissipate the absorbed solar radiation through transpiration and to cool the air. Therefore, the leaf area density should be sufficiently high such that solar radiation is mostly absorbed at the top of the vegetation volume.

1.12.4 Summary on the influence of tree properties

The study on the influence of tree properties on the net energy balance shows that both leaf size and stomatal resistance have a non-linear effect. Both leaf size and stomatal resistance influence the convective heat and mass transfer coefficients at the surface of leaves. Plants with larger

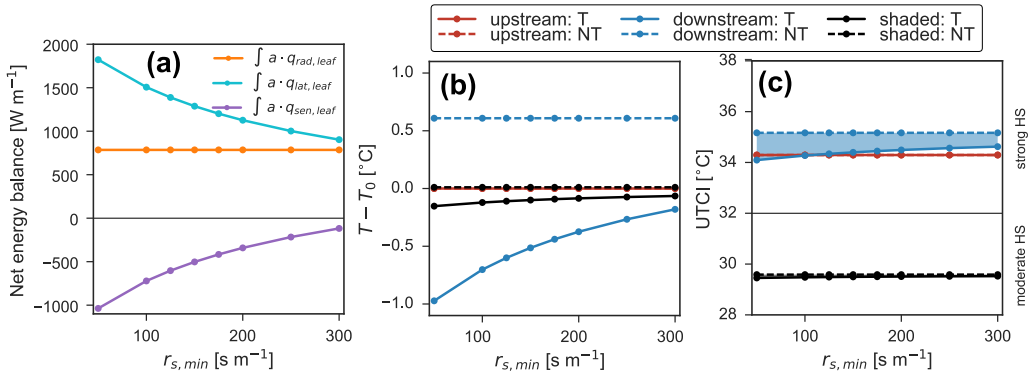


Figure 1.13: Influence of stomatal resistance $r_{s,\min}$ (s m^{-1}) on (a) the net energy balance of radiation, sensible and latent heat fluxes at the trees, $\int a \cdot (q_{rad,leaf} - q_{sen,leaf} - q_{lat,leaf}) dA = 0 \text{ W m}^{-2}$, (b) on air temperature $T - T_0$ ($^{\circ}\text{C}$), and (c) UTCI ($^{\circ}\text{C}$). Point measurement of air temperature and UTCI at three locations as shown in Fig. 1.2: upstream (red), downstream (blue) and shaded (black) for transpiring (T) (solid, —) and non-transpiring (NT) conditions (dashed, - - -).

leaves provide less cooling effect than plant with small leaves, Fig. 1.13a. We also observe that, to provide the highest cooling, the stomatal resistance should be low such that transpiration rate is high. However, higher rate of transpiration results also in increased humidity in the air and counters the thermal comfort provided by reduced air temperature. The study on the impact of leaf area density shows that leaf area density should be sufficiently high such that solar radiation is mostly absorbed at the top of the vegetation volume. Therefore, the lower part of the volume are shaded and can provide cooling to the air. A similar observation is found in the field measurements of rooftop gardens in Singapore where thicker foliated plants are shown to provide more cooling (Wong et al. 2003). The cooling provided by the single row of trees is seen to grow almost linearly with leaf area density providing 10 times higher temperature drop and UTCI drop for a densely foliated tree row of $a = 10 \text{ m}^2 \text{ m}^{-3}$ compared to a weakly foliated tree row of $a = 1 \text{ m}^2 \text{ m}^{-3}$. Therefore, cities focused on mitigating UHI through shading of vegetation should ensure that the trees are sufficiently foliated to reduce the transmission of short-wave radiation through vegetation.

1.13 INFLUENCE OF VEGETATION SIZE

Finally we investigate how vegetation size influences the transpirative cooling effect. The size of vegetation in the domain can be described in terms of its length, i.e. number of tree rows n , or the height of the trees nH as shown in Fig. 1.15. The impact of the tree height on the air temperature is determined by probing the *upstream* region ($x = -H$, $y = H$), the *shaded* region ($x = 0$, $y = H/4$) and the *downstream* region ($x = H$, $y = H$) at fixed heights. The probe locations have fixed heights as they represent a reference pedestrian standing next to trees with varying heights. The impact of number of tree rows on the air temperature is determined for three positions: *upstream* ($x = -H$, $y = H$), *shaded* ($x = 0$, $y = H/4$) and *downstream* region

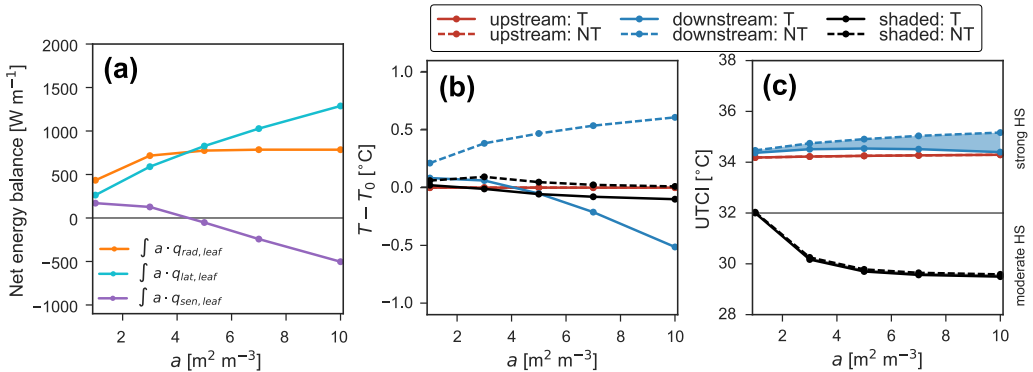


Figure 1.14: Influence of leaf area density a ($\text{m}^2 \text{ m}^{-3}$) on (a) the net energy balance of radiation, sensible and latent heat fluxes at the trees, $\int a \cdot (q_{rad,leaf} - q_{sen,leaf} - q_{lat,leaf}) dA = 0$ W m^{-2} , (b) on air temperature $T - T_0$ ($^\circ\text{C}$), and (c) UTCI ($^\circ\text{C}$). Point measurement of air temperature and UTCI at three locations as shown in Fig. 1.2: upstream (red), downstream (blue) and shaded (black) for transpiring (T) (solid, —) and non-transpiring (NT) conditions (dashed, - - -).

($x = nH + H$, $y = H$). The downstream probe point is located at distance H away from the last downwind tree row.

1.13.1 Influence of number of tree rows

A study on the influence of the number of tree rows provides an understanding on how increasing vegetation along the downstream direction has an effect on the overall cooling of the environment. Fig. 1.16a shows the influence of number of tree rows on the net energy balance. The net absorbed radiation is linearly increasing with number of tree rows. The latent heat flux increases as well whereas the sensible heat flux approaches zero. Despite an increase in net transpiration, the cooling reduces. Since each additional tree row results in a lower wind speed due to the increased momentum drag, the lower CHTC and CMTC result in a reduction of transpiration and a reduced cooling of the air downstream of the tree row Fig. 1.16b. When the trees does not transpire, an increase in the number of tree rows causes more heating of the flow. Reversely, transpiration ensures that the air domain is cooled regardless of the number of tree rows. The study of the impact of number of tree rows on the thermal comfort Fig. 1.16c shows that there is large change in the thermal comfort comparing transpiring and non-transpiring conditions. The transpirative cooling provided by the trees regulates the thermal comfort downstream of the tree row. The absence of transpiration yields growing deterioration of the thermal comfort with an increasing number of tree rows. Thus, the transpirative cooling effect plays a critical role when increasing the number of tree rows in the domain.

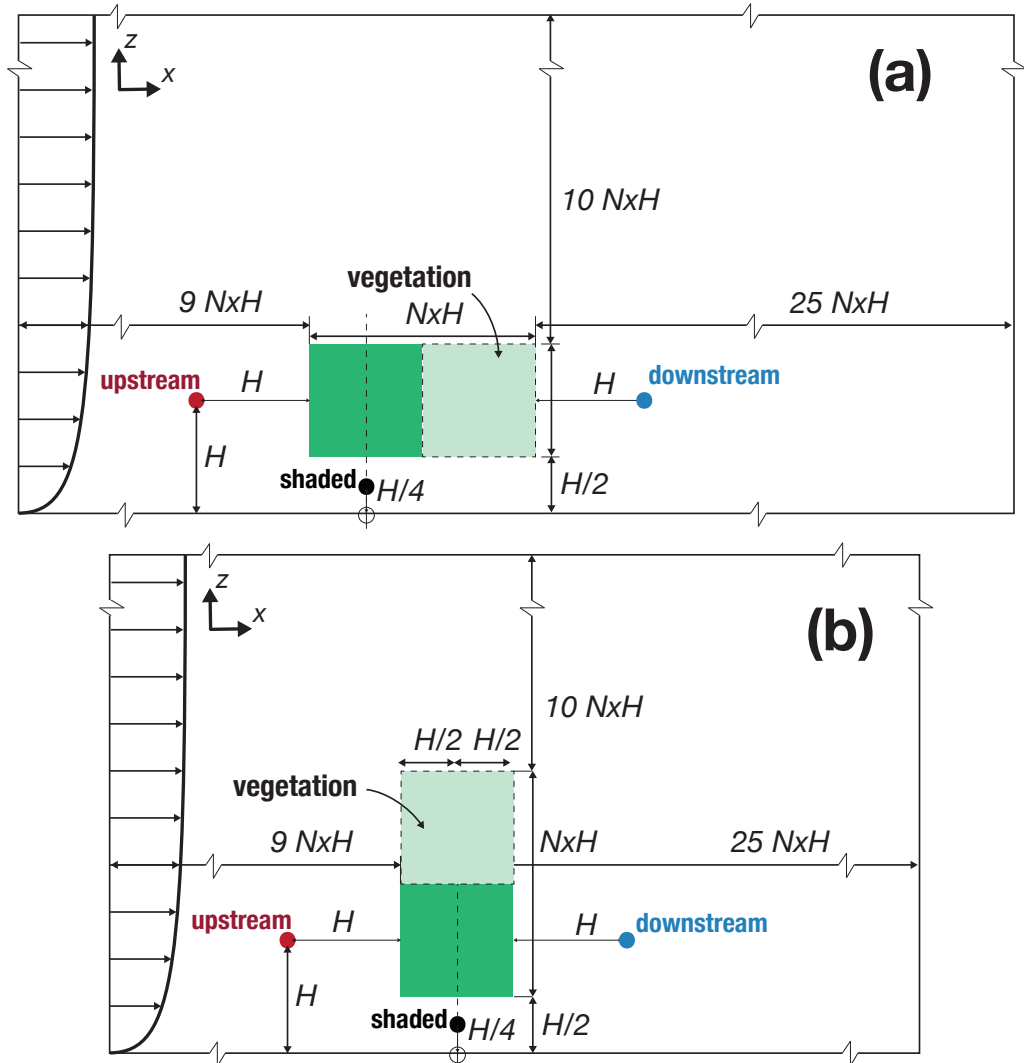


Figure 1.15: Simulation domain for the study on the size of vegetation, where vegetation region is indicated in green (■), **(a)** study on the number of tree rows $n = [1, 2, 5, 10]$, and **(b)** study on the tree height nH with $n = [1, 2, 3, 5, 10]$. The sample points at three locations: *upstream* (red), *downstream* (blue) and *shaded* (black).

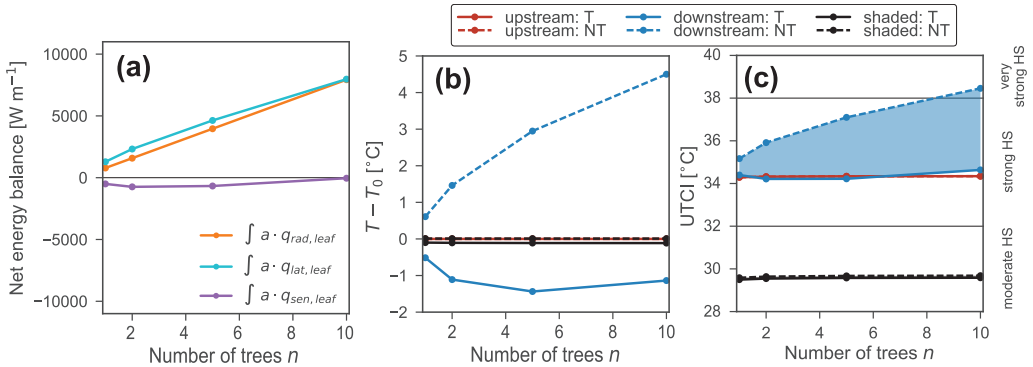


Figure 1.16: Influence of number of tree rows n on (a) the net energy balance of radiation, sensible and latent heat fluxes at the trees, $\int a \cdot (q_{rad,leaf} - q_{sen,leaf} - q_{lat,leaf}) dA = 0$ W m⁻², (b) on air temperature $T - T_0$ (°C), and (c) UTCI (°C). Point measurement of air temperature and UTCI at three locations as shown in Fig. 1.15: upstream (red), downstream (blue) and shaded (black) for transpiring (T) (solid, —) and non-transpiring (NT) conditions (dashed, - - -).

1.13.2 Influence of tree height

Fig. 1.17a shows the influence of tree height on the net energy balance. The solar radiation absorbed by the trees does not change with increasing height as the top of the trees has absorbed all the incident solar radiation independently from tree height. However, the magnitudes of latent and sensible heat fluxes increase linearly with tree height as there is a linear increase of leaf surfaces, thus in transpirative cooling effect. Fig. 1.17b shows that the cooling of the air at the downstream location converges to -1 °C in the transpiring condition and, for the non-transpiring condition, the temperature change approaches zero. This occurs because the top of the trees, which is hotter, is further away from the pedestrian level. Therefore, at the lower regions of the trees, the magnitude of the sensible heat flux remains uniform in height, providing equal change in air temperature. This is also evident from observing the thermal comfort, Fig. 1.17c. The UTCI does not vary after the trees are higher than 3 m. The shaded region can be assumed to be unaffected by the change in tree height as indicated by a negligible temperature change, Fig. 1.17b, and a negligible UTCI change, Fig. 1.17c.

1.13.3 Summary on the influence of vegetation size

The study on the influence of vegetation size is performed by varying the tree height and the number of tree rows. An increase in the number of tree rows has an influence on the CHTC and the CMTC due to the reduction in wind speed. A reduced wind speed results in a lower transpiration leading to a reduced transpirative cooling effect of the air. We also observe that, when increasing the number of tree rows, if the trees do not transpire, the thermal comfort continues to deteriorate. Therefore, transpiration plays a critical role when increasing the number of tree rows. A study on the influence of tree height shows that the top of the trees, which is hotter

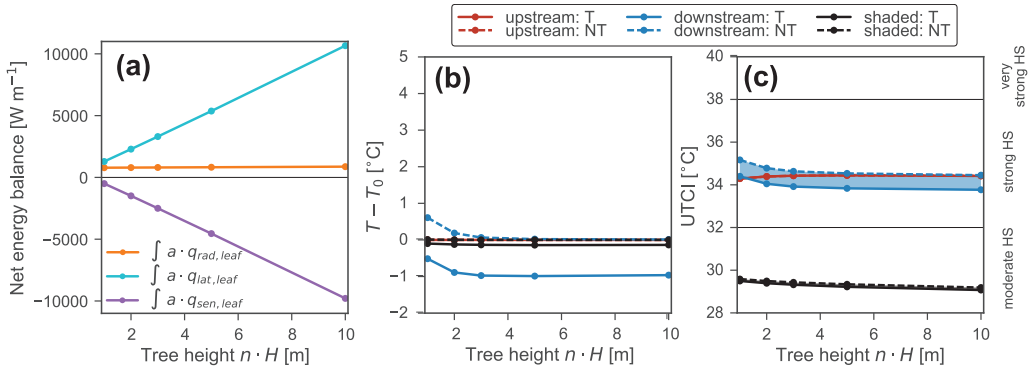


Figure 1.17: Influence of tree height nH (m) on (a) the net energy balance of radiation, sensible and latent heat fluxes at the trees, $\int a \cdot (q_{rad,leaf} - q_{sen,leaf} - q_{lat,leaf}) dA = 0 \text{ W m}^{-2}$, (b) on air temperature $T - T_0$ ($^{\circ}\text{C}$), and (c) UTCI ($^{\circ}\text{C}$). Point measurement of air temperature and UTCI at three locations as shown in Fig. 1.15: upstream (red), downstream (blue) and shaded (black) for transpiring (T) (solid, —) and non-transpiring (NT) conditions (dashed, - - -).

and is far high enough from the ground, the thermal comfort at pedestrian level is higher. This indicates that ideally, cities should focus on implementing a combination of tall wide-canopy trees and dense foliated pedestrian-level trees. The tall wide-canopy trees can provide shading to the building surfaces, and the warmer leaves are also further away from the pedestrian level to not have a negative influence on the thermal comfort. Furthermore, the densely foliated pedestrian-level trees can provide transpirative cooling and generate cool oasis at the ground level.

1.14 CONCLUSION

In this study, we investigated the influence of environmental factors, tree properties and size on the transpirative cooling effect of a single row of trees. A computational fluid dynamics (CFD) model is used for modelling the flow in the air domain and through the vegetation. Vegetation is modelled as a porous medium where the heat exchange is solved using a leaf energy balance model. The long-wave radiative transfer between vegetation and the environment is empirically modelled. The vegetation model is validated against the numerical and experiment study of Kichah et al. (2012). Thereafter, a parametric study is performed to determine the transpirative cooling effect of vegetation at noon with a solar altitude of 90° . The following conclusions were determined from the parametric study:

1. The transpirative cooling effect of a single row of trees is highest at lower wind speed when $U < 1 \text{ m s}^{-1}$.
2. A pedestrian perceives transpirative cooling mainly when wind speeds are low, as indicated by the UTCI showing a cool zone locally around the trees. However, trees extract more sensible heat from the flow by transpiration when wind speeds are higher.

3. The transpirative cooling effect of a row of trees is diminished in humid and low temperature conditions, where the vapor pressure of air is closer to saturation and the transpiration from vegetation diminishes. Cities in such climatic condition should develop mitigation strategies focusing on cooling by shading and less on maximizing transpirative cooling.
4. Solar radiation has a large influence on the thermal comfort and, in all cases, the comfort level below the trees is substantially higher than downstream of the tree row due to shadowing effects. The additional benefit of transpirative cooling is smaller, since solar radiation is found to be the dominant factor in the thermal comfort.
5. The tree properties, leaf size l and minimum stomatal resistance $r_{s,min}$, have a small influence on the transpirative cooling effect of vegetation, compared to the environmental factors such as wind speed, temperature and relative humidity.
6. The transpirative cooling effect of vegetation depends on its leaf area density due to the coupled effect on both wind speed and air temperature.
7. An increase in vegetation height is beneficial as the top of the trees with higher leaf temperatures is further from the pedestrian level. This ensures that the transpirative cooling effect is high at the pedestrian level.
8. If vegetation does not transpire, increasing the number of tree rows result in an increase in air temperature and UTCI downstream of the vegetation.
9. In general, cities should use a combination of tall wide-canopy trees, that can provide shading to urban surfaces, and pedestrian-level trees, that can provide transpirative cooling near the ground. Such combination can maximize the cooling through shading and transpiration.

Future studies will consider the long-radiative exchanges between terrestrial objects and varying solar altitude. This enables to study the influence of vegetation in urban areas and understand the thermal role of the ground and buildings on the transpirative cooling effect of vegetation. Furthermore, the influence of water availability at the roots on the transpiration rate and the impact on transpirative cooling effect will be studied.

2

COMPARISON OF WIND TUNNEL MEASUREMENT AND CFD OF A SMALL PLANT

In this chapter, we compare the numerical method described in Chapters 1 and 3 with the measurements of ???. The measurements were performed for a small *Buxus sempervirens* plant. The measurements consisted of: i) X-ray tomography measuring plant microstructure metrics such as net leaf area and leaf area density, ii) stereoscopic particle image velocimetry (SPIV) measuring the wake flow properties such as mean velocity and turbulence kinetic energy (TKE), iii) infrared thermography measuring the spatiotemporal leaf temperature profile, and iv) hygrothermal in-foliage measurement probes measuring the vertical distribution of relative humidity (RH) and air temperature. Therefore, the goal of the present study is to compare the numerical simulation of the Buxus plant setup using the porous medium approach detailed in this thesis and compare with the high-resolution dataset to quantify the discrepancies. The present study aims at providing insight to the feasibility of employing such numerical techniques and possible limitation.

2.1 SIMULATION DOMAIN AND BOUNDARY CONDITION

The simulation setup consisting of the numerical domain and its boundary conditions were that of the wind tunnel experiment with wind tunnel set wind speed $U_{ref} = 1 \text{ m s}^{-1}$. The reference velocity used for the study is the plant-canopy height velocity $U_H = 0.77 \text{ m s}^{-1}$ at $H = 0.21 \text{ m}$.

2.1.1 Numerical domain

The numerical domain is based on the geometry of the wind tunnel test-section with a wind tunnel height $H = 1.6 \text{ m}$ and a lateral dimension $W = 1.9 \text{ m}$, as depicted in Fig. 2.1. The downstream fetch of the numerical domain after the plant was extended to ensure a developed flow at the outlet of the numerical domain.

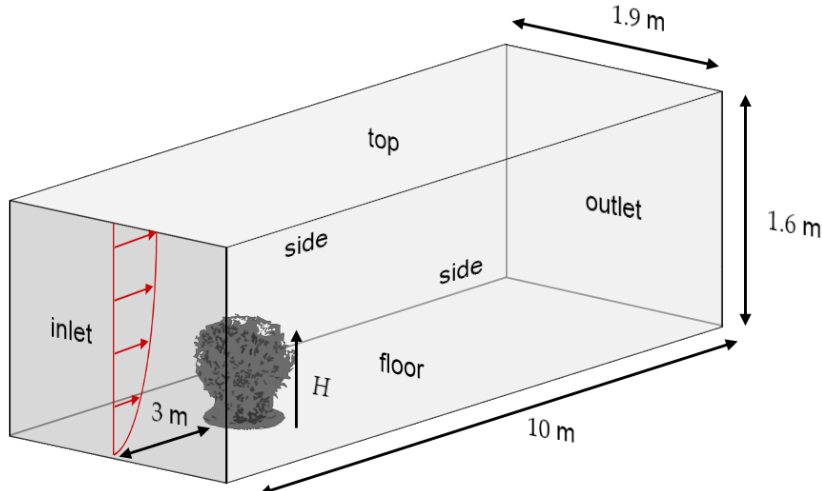


Figure 2.1: Numerical domain used for the wind-tunnel-CFD comparison study with plant-canopy height $H = 0.21$ m (not to scale).

2.1.2 Boundary conditions

Fig. 2.2 shows the upstream boundary condition of mean velocity \bar{u} (m s^{-1}) and the turbulent kinetic energy k obtained from the wind tunnel experiment. An atmospheric boundary layer (ABL) profile, described through the following three equations (Richards and Hoxey 1993):

$$\bar{u}(z) = \frac{u_*}{\kappa} \ln \left(\frac{z + z_0}{z_0} \right) \quad (2.1)$$

$$k = \frac{u_*^2}{\sqrt{C_\mu}} \quad (2.2)$$

$$\varepsilon = \frac{u_*^3}{\kappa(z + z_0)} \quad (2.3)$$

were used as the boundary condition at the inlet of the numerical domain, where $\bar{u}(z)$ (m s^{-1}) is the mean horizontal velocity, $u_* = 0.062336 \text{ m s}^{-1}$ is the friction velocity, $\kappa = 0.41$ is von Kármán constant, $z_0 = 0.001335 \text{ m}$ is the aerodynamic roughness height and $C_\mu = 0.09$. The roughness height z_0 and the friction velocity u_* were obtained using curve-fit of the measured PIV profile (see Fig. 2.2), resulting in an inlet turbulent intensity of $I = \sqrt{2/3 k}/U_{ref} = 12.1\%$. The outlet boundary condition is defined as pressure outlet with a static pressure $p = 0$. A zero-gradient boundary condition was enforced for \mathbf{u} , k , and ε . The remaining boundaries (i.e., top-wall and side-walls) are modeled as no-slip wall-boundary and with standard wall functions.

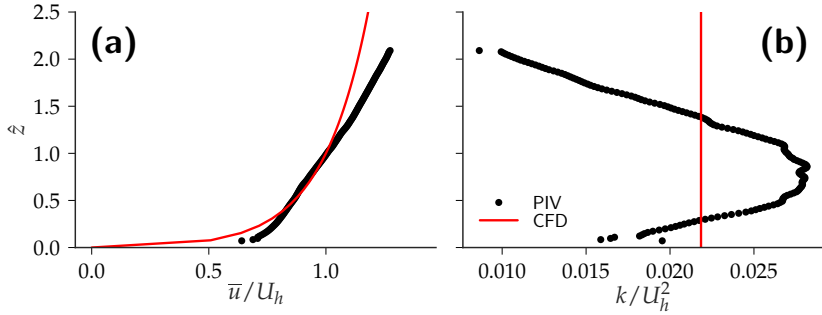


Figure 2.2: Vertical profiles of incoming normalized **(a)** mean streamwise velocity \bar{u}/U_h and **(b)** turbulent kinetic energy k/U_h^2 : (black) PIV profile from wind tunnel and (red) CFD boundary condition.

2.1.3 Leaf area density

The vegetation is modeled as a porous medium parameterized using a leaf area density a ($\text{m}^2 \text{ m}^{-3}$) distribution and a constant leaf drag coefficient c_d . The momentum source term s_u (N m^{-3}) is given as:

$$s_u = -\rho c_d a |\bar{\mathbf{u}}| \bar{\mathbf{u}} \quad (2.4)$$

$$s_k = \rho c_d a \left(\beta_p |\bar{\mathbf{u}}|^3 - \beta_d |\bar{\mathbf{u}}| k \right) \quad (2.5)$$

$$s_\varepsilon = \rho c_d a \left(\beta_p C_{4\varepsilon} |\bar{\mathbf{u}}|^3 \frac{\varepsilon}{k} - \beta_d C_{5\varepsilon} |\bar{\mathbf{u}}| \varepsilon \right) \quad (2.6)$$

where c_d is the leaf drag coefficient (Wilson and Shaw 1977) and experimental measurements suggesting that $c_d \in [0.2, 0.5]$ (Vogel 1989). The closure coefficients $C_{4\varepsilon} = 0.9$ and $C_{5\varepsilon} = 0.9$ are obtained from literature (Katul, Mahrt, et al. 2004; Kenjereš and Ter Kuile 2013; Sanz 2003). The coefficients $\beta_p = 1.0$ and $\beta_d = 5.1$ are energy conversion ratio from MKE to TKE and TKE to heat, respectively. The valid parameters are dependent on the specific plant type and plant sample and require calibration. In this study, the X-ray tomography measured is used to determine the leaf area density a distribution. Thereafter, the values are interpolated onto the numerical domain. In the present study, a simple tri-linear interpolation scheme is employed to interpolate onto the finite volume cells. The leaf area density a is derived as:

$$a = \frac{1}{2} A_l \frac{1 - \phi}{\int 1 - \phi \, dV} \quad (2.7)$$

where A_l (m^2) is the net plant leaf area (both sides of the leaves) and ϕ is the plant porosity.

2.1.4 Numerical solution

The problem is solved using the SIMPLE pressure-velocity coupling algorithm, obtaining a steady-state solution. The gradient terms are discretized using Gauss integration and interpo-

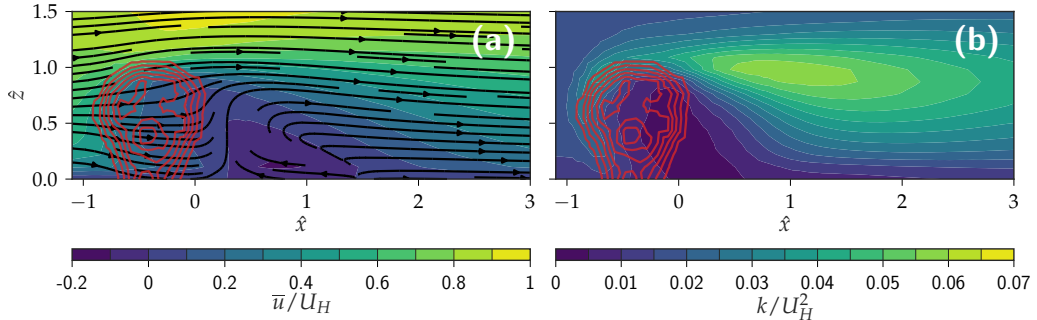


Figure 2.3: Vertical plane at the center-line (i.e., at $\hat{y} = 0$) showing the normalized **(a)** streamwise velocity $|\bar{u}|/U_H$ and **(b)** turbulent kinetic energy k/U_H^2 around the plant. The heterogeneous leaf area density a is indicated with red iso-contour lines of $a = [20, 40, 60, 80, 100, 120, 140] \text{ m}^2 \text{m}^{-3}$. The drag coefficient is $c_d = 0.5$. Note that the corrected reference velocity $U_H = 0.95 \text{ m s}^{-1}$ is used (Blocken et al. 2007).

lated using second-order central differencing scheme (linear). Similarly, the divergence terms are interpolated using second-order linear upwind differencing scheme (linearUpwind). The pressure is solved using geometric-algebraic multi-grid (GAMG) solver and preconditioned with diagonal incomplete-Cholesky (DIG) smoother, whereas velocity is solved using Preconditioned bi-conjugate gradient (PBiCG) solver with diagonal incomplete-LU (DILU) preconditioner. The matrix solvers are iteratively solved until the residuals of pressure are below 1×10^{-5} and below 1×10^{-6} for all the other variables. Furthermore, under-relaxation factors are used with $\alpha_p = 0.3$ for pressure, $\alpha_u = 0.7$ for velocity (ensuring $\alpha_p + \alpha_u = 1$) and $\alpha_k = \alpha_e = 0.5$. The under-relaxation factors are modified to $\alpha_p = 0.7$ and $\alpha_u = 0.3$ for the non-isothermal case to ensure stable convergence.

2.2 ISOTHERMAL CASE

The comparison of the CFD simulation and the wind tunnel results are split into two section: *isothermal* case and *non-isothermal* case. In the isothermal case, the influence of the leaf area density distribution, plant drag coefficient, and the turbulence model is investigated. A preliminary assessment of the discrepancy between CFD and wind tunnel results is performed by comparing the mean velocity and TKE of the plant wake. Thereafter, the non-isothermal case investigates the vertical profile of the air temperature and relative humidity for both the daytime and nighttime conditions.

Fig. 2.3 shows the streamwise velocity $|\bar{u}|/U_H$ and TKE k/U_H^2 due to the plant. The leaf area density is depicted using the iso-contour lines of $a = [20, 40, 60, 80, 100, 120, 140] \text{ m}^2 \text{m}^{-3}$ determined using Eq. (2.7). It is seen to vary in space with peak density located approximately in the middle of the plant ($\hat{x} = -0.5$, $\hat{z} = 0.5$). A modification to the reference velocity for the numerical model is seen to be necessary due to the bias in the CFD prediction. The airflow and TKE is seen to be consistently over-predicted. However, with a corrected reference velocity of $U_H = 0.95 \text{ m s}^{-1}$ the flow field is seen to be in better agreement. The source of the bias is assumed

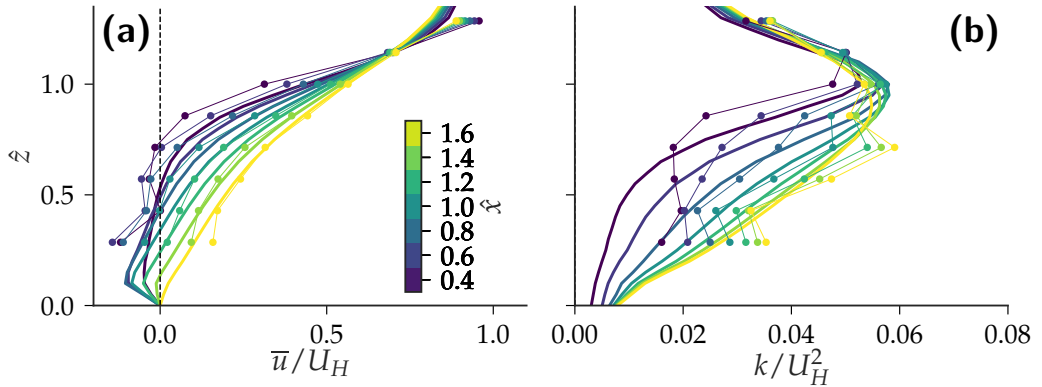


Figure 2.4: Mean normalized vertical profiles at 7 streamwise positions \hat{x} , at center-line of the plant $\hat{y} = 0$: (a) streamwise velocity $|\bar{u}|/U_H$ and (b) turbulent kinetic energy k/U_H^2 . Note that $U_H^{exp} = 0.77 \text{ m s}^{-1}$ and $U_H^{num} = 0.77 \text{ m s}^{-1}$.

to be the ABL inlet boundary condition. An apparent amplification of the velocity and TKE is observed in the CFD results, and similar finding has been observed by Blocken et al. (2007). However, a rigorous study of the source of the bias has not performed for this study. The vertical plane velocity field is plotted together with the streamlines (Fig. 2.3a). The near-wake of the plant is consists of a recirculation zone below $\hat{z} = 0.5$, indicated by negative stream-wise velocity. The highest TKE is observed at the plant-canopy height $\hat{z} = 1$, with peak TKE at approximately $\hat{x} = 1$. Therefore, the wake turbulence is seen to dominantly affected by the shear-zone generated by the plant canopy.

A preliminary comparison of the numerical prediction and the experimental measurement is performed by comparing the stream-wise velocity and the TKE at $\hat{x} = [0.4, 0.6, 0.8, 1.0, 1.2, 1.4, 1.6]$. Fig. 2.4 shows the vertical profiles at these seven locations, where the lateral position is at the plant center-line (i.e., $\hat{y} = 0$). The comparison shows a reasonably accurate prediction of the near-wake statistics of the plant. The prediction especially demonstrates an accurate prediction of the magnitude and the gradient of the stream-wise velocity. Although, very close to the tree, $\hat{x} < 0.6$, the deficit in the velocity is seen to be under-predicted. The TKE shows a good comparison as well with an accurate prediction of the peak TKE at the plant-canopy shear-layer. However, as with the stream-wise velocity, very close to the tree, there is a slight overestimation. Furthermore, the variability in height is seen to less severe than the experimental observation. This is most likely due to the numerical approach being a porous media approach where instead of explicitly resolving the plant elements (i.e., branches and leaves), they are aggregated into a distribution function.

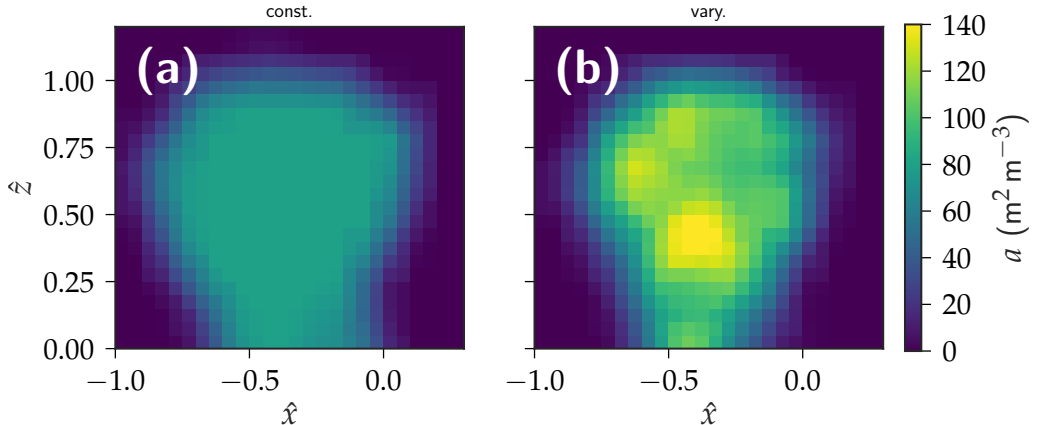


Figure 2.5: Two types of leaf area density a distribution: **(a)** constant distribution and **(b)** varying distribution.

2.2.1 Influence of heterogeneity in leaf area density distribution

The influence of heterogeneity in the leaf area density distribution is investigated by comparing a spatially *varying* leaf area density and a spatially *constant* (average) leaf area density. Applying a spatial averaging operator to Eq. (2.7), we obtain the average leaf area density $\langle a \rangle (\text{m}^2 \text{m}^{-3})$ as:

$$\langle a \rangle = \frac{1}{2} A_l \frac{1 - \langle \phi \rangle}{\int 1 - \phi \, dV} \quad (2.8)$$

where it is simply related to net leaf area A_l and the average plant porosity $\langle \phi \rangle$. Therefore, the constant leaf area density distribution function in the air domain Ω_a is defined:

$$a(\mathbf{x}) = \begin{cases} \langle a \rangle & \text{if } 0 \leq \phi < 1 \\ 0 & \text{if } \phi = 1 \end{cases} \quad (2.9)$$

Fig. 2.5 shows the two types of leaf area density distribution at $\hat{y} = 0$. A spatially-averaged leaf area density is seen to be around $\langle a \rangle \approx 80 \text{ m}^2 \text{m}^{-3}$, with maximum leaf area density $\max(a) = 140 \text{ m}^2 \text{m}^{-3}$.

To study the impact of heterogeneity in leaf area density distribution, both cases are compared with the wind tunnel measurements. Fig. 2.6 shows the horizontal profile of stream-wise velocity and turbulent kinetic energy at three heights $\hat{z} = [0.29, 0.71, 1]$. The figure reveals that both constant and varying leaf area density distribution shows similar behavior where the more realistic description of the varying leaf area density distribution is seen to provide better predictions. The stream-wise velocity profile shows that the numerical model under-predicts the peak wake velocity deficit at all heights. Furthermore, the wake recovery from the numerical model is seen to be slower than the measurements. Therefore, the recirculation length of the numerical model is seen to be larger than in reality. One of the possible contributing factors to the recirculation

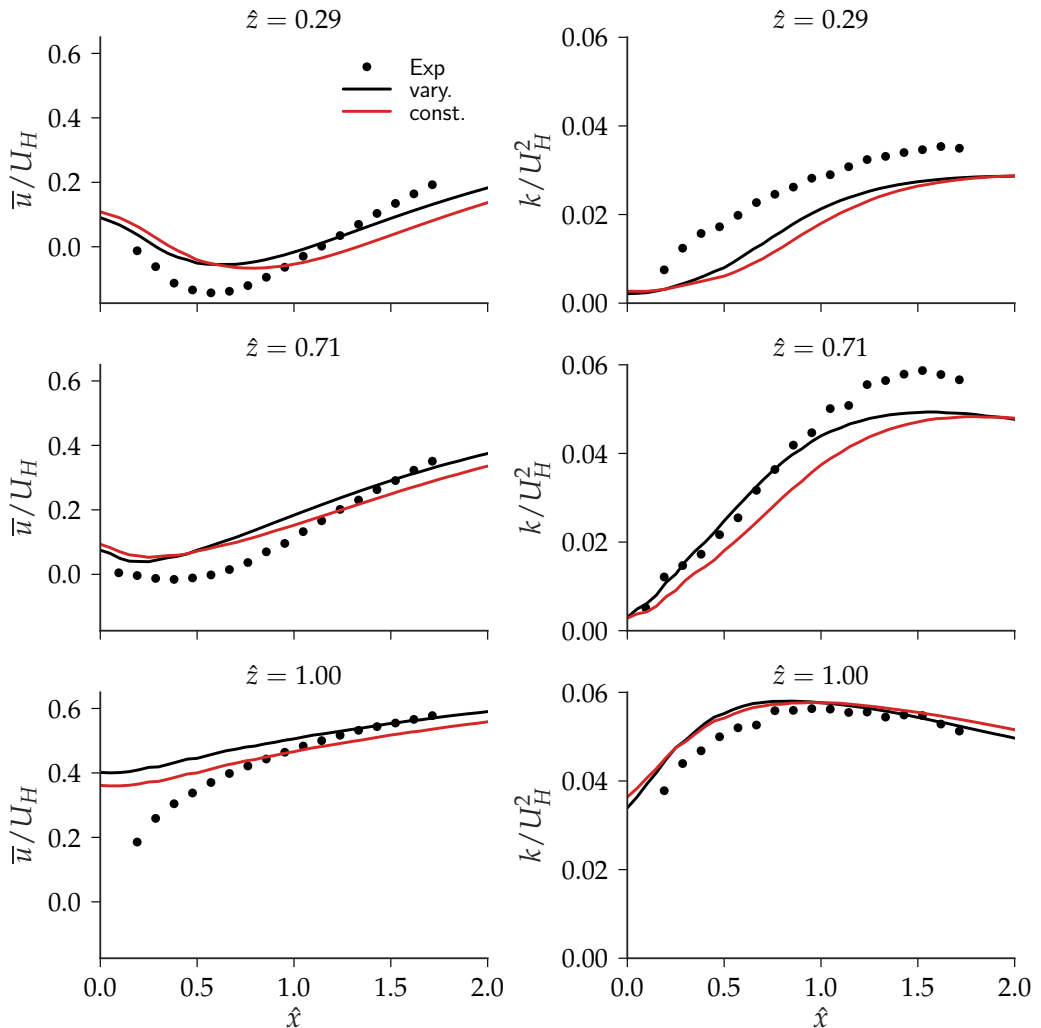


Figure 2.6: Influence of constant and varying leaf area density a ($\text{m}^2 \text{ m}^{-3}$): Horizontal profile of normalized stream-wise velocity \bar{u}/U_H and turbulent kinetic energy k/U_H^2 at heights $\hat{z} = [0.29, 0.71, 1]$.

length is the accuracy of the turbulence closure. Therefore, the influence of the turbulence model is investigated in more detail.

2.2.2 *Influence of plant drag coefficient*

A second plant property that determines the net influence of the vegetation on the flow is the drag coefficient c_d in Eqs. (2.5) to (2.6). Generally, the drag coefficient is associated with the leaf drag coefficient and determined to be $c_d \in [0.2, 0.5]$ (Vogel 1989; Wilson and Shaw 1977). However, as there is a high quantity of branch elements in the small Buxus plant, the validity of the assumption is investigated by a parametric study on the drag coefficient.

Fig. 2.7 shows the horizontal profile of stream-wise velocity and turbulent kinetic energy at three heights $\hat{z} = [0.29, 0.71, 1]$, and the influence of drag coefficient on them. We observe clearly that the numerical prediction convergently approaches to the experimental results as c_d increases. Therefore, there is a clear indication that the drag coefficient of the plant is not just that of the leaf but should also take into account the contribution of the remaining plant elements such as branches. However, the wake velocity deficit still shows a slight under-prediction. Similarly, in the wake zone (i.e., $\hat{z} < 1$), the peak TKE is under-predicted.

2.2.3 *Influence of turbulence model*

For the study of the turbulence model, four similar closure approaches were investigated: i) the standard $k - \varepsilon$ without vegetation terms, ii) the standard realizable $k - \varepsilon$ without vegetation terms, iii) the porous $k - \varepsilon$ with vegetation terms, and iv) the porous realizable $k - \varepsilon$ with vegetation terms.

Fig. 2.8 shows the influence the four turbulence closure approaches on the stream-wise horizontal profile of stream-wise velocity u and turbulent kinetic energy k at three heights $\hat{z} = [0.29, 0.71, 1]$. The study shows the clear importance of an accurate turbulence closure to obtain the real observed plant wake. Let us first look at the influence of the turbulence model by comparing standard $k - \varepsilon$ and realizable $k - \varepsilon$. We see that this change already has a good improvement to the numerical prediction. The realizable turbulence model is seen to outperform the normal $k - \varepsilon$ model providing more realistic velocity deficit and reduces the overestimation of the TKE. However, we see that the turbulence closure terms of the vegetation have a significantly more impact on the accuracy of the prediction. By adding the vegetation terms, i.e., the porous std. $k - \varepsilon$ is seen to be drastically better than the simple change of turbulence model from $k - \varepsilon$ to the more accurate realizable $k - \varepsilon$. We see that, not only is the wake velocity deficit more pronounced as with observation, but the TKE at the vicinity of the plant is seen to drastically less over-predicted. Therefore, the impact of foliage, such as the TKE suppression from the fluid-structure interaction of the foliage and airflow, is seen to be an important aspect of vegetation. As the standard turbulence models do not model such shortcuts in turbulence cascade (i.e., from TKE to heat), an over-prediction of turbulence is observed. The best performance in prediction accuracy is seen to be obtained from the porous realizable $k - \varepsilon$ model, where the stream-wise velocity deficit and the magnitude of the TKE is predicted with good accuracy. However, at the plant-canopy height (i.e., $\hat{z} = 1$), very close to the foliage (i.e., $\hat{x} \rightarrow 0$), the strong plant

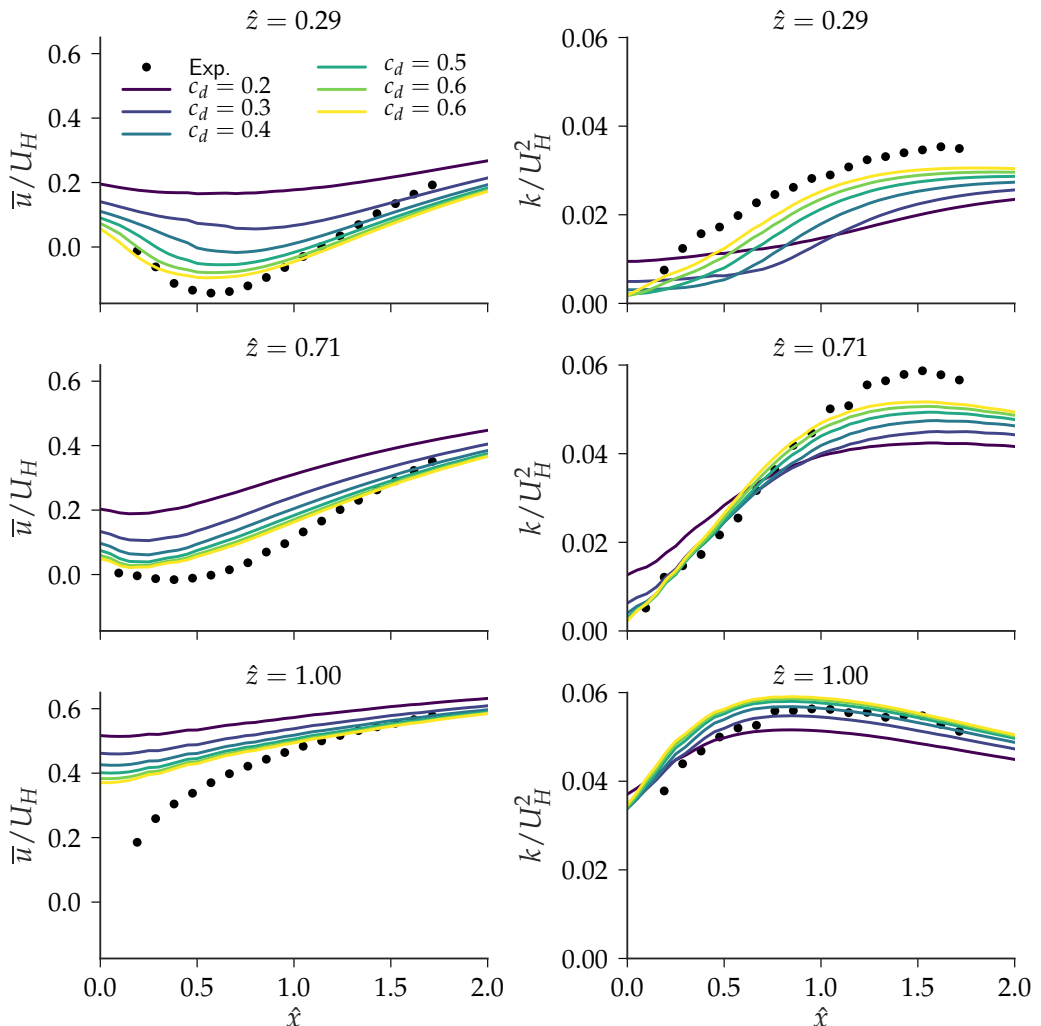


Figure 2.7: Influence of drag coefficient $c_d = [0.2, 0.3, 0.4, 0.5, 0.6]$: Horizontal profile of normalized stream-wise velocity \bar{u}/U_H and turbulent kinetic energy k/U_H^2 at heights $\hat{z} = [0.29, 0.71, 1]$.

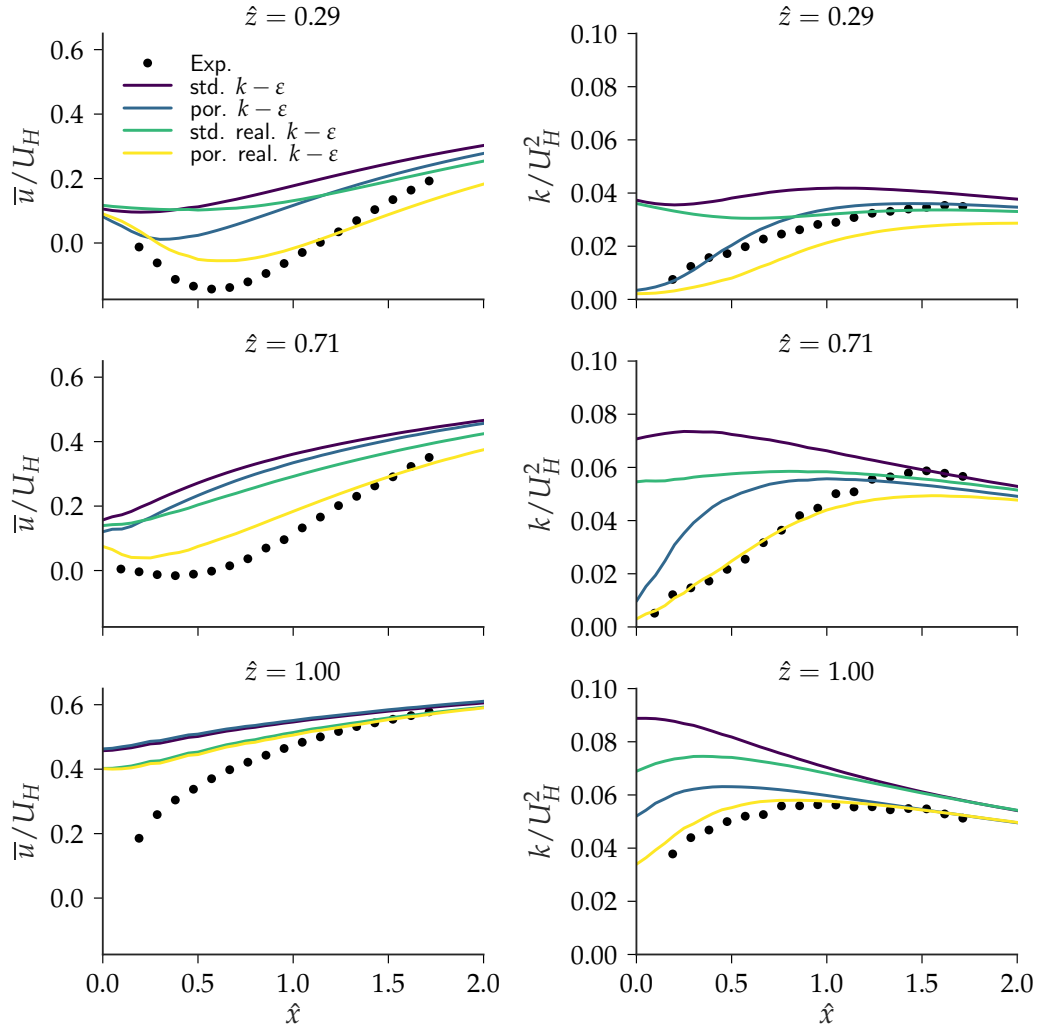


Figure 2.8: Influence of turbulence model std. $k - \varepsilon$, std. real. $k - \varepsilon$, por. $k - \varepsilon$ and por. real. $k - \varepsilon$: Horizontal profile of normalized stream-wise velocity \bar{u}/U_H and turbulent kinetic energy k/U_H^2 at heights $\hat{z} = [0.29, 0.71, 1]$.

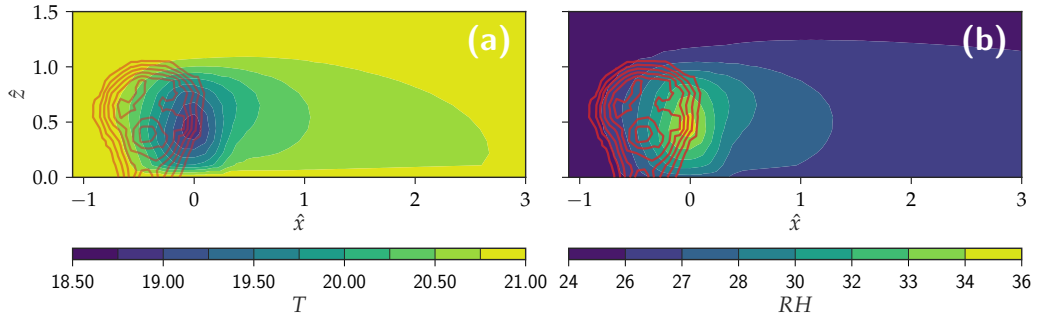


Figure 2.9: Center-plane (i.e., $y = 0$) hygrothermal condition of the flow at day-time with $T = 21$ $^{\circ}\text{C}$, $RH = 25\%$ and $q_{r,sw,0} = 100 \text{ W m}^{-2}$: (a) air temperature T ($^{\circ}\text{C}$) and (b) relative humidity RH (%).

wake velocity deficit is not captured. This could be fundamentally due to the shortcomings of a porous media and similar immersed boundary approach where boundary layer flow phenomena are weakly captured. The flow characteristics prevalent the interfaces such as shear-flow are no longer captured with such spatial definition and intensity.

An additional aspect of the turbulence closure is the model coefficients such as c_μ , $C_{1\epsilon}$, $C_{2\epsilon}$, $C_{4\epsilon}$, $C_{5\epsilon}$, β_p and β_d . These are also typically referred to as *free* coefficients and typically requires rigorous calibration (i.e., tuned) to capture and recover the experimental observations. The calibration of these coefficient to the experiment results can be described as an optimization problem (Gorlé2013; Couplet et al. 2005; Duraisamy et al. 2018; Gorlé et al. 2015; Lucor et al. 2007; Margheri et al. 2014; Najm 2009), where data assimilation techniques are well regarded as an effective methodology to ensure the accurate, efficient convergence to global optima:

$$\arg \min_c \varepsilon(\mathbf{x}, \mathbf{c}) = \|\mathcal{N}(\mathbf{x}) - \mathcal{M}(\mathbf{x}, \mathbf{c})\|_2 \quad (2.10)$$

where $\mathbf{c} = (c_\mu, c_{1\epsilon}, c_{2\epsilon}, c_{4\epsilon}, c_{5\epsilon}, \beta_p, \beta_d)^T$ is a vector of the free coefficients and \mathbf{c} spans \mathbb{R}^7 , \mathcal{N} is the true Navier-Stokes solution (neglecting the experimental uncertainties) and \mathcal{M} is the numerical model. Therefore, the numerical model can be regarded as a “black-box” simply dependent on the free coefficient vector \mathbf{c} . We see that a brute-force search for coefficient vector \mathbf{c} that minimizes the error ε is intangible as the search needs to be formed in a 7-dimensional space, requiring a rigorous search algorithm. Therefore, the calibration of the turbulence model is beyond the scope of the study, but an important aspect for future studies.

2.3 NON-ISOTHERMAL CASE

Finally, the numerical prediction of the thermal impact of the plant is compared with the hygrothermal wind tunnel measurements with ambient conditions $T = 21$ $^{\circ}\text{C}$, 25% relative humidity and plant-canopy incident solar radiation levels $q_{r,sw} = [0, 100]$ W m^{-2} . The temperature and humidity equations are solved as passive scalar where the plant source is determined using the leaf energy balance approach described in Chapter 1. Additionally, the resistance-based

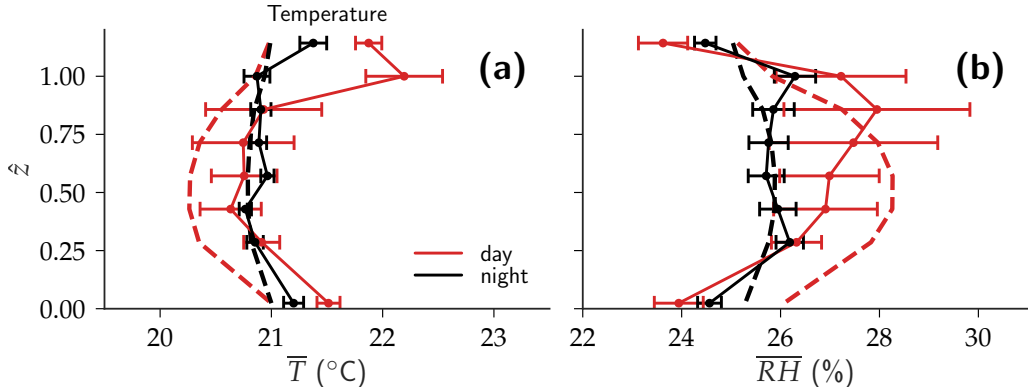


Figure 2.10: Comparison of wind tunnel (solid) and numerical simulation (dashed): **(a)** Air temperature T ($^{\circ}\text{C}$) and **(b)** relative humidity RH (%)

aerodynamic and stomatal models described in the chapter are used to parameterise the heat and mass flux between the foliage and air. The minimum stomatal resistance of the plant is set to $r_{s,min} = 400 \text{ s m}^{-1}$, a typical value for deciduous plants (Baille et al. 1994; Bruse and Fleer 1998). Furthermore, it is equivalent to a stomatal conductance of $k_{st} = 40 \text{ mmol m}^{-2} \text{ s}^{-1}$, typical of a *Buxus sempervirens* (Letts et al. 2012; Rodriguez-Calcerrada et al. 2013). In our study, the characteristic plant leaf size is set to $l = 3 \text{ cm}$, obtained from measurements.

Fig. 2.9 shows the temperature and relative humidity at the center-plane of the plant ($y = 0$) during day time. A peak temperature drop of approximately $\Delta T = -2.5 \text{ }^{\circ}\text{C}$ and humidity rise to $\Delta RH = +12\%$ is observed near the mid-aft region of the plant ($\hat{x} = 0$, $\hat{z} = 0.5$). We also note that there is no observed heating of the flow, typically present at the plant canopy height, possibly due to the lower level of incident solar radiation $q_{r,sw,0} = 100 \text{ W m}^{-2}$ and high convective heat transfer arising from the presence of wind. To accurately assess the discrepancy between the hygrothermal prediction and the experiment observation, the in-foliage air temperature, and relative humidity are compared at various vertical locations. Fig. 2.10 shows the vertical profile of the air temperature and relativity humidity during day and night where the results of the numerical simulation are plotted with dashed lines. In general, we see a good agreement with the numerical predictions and the experimental measurements. Although, we see that there is a slight overestimation of the transpirative cooling indicated by slightly lower air temperature and a slightly higher relative humidity during the daytime. The air temperature is seen to have the highest discrepancy at the top region of the foliage, where the solar radiation is intercepted. The air temperature is seen to be higher than ambient from the experimental observations. However, in the simulation, the air temperature is only seen to be lower than ambient indicating that a heat of the air, due to excess radiation absorption, is not numerically predicted. The numerical model predicts a transpiration rate enough to reduce the air temperature. Comparing the relative humidity profiles, we see that the peak humidity from simulations is seen in the middle region of the plant (i.e., $\hat{z} = 0.5$). At night, the hygrothermal parameters are well predicted with a minimal discrepancy.

A more general assessment on the prediction of the plant transpiration can be assessed by examining the net plant transpiration rate during day and night. Table 2.1 shows the experimental and numerical value of the net transpiration rate TR (g h^{-1}) during day and night. The comparison validates the finding that numerical model predicts a high transpiration rate. Especially during the daytime, a very high transpiration rate of 17.6 g h^{-1} is predicted in contrast to the mean transpiration rate of 5.8 g h^{-1} and a peak transpiration rate of 14.8 g h^{-1} . During the night, the net transpiration rate is predicted to be 4.9 g h^{-1} , whereas the experimental observation suggests a mean and peak value of 3 and 8.6 g h^{-1} , respectively. Therefore, the numerical prediction of the plant transpiration is equivalent to the maximum plant transpiration rate. This indicates that time-dependent stomatal regulatory phenomena, as observed in chapter ??, is not modeled using the presently used stomatal model. Furthermore, the comparison shows a need for a more rigorous modeling plant response to take into account dynamic plant responses.

Table 2.1: Experimental and numerical values of net plant transpiration rate $TR = dm/dt$ (g h^{-1}) during day and night.

period	experimental		numerical
	mean	max.	
day	5.8	14.8	17.6
night	3.0	8.6	4.9

3

NUMERICAL MODEL FOR MODELING VEGETATION IN URBAN AREA

3.1 INTRODUCTION

The simplified vegetation model is described in Chapter 1 introduction the governing equation for moist flow vegetation. The vegetation model provides the necessary source/sink terms for heat, mass and momentum exchanges between vegetation and air as described in Section 1.4. Furthermore, radiation transfer within vegetation is also described in Section 1.7. For reader, a detailed derivation of the thermodynamic of the moist air is given in ?? and a detailed derivation of the governing equation of moist flow is given in ??.

In this chapter, the numerical method for modeling vegetation inside an urban area is described. The chapter focuses on coupling of the vegetation model with the of heat (incl. radiation) and mass fluxes of the urban surfaces. The governing equation for the the coupled heat and moisture transport in the porous material is first described.

3.2 GOVERNING EQUATIONS OF COUPLED HEAT AND MOISTURE TRANSPORT

3.2.1 *Composition of the porous material*

The building materials and the soil is considered as a porous material consisting of three phases: solid phase (denoted with s), liquid phase referring to liquid water (l) and the air phase which is split into dry air (a) and water vapor v (Carmaliet2005; Defraeye 2011; Janssen 2002; Saneinejad 2013). The open porosity ϕ_o ($\text{m}^3 \text{ m}^{-3}$) of the porous material is defined as:

$$\phi_o = \frac{V_{pore}}{V} \quad (3.1)$$

where V_{pore} (m^3) is the volume of open pores and V (m^3) is the total volume of the porous material S . The solid material content w_s (kg m^{-3}) is defined as:

$$w_s = (1 - \phi_o) \rho_s \quad (3.2)$$

where ρ_s (kg m^{-3}) is the solid material matrix density. Similarly the dry air w_a , water vapor w_v , liquid water w_l contents are defined as:

$$w_l = \phi_o S_l \rho_l \quad (3.3)$$

$$w_a = \phi_o (1 - S_l) \rho_a \quad (3.4)$$

$$w_v = \phi_o (1 - S_l) \rho_v \quad (3.5)$$

where they are related to the degree of liquid saturation S_l of the porous open pores:

$$S_l = \frac{\phi_{o,l}}{\phi_o} \quad (3.6)$$

with $\phi_{o,l}$ being the amount of liquid water occupied inside the open pores and ρ_a , ρ_l being the air and liquid water densities, respectively. The total moisture content w (kg m^{-3}) inside the porous material is simply the sum of liquid water and water vapor:

$$w = w_l + w_v \quad (3.7)$$

3.2.2 Water potential

Water potential is a universal parameter for determine the water status in any medium (Nobel 2009). In the thesis, we use it to define the water status of multiple domains such as solid porous materials (soil and building facades), plant xylem, and air. The water potential ψ (Pa) describes the chemical potential of water μ (J mol^{-1}) with respect to chemical potential of pure water $\mu^{o,l}$ (J mol^{-1}) at the same temperature, standard atmosphere and at zero level:

$$\psi = \frac{\mu - \mu^{o,l}}{V_l^o} \quad (3.8)$$

where $V_l^o = 18.0510^{-3} \text{ m}^3 \text{ mol}^{-1}$ is the molar volume of pure water in liquid phase. We can see that water potential of pure water at 298 K is therefore 0 Pa. The water tends to move towards a region where $\mu - \mu^{o,w}$ is lowers, i.e. in the direction of $-\nabla\psi$. The water potential is related to due pressure potential, osmotic potential, matrix potential, and gravitational potential. In our study, we assume that the pressure potential gradient is negligible in the solid, we ignored the influence of osmotic potential ψ_o (Pa) as we assume we have a non-saline porous material and so only the matrix potential and gravitation potential influences the water transport:

$$\psi = \underbrace{p_c}_{\psi_c} + \underbrace{\rho_l g z}_{\psi_g} \quad (3.9)$$

where $\psi_c = p_c$ (Pa) is the capillary potential due to capillary pressure, and $\psi_g = \rho_l g h$ (Pa) is the gravitational potential with $g = |\mathbf{g}|$ (m s^{-2}) where \mathbf{g} is the gravitational acceleration. The

contribution of the matrix potential is represented with the capillary pressure. The capillary pressure p_c is defined as the difference between liquid p_l and the gas phase p_g :

$$p_c = p_l - p_g \quad (3.10)$$

and is related to relative humidity ϕ by the Kelvin's law:

$$p_c = \rho_l R_v T \ln(\phi) \quad (3.11)$$

The gravitational potential ψ_g (Pa) is defined as:

$$\psi_g = -\rho \mathbf{g} \cdot \mathbf{x} = \rho g z \quad (3.12)$$

where $g = |\mathbf{g}|$ with z oriented upward. Thus, by taking in account of the capillary and gravitation water potential, the transport of water can be described in building materials and more importantly, soil where the plant roots are present.

3.2.3 Coupled transport of heat and mass

The conservation of mass in the solid domain is defined as:

$$\frac{\partial w_s}{\partial t} = 0 \quad (3.13)$$

$$\frac{\partial w_a}{\partial t} + \nabla \cdot (w_a \mathbf{u}_a) = 0 \quad (3.14)$$

$$\frac{\partial w_l + w_v}{\partial t} + \nabla \cdot (w_l \mathbf{u}_l + w_v \mathbf{u}_v) = 0 \quad (3.15)$$

assuming that solid matrix does not move, mass of different phases only change due to evaporation or condensation. Other phenomena such as melting, freezing, sublimation and deposition are neglected. As we are only interested in the rate of change of moisture content $w = w_l + w_g$, we conservation of mass in the solid domain is simply:

$$\frac{\partial w}{\partial t} = -\nabla \cdot (\mathbf{g}_l + \mathbf{g}_v) \quad (3.16)$$

where \mathbf{g}_l and \mathbf{g}_v ($\text{kg m}^{-2} \text{s}^{-1}$) are liquid water and water vapor fluxes, respectively.

The conservation of energy is given as:

$$\frac{\partial h}{\partial t} + \nabla \cdot (h \mathbf{u}) = -\nabla \cdot \mathbf{q} \quad (3.17)$$

where h (J kg^{-1}) is the enthalpy of total solid domain:

$$h = \sum_i w_i h_i = w_s h_s + w_a h_a + w_l h_l + w_v h_v \quad (3.18)$$

and assuming that contribution of soil and liquid water is much higher than dry air and water vapor, we can simply to:

$$\frac{\partial}{\partial t} (w_s h_s + w_l h_l) = -\nabla \cdot \mathbf{q} - \nabla \cdot (w_l h_l \mathbf{u}_l + w_v h_v \mathbf{u}_v) \quad (3.19)$$

or equivalently written as:

$$\frac{\partial}{\partial t} (w_s h_s + w_l h_l) = -\nabla \cdot \mathbf{q} - \nabla \cdot (h_l \mathbf{g}_l + h_v \mathbf{g}_v) \quad (3.20)$$

where the enthalpy of liquid water h_l and water vapor h_v is defined as:

$$h_l = c_{p,l} (T - T_{ref}) \quad (3.21)$$

$$h_v = c_{p,v} (T - T_{ref}) + L_v \quad (3.22)$$

where L_v is the latent heat of vaporization of water. In the present study, the conservation of mass and energy is coupled together as a heat and mass model (HAM) according to ([Carmeliet 2005](#); [Defraeye 2011](#); [Janssen 2002](#); [Kubilay et al. 2018](#); [Saneinejad 2013](#)). The conservation of mass resulting in a p_c -form Richards equation is given as:

$$\frac{\partial w}{\partial p_c} \frac{\partial p_c}{\partial t} = -\nabla \cdot (\mathbf{g}_l + \mathbf{g}_v) + s_r \quad (3.23)$$

where \mathbf{g}_l and \mathbf{g}_v are the water liquid and water vapor fluxes ($\text{kg m}^{-2} \text{s}^{-1}$) and s_r is the root water uptake ($\text{kg m}^{-3} \text{s}^{-1}$) due to plant leaf transpiration. The sink term due to root water uptake is explained in detail later in Section 3.3.

The conservation of energy is written as

$$(c_{ps} w_s + c_{pl} w) \frac{\partial T}{\partial t} + \left[c_{pl} (T - T_{ref}) \frac{\partial w}{p_c} \right] \frac{\partial p_c}{\partial t} = -\nabla \cdot \left\{ \underbrace{\mathbf{q} + c_{pl} (T - T_{ref}) \mathbf{g}_l}_{\mathbf{q}_l} + \underbrace{\left[c_{pv} (T - T_{ref}) + L_v \right] \mathbf{g}_v}_{\mathbf{q}_v} \right\} \quad (3.24)$$

where \mathbf{q} (W m^{-2}) is the heat conduction given by Fourier's law as:

$$\mathbf{q} = -\lambda \nabla T \quad (3.25)$$

where T (K) is temperature, λ ($\text{W m}^{-1} \text{K}^{-1}$) is thermal conductivity. Therefore, the change in water content in the porous material is simply due to the liquid and vapor fluxes, and root water uptake. The liquid water flux in porous media is given by:

$$\mathbf{g}_l = -K_{lp} \nabla (p_c + \rho_l g z) \quad (3.26)$$

and assumes the air-pressure effects is negligible with respect to capillary and gravitational effects with K_{lp} (s) the liquid water permeability. We assume that the liquid water permeability is only

due to pressure gradient, and the influence of thermal gradient is neglected (**Carmeliet2005**). The water vapor flux in the porous media is given by:

$$\mathbf{g}_v = K_{vp} \nabla p_c + K_{vT} \nabla T \quad (3.27)$$

where

$$K_{vp} = -\delta_v \frac{p_v}{\rho_l R_v T} \quad (3.28)$$

is the water vapor permeability due to pressure (s),

$$K_{vT} = -\delta_v \frac{p_v}{\rho_l R_v T^2} (\rho_l L_v - p_c) \quad (3.29)$$

is the water vapor permeability due to temperature (s), and δ_v is the water vapor diffusion coefficient (s) (**Carmeliet2005**; Defraeye 2011; Kubilay 2014; Saneinejad 2013):

$$\delta_v = \frac{D_{va,mat}}{R_v T} \quad (3.30)$$

Thus, the heat and mass conservation in the porous media is therefore written as:

$$C_{mm} \frac{\partial p_c}{\partial t} = \nabla \cdot \left(K_{lp} \nabla (p_c + \rho_l g z) + K_{vp} \nabla p_c + K_{vT} \nabla T \right) + s_r \quad (3.31)$$

$$C_{TT} \frac{\partial T}{\partial t} + C_{Tp} \frac{\partial p_c}{\partial t} = \nabla \cdot \left(\lambda \nabla T + K_{lp} c_{pl} (T - T_{ref}) \nabla p_c + K_{lp} c_{pl} (T - T_{ref}) \rho_l g z - K_{vp} [c_{pv} (T - T_{ref}) + L_v] \nabla p_c - K_{vT} [c_{pv} (T - T_{ref}) + L_v] \nabla T \right) \quad (3.32)$$

where the capacity terms are:

$$C_{mm} = \frac{\partial w}{\partial p_c} \quad (3.33)$$

$$C_{TT} = c_{ps} w_s + c_{pl} w \quad (3.34)$$

$$C_{Tp} = c_{pl} (T - T_{ref}) \frac{\partial w}{\partial p_c} \quad (3.35)$$

3.2.4 Linearized heat and mass transport equation

In this section, the numerical approach of solving the coupled heat and mass transport for the solid material is detailed. Due to the shape of the water retention curve and the hydraulic con-

ductivity curve, the Richards equation is highly non-linear. Therefore, the numerical solution of the equation is very sensitive to convergence tolerance and requires linearization techniques to maintain accuracy and computational efficiency. Therefore, methods such as fixed-point Picard iterations is used to solve the non-linear equations. More details on the discretization is provided in Janssen (2002), Kubilay et al. (2018), and Liu (2012). The linearized form of moisture transport equation is given as:

$$\begin{aligned} C_{mm}^{n+1,k} \frac{p_c^{n+1,k+1} - p_c^n}{\Delta t} = & \nabla \cdot \left(K_{lp}^{n+1,k} \nabla \left(p_c^{n+1,k+1} + \rho_l g z \right) \right. \\ & + K_{vp}^{n+1,k} \nabla p_c^{n+1,k+1} \\ & \left. + K_{vT}^{n+1,k} \nabla T^{n+1,k} \right) \\ & + s_r^{n+1,k+1} \end{aligned} \quad (3.36)$$

where the capacity, permeabilities and temperature are determined from the previous Picard iteration (k). The subscript (n) denotes the global (i.e., outer) time step of t and k denoting the internal Picard iteration step. When the Picard solution approaches converges, $p_c^{n+1,k} \rightarrow p_c^{n+1,k+1}$ and the influence of $\partial w / \partial p_c$ becomes negligible. This can results in larger mass conservation errors and can be minimized by using mixed-form:

$$\begin{aligned} C_{mm}^{n+1,k} \frac{p_c^{n+1,k+1} - p_c^n}{\Delta t} = & \nabla \cdot \left(K_{lp}^{n+1,k} \nabla \left(p_c^{n+1,k+1} + \rho_l g z \right) \right. \\ & + K_{vp}^{n+1,k} \nabla p_c^{n+1,k+1} \\ & \left. + K_{vT}^{n+1,k} \nabla T^{n+1,k} \right) \\ & + s_r^{n+1,k+1} - \frac{w^{n+1,k+1} - w^n}{\Delta t} \end{aligned} \quad (3.37)$$

Similarly, the linearized form of the heat equation is defined as:

$$\begin{aligned} C_{TT}^{n+1,k} \frac{T^{n+1,k+1} - T^n}{\Delta t} = & \nabla \cdot \left(\lambda \nabla T^{n+1,k+1} \right. \\ & + K_{lp}^{n+1,k} c_{pl} \left(T^{n+1,k+1} - T_{ref} \right) \nabla p_c^{n+1,k+1} \\ & + K_{lp}^{n+1,k} c_{pl} \left(T^{n+1,k+1} - T_{ref} \right) \rho_l g z \\ & \left. - K_{vp}^{n+1,k} \left[c_{pv} \left(T^{n+1,k+1} - T_{ref} \right) + L_v \right] \nabla p_c^{n+1,k} \right. \\ & \left. - K_{vT}^{n+1,k} \left[c_{pv} \left(T^{n+1,k+1} - T_{ref} \right) + L_v \right] \nabla T^{n+1,k+1} \right) \end{aligned} \quad (3.38)$$

where the capillary pressure time derivative term is ignored. The mixed-form the heat equation is given as:

$$\begin{aligned}
 C_{TT}^{n+1,k} \frac{T^{n+1,k+1} - T^n}{\Delta t} = & \nabla \cdot \left(\lambda \nabla T^{n+1,k+1} \right. \\
 & + K_{lp}^{n+1,k} c_{pl} \left(T^{n+1,k+1} - T_{ref} \right) \nabla p_c^{n+1,k+1} \\
 & + K_{lp}^{n+1,k} c_{pl} \left(T^{n+1,k+1} - T_{ref} \right) \rho_l g z \\
 & - K_{vp}^{n+1,k} \left[c_{pv} \left(T^{n+1,k+1} - T_{ref} \right) + L_v \right] \nabla p_c^{n+1,k} \\
 & - K_{vT}^{n+1,k} \left[c_{pv} \left(T^{n+1,k+1} - T_{ref} \right) + L_v \right] \nabla T^{n+1,k+1} \Big) \\
 & - \frac{C_{TT}^{n+1} T^{n+1} - C_{TT}^n T^n}{\Delta t}
 \end{aligned} \tag{3.39}$$

The system of linear equations is solved by Krylov subspace iteration solver, i.e. preconditioned conjugate gradient (PCG) with diagonal-based incomplete Cholesky (DIG) preconditioning. The convergence criteria for the Picard iteration is user-defined:

$$|p_c^{n+1,k+1} - p_c^{n+1,k}| \leq \delta p_c \tag{3.40}$$

$$|T^{n+1,k+1} - T^{n+1,k}| \leq \delta T \tag{3.41}$$

where $\delta p_c = \delta T = 10^{-2}$.

3.3 SOIL-PLANT-ATMOSPHERIC CONTINUUM

In the present study, the components of the water potential inside the plants are not directly determined. The soil-plant-atmosphere continuum model that is integrated into the vegetation model is described in this section, implemented according the state-of-art techniques: (Farquhar et al. 1980; Idso 1977; Launiainen et al. 2015; Manoli et al. 2014; Manzoni et al. 2011; Volpe et al. 2013). The root-system of the plants are represented as a network-like structure assuming cooperative strategy among the individual roots and a bulk plant transpiration through a single xylem is assumed.

3.3.1 Water transport in soil-root system

The hydraulic conductivity in soil K (m s^{-1}) is given as:

$$K(\mathbf{x}) = K_{lp}(\mathbf{x}) |\mathbf{g}| \tag{3.42}$$

where K_l (s) is the liquid permeability defined in the previous section and function on the moisture content. The soil conductance in the root region k_s (s^{-1}) is:

$$k_s(\mathbf{x}) = \alpha K(\mathbf{x}) r(\mathbf{x}) \quad (3.43)$$

where α is

$$\alpha = \sqrt{\left(\frac{L}{RAI}\right) \frac{1}{d}} \quad (3.44)$$

and d is the root diameter and $RAI = \int r dz$ is the root area index ($m^2 m^{-2}$) and is the vertical integral of the root area density r ($m^2 m^{-3}$). The conductance of the root system k_r (s^{-1}) is given as:

$$k_r(\mathbf{x}) = r(\mathbf{x}) \frac{\Delta z}{\beta} \quad (3.45)$$

where Δz is the vertical height of the root layer mesh and $\beta = 3 \times 10^8$ s. The effective conductance of the soil-root system (or rhizosphere) k_{sr}^* ($s m^{-1}$) is given as:

$$k_{sr}^*(\mathbf{x}) = \frac{1}{|\mathbf{g}|} \frac{k_s(\mathbf{x}) k_r(\mathbf{x})}{k_s(\mathbf{x}) + k_r(\mathbf{x})} \quad (3.46)$$

The sink in soil moisture s_r ($kg m^{-3} s^{-1}$) is given as:

$$s_r(\mathbf{x}) = r(\mathbf{x}) g_{v,root}(\mathbf{x}) \quad (3.47)$$

where $g_{v,root}$ is the root water uptake ($kg m^{-2} s^{-1}$)

$$g_{v,root}(\mathbf{x}) = k_{sr}^*(\mathbf{x}) (\psi_s(\mathbf{x}) - \psi_R) \quad (3.48)$$

and simply dependent on the soil-root system conductance, soil water potential ψ_s and the (bulk) root water potential ψ_R . The resulting net sink is soil moisture $G_{v,root}$ ($kg s^{-1}$) due to transpiration is thus:

$$G_{v,root} = \int_{\Omega_s} r(\mathbf{x}) g_{v,root}(\mathbf{x}) dV \quad (3.49)$$

where Ω_s is the soil domain. The water uptake from the root is equal to the water transport in the xylem as so:

$$G_{v,root} = G_{v,xylem} \quad (3.50)$$

3.3.2 Water transport in xylem-leaf system

The plant xylem conductance is modeled using a “vulnerability curve” approach, where xylem conductance becomes exponentially smaller with increasing leaf water potential (Volpe et al. 2013). This empirical model is based on plant response to the vulnerability to xylem cavitation and embolism that could occur at high water potential gradients. The xylem conductance k_x ($m Pa^{-1} s^{-1}$) is given by:

$$k_x(\psi_L) = k_{x,max} \exp \left\{ - \left(-\frac{\psi_L}{d} \right)^c \right\} \quad (3.51)$$

where $k_{x,max}$ ($\text{m Pa}^{-1} \text{s}^{-1}$) is the maximum xylem conductance, c and d are fit coefficients (Volpe et al. 2013), and ψ_L (Pa) is the (bulk) leaf water potential. The effective xylem conductance k_x^* (s m^{-1}) of water is:

$$k_x^*(\psi_L) = k_x(\psi_L) \rho_l \quad (3.52)$$

Thus, the water flux through the plant in xylem $g_{v,xylem}$ ($\text{kg m}^{-2} \text{s}^{-1}$) is given as:

$$g_{v,xylem}(\psi_L) = k_x^*(\psi_R - \psi_L) \quad (3.53)$$

where is governed by the water potential gradient. The net water flux $G_{v,xylem}$ (kg s^{-1}) is given as:

$$G_{v,xylem}(\psi_L) = \int_{\partial\Omega_{x|s}} g_{v,xylem}(\psi_L) \, dA = g_{v,xylem} A_x \quad (3.54)$$

where A_x (m^2) is the xylem cross-sectional area, assuming that the net water flux through the xylem is equal (i.e. no water storage).

Similarly, the net flux of water in xylem should be equal to the net transpiration rate, as storage is negligible. Therefore,

$$G_{v,xylem} = G_{v,leaf} \quad (3.55)$$

and moreover,

$$G_{v,root} = G_{v,xylem} = G_{v,leaf} \quad (3.56)$$

3.3.3 Water transport from leaf to air

The leaf transpiration rate $g_{v,leaf}$ ($\text{kg m}^{-2} \text{s}^{-1}$) is defined in Chapter 1, and is simply defined as:

$$g_{v,leaf} = k_{st,v}^* (p_{v,leaf} - p_v) \quad (3.57)$$

where $k_{st,v}^*$ (s m^{-1}) is the effective stomatal conductance to water vapor, $p_{v,leaf}$ (Pa) is the leaf surface vapor pressure and p_v (Pa) is the atmospheric vapor pressure. The net plant transpiration rate is given as:

$$G_{v,leaf} = \int_{\Omega_a} a g_{v,leaf} \, dV \quad (3.58)$$

where a ($\text{m}^2 \text{ m}^{-3}$) is the leaf area density. The water mass flux to the atmosphere is assumed to be in equilibrium with the water vapor flux through xylem:

$$G_{v,xylem} = G_{v,leaf} \quad (3.59)$$

and so:

$$k_x^*(\psi_R - \psi_L) A_x = \int_{\Omega_a} a g_{v,leaf} \, dV \quad (3.60)$$

Therefore, the root water potential ψ_R can be determined once leaf water potential ψ_L (Pa), net plant transpiration rate $G_{v,leaf}$ (kg s^{-1}), effective xylem conductance k_x^* (s m^{-1}) and xylem cross-section area A_x (m^2):

$$\psi_R(\psi_L) = \psi_L + \frac{G_{v,leaf}}{A_x k_x^*} \quad (3.61)$$

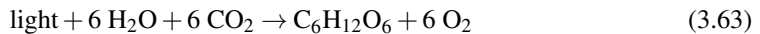
The assumption is that water extract by roots only feed the transpiration and storage inside the plant is neglected. Furthermore, one can also take in account of the gravitation potential change due to tree height:

$$\psi_R(\psi_L) = \psi_L + \frac{G_{v,leaf}}{A_x k_x^*} + \rho_l g H \quad (3.62)$$

however, with a tree height of $H = 10$ m, the additional potential is only $\psi_g = 0.1$ MPa.

3.3.4 Improved stomatal model

The photosynthetic reaction takes light, water and CO₂ and creates carbohydrate and oxygen:



and additional moisture is lost by evaporation when stomatal cavity is exposed to atmosphere. Therefore, the photosythetic process is directly related to atmospheric condition such as CO₂ concentration, availability of light and temperature. Furthermore, the transpiration rate is also dependent on the atmospheric humidity and the availability of water for transpiration (Ball 1987; Leuning et al. 1995). Based on these conditions, a generally accepted theory is the plant regulates the stomatal aperture to optimize the photosynthetic rate for a given transpiration rate. Moreover, the function of vegetation can be simplified as just maximizing the photosynthesis (or CO₂ assimilation) for a given transpiration rate (water use) (Medlyn et al. 2011). The water use efficiency or WUE quantifies the efficiency of the plant of reaching this target. The WUE is defined as:

$$WUE = \frac{f_c}{f_v} \quad (3.64)$$

where f_c (mol m⁻² s⁻¹) is the CO₂ assimilation rate (i.e., denoted also as A_n (in plant-science) or $G_{c,leaf}$ (in building physics), also known as photosynthesis rate) and f_v (mol m⁻² s⁻¹) is the transpiration rate (i.e. denoted also as f_e (in plant-science) or $G_{v,leaf}$ (in building physics), also known as water use).

The stomatal optimality model reflects the theory of the stomatal behavior (Cowan 1978). The optimal stomatal control is derived from the minimization problem described by the Lagrangian:

$$\mathcal{L}(k_{st}) = f_c - \lambda f_v \quad (3.65)$$

where λ (mol mol⁻¹) is a Lagrange multiplier and represents the marginal water cost of plant carbon gain (Katul, Manzoni, et al. 2010; Manoli et al. 2014; Medlyn et al. 2011) and $f_c = f_c(k_{st})$ and $f_v = f_v(k_{st})$ where both assimilation rate and transpiration rate are both dependent on the stomatal conductance k_{st} (mol m⁻² s⁻¹) (i.e. g_s (in plant-science) or $h_{c,m}$ (in building-physics) or $1/r_s$ where r_s is stomatal resistance). Cowan (1978) shows that optimal stomatal behaviour is at the minima of the Lagrangian:

$$\frac{\partial \mathcal{L}}{\partial k_{st}} = 0 \quad (3.66)$$

leading to the following constraint:

$$\lambda = \frac{\partial f_v}{\partial k_{st}} \frac{\partial k_{st}}{\partial f_c} \quad (3.67)$$

or simply:

$$\lambda = \frac{\partial f_v}{\partial f_c} \quad (3.68)$$

Following, these constraints, the stomatal conductance is can be determined with additional closure model for assimilation rate and transpiration rate. The assimilation rate f_c can be described from the perspective of photochemical reaction model and the Fickian diffusion model from the stomatal cavity.

The Farquhar model of photosynthesis describing the biochemical demand function is given as:

$$f_c = \frac{a_1 c_i}{a_2 + s c_a} \quad (3.69)$$

where c_i (mol mol^{-1}) is the intercellular CO_2 concentration, c_a (mol mol^{-1}) is the ambient CO_2 concentration, and a_1 and a_2 are parameters dependent on whether photosynthetic reaction rate is limited by light or Rubisco (Ribulose bisphosphate (RuBP) carboxylase-oxygenase) (Farquhar et al. 1980; Katul, Manzoni, et al. 2010) and $s = 0.7$ is the constant representing long-term intercellular to ambient CO_2 concentration ratio (Volpe et al. 2013). Note that we use a linearized model assuming $c_p \ll c_i$ where c_p is the CO_2 compensation point. As the photosynthesis can either be light-limited or Rubisco limited, the true assimilation rate f_c is given as:

$$f_c = \min(f_c^l, f_c^r) \quad (3.70)$$

where f_c^l is the light-limited assimilation rate and f_c^r is the Rubisco limited assimilation rate. Note that it is also possible to incorporate the dark (or night) respiration and in that case $f_c = \min(f_c^l, f_c^r) - r_d$, but is simplified in our study.

Light-limited

When the assimilation (or photosynthesis) rate is *light-limited*:

$$a_1(\mathbf{x}) = \alpha_p e_m Q_p = \gamma Q_p(\mathbf{x}) \quad (3.71)$$

and

$$a_2(\mathbf{x}) = 2c_p(\mathbf{x}) \quad (3.72)$$

where α_p is the leaf absorptivity of photosynthetically active radiation (PAR), e_m is the maximum quantum efficiency of the leaf, $\gamma = 0.015$ is the apparent quantum yield, Q_p ($\text{mol m}^{-2} \text{s}^{-1}$) is the flux of incoming PAR and c_p (mol mol^{-1}) is the the CO_2 compensation point with:

$$c_p(\mathbf{x}) = \frac{K_c(\mathbf{x})}{2K_o(\mathbf{x})} C_{o,a} \frac{k_o}{k_c} \quad (3.73)$$

where $k_c = 2.5 \text{ s}^{-1}$ and $k_o = 0.18k_c$ (Farquhar et al. 1980). Therefore, the light-limited assimilation rate is:

$$f_c^l(\mathbf{x}) = \frac{\gamma Q_p(\mathbf{x}) c_i(\mathbf{x})}{2c_p(\mathbf{x}) + sc_a(\mathbf{x})} \quad (3.74)$$

Rubisco-limited

If the assimilation rate is *Rubisco-limited*:

$$a_1(\mathbf{x}) = V_{cmax}(\mathbf{x}) \quad (3.75)$$

and

$$a_2(\mathbf{x}) = K_c(\mathbf{x}) \left(1 + \frac{C_{o,a}}{K_o(\mathbf{x})} \right) \quad (3.76)$$

where $V_{c,max}$ is the maximum carboxylation capacity (referenced at 25 °C), K_c and K_o are Michaelis constant for CO₂ and O₂ inhibition (referenced at 25 °C), and $C_{o,a} = 0.21 \text{ mol mol}^{-1}$ is the oxygen concentration in the atmosphere. The maximum carboxylation capacity is given as:

$$V_{cmax}(\mathbf{x}) = V_{cmax,25} \frac{\exp\{0.088(T_l(\mathbf{x}) - 298.15)\}}{1 + \exp\{0.29(T_l(\mathbf{x}) - 314.15)\}} \quad (3.77)$$

and K_c and K_o are

$$K_c(\mathbf{x}) = K_{c,25} \exp\{\gamma_c(T_l(\mathbf{x}) - 298.15)\} \quad (3.78)$$

$$K_o(\mathbf{x}) = K_{o,25} \exp\{\gamma_o(T_l(\mathbf{x}) - 298.15)\} \quad (3.79)$$

where T_l (K) is the leaf temperature, $V_{cmax,25} = 5.9 \times 10^{-5} \text{ mol m}^{-2} \text{ s}^{-1}$, $\gamma_c = 0.074$, $\gamma_o = 0.015$, $K_{c,25} = 3 \times 10^{-3} \text{ mol mol}^{-1}$ and $K_{o,25} = 0.3 \text{ mol mol}^{-1}$. Therefore, the Rubisco-limited assimilation rate is:

$$f_c^r(\mathbf{x}) = \frac{V_{cmax}(\mathbf{x}) c_i}{K_c(\mathbf{x}) \left(1 + \frac{C_{o,a}}{K_o(\mathbf{x})} \right) + sc_a(\mathbf{x})} \quad (3.80)$$

The Fickian diffusion through stomata is given as:

$$f_c = k_{st}(c_a - c_i) \quad (3.81)$$

$$f_v = k_{st,v} \left(\frac{p_{v,i} - p_v}{p} \right) \quad (3.82)$$

where $k_{st,v}$ (mol m⁻² s⁻¹) is the stomatal conductance to water vapor:

$$k_{st,v} = a_c k_{st} \quad (3.83)$$

where $a_c = 1.6$ is the relative diffusion of water vapor to CO₂. Furthermore, $p_{v,i} = p_{v,sat}(T_l)$ (Pa) is the intercellular vapor pressure inside the stomatal cavity assumed to be at saturation at the leaf temperature T_l . Thus, equating Fickian CO₂ flux to the Farquhar biochemical demand, we have:

$$f_c = \frac{a_1 c_i}{a_2 + sc_a} = k_{st} (c_a - c_i) \quad (3.84)$$

where c_i is the unknown. Rewriting, we get:

$$c_i = c_a \frac{a_2 + sc_a}{a_1/k_{st} + a_2 + sc_a} \quad (3.85)$$

and substituting c_i into the biochemical demand function, the assimilation rate is a closed-problem as:

$$f_c = \frac{k_{st} a_1 c_a}{a_1 + k_{st} (a_2 + sc_a)} \quad (3.86)$$

Thus, the stomatal conductance can be finally obtained from the minimizing the problem:

$$\frac{\partial \mathcal{L}}{\partial k_{st}} = \frac{\partial f_c}{\partial k_{st}} - \lambda \frac{\partial f_v}{\partial k_{st}} = 0 \quad (3.87)$$

which becomes:

$$\frac{\partial}{\partial k_{st}} \left[\left(\frac{k_{st} a_1 c_a}{a_1 + k_{st} (a_2 + sc_a)} \right) - \lambda a_c k_{st} VPD \right] = 0 \quad (3.88)$$

where $VPD = (p_{v,i} - p_v) / p$ (mol mol⁻¹). The derivative becomes:

$$\frac{a_1^2 c_a}{[a_1 + k_{st} (a_2 + sc_a)]^2} - \lambda a_c VPD = 0 \quad (3.89)$$

Therefore, solving for k_{st} we obtain:

$$k_{st}(\mathbf{x}) = \frac{a_1(\mathbf{x})}{a_2(\mathbf{x}) + sc_a(\mathbf{x})} \left(-1 + \sqrt{\frac{c_a(\mathbf{x})}{a_c \lambda(\psi_l) VPD(\mathbf{x})}} \right) \quad (3.90)$$

where the marginal water use is empirically related to the leaf water potential $\lambda = \lambda(\psi_l)$ (Katul, Manzoni, et al. 2010; Manoli et al. 2014). Therefore, the stomatal response change to water availability is reflected through the change in leaf water potential ψ_l . Additionally, in literature it is known that stomata does not completely close during night allowing for respiration. Therefore, taking this into account:

$$k_{st}(\mathbf{x}) = \frac{a_1(\mathbf{x})}{a_2(\mathbf{x}) + sc_a(\mathbf{x})} \left(-1 + \sqrt{\frac{c_a(\mathbf{x})}{a_c \lambda(\psi_l) VPD(\mathbf{x})}} \right) + k_{st,n} \quad (3.91)$$

where $k_{st,n}$ ($\text{mol m}^{-2} \text{s}^{-1}$) is the nocturnal stomatal conductance ($k_{st,n} = 0.018 \text{ mol m}^{-2} \text{s}^{-1}$ (Manoli et al. 2014)). The intercellular CO₂ concentration simplifies to:

$$c_i = c_a \left(1 - \sqrt{\frac{a\lambda VPD}{c_a}} \right) \quad (3.92)$$

and thus closing the (with the exception of λ) the photosynthetic rate. So far, the stomatal conductance model is derived by neglecting the contribution of boundary layer conductance k_b (i.e. g_b (in plant-science), or inverse of boundary layer resistance r_b , assumed to be equivalent to aerodynamic resistance r_a). Therefore, the effective stomatal condutance k_{st}^* is defined as:

$$k_{st}^* = \frac{k_{st} k_b}{k_{st} + k_b} \quad (3.93)$$

assuming the resistance are in series. Therefore, the plant fluxes into atmosphere become:

$$f_c = k_{st}^* f_c \quad (3.94)$$

$$f_v = k_{st,v}^* f_v \quad (3.95)$$

Furthermore, the fluxes in units $\text{kg m}^{-2} \text{s}^{-1}$ can be simply determined as:

$$g_{c,leaf} = M_c f_c \quad (3.96)$$

$$g_{v,leaf} = M_v f_v \quad (3.97)$$

where $M_c = 4.401 \times 10^{-2} \text{ kg mol}^{-1}$ and $M_v = 1.8015 \times 10^{-2} \text{ kg mol}^{-1}$ are the molar mass of CO₂ and water vapor, respectively.

3.3.5 Marginal water use

The marginal water use efficiency (WUE) λ or the cost-parameter for the cost of water lost from leaves. The marginal WUE should change over time depending on the water availability Manzoni et al. (2011). The marginal WUE is estimated from photosynthesis, transpiration and stomatal conductance measurement, obtained simply from the gradient of WUE:

$$WUE = \frac{f_c}{f_v} \quad (3.98)$$

The observations derive a marginal WUE as a function of leaf water potential ψ_L :

$$\lambda(\psi_L) = \lambda_{max}^* \frac{c_a}{c_a^*} \exp \left\{ -\beta \left(\langle \psi_L \rangle_{24h} - \psi_{L,max} \right)^2 \right\} \quad (3.99)$$

where ψ_L is assumed to vary slowly such that $\langle \psi_L \rangle_{24h}$ is fixed within the secant iteration, λ_{max}^* is the marginal WUE under well-watered soil condition at reference CO₂ concentration $c_a^* = 400$

$\mu\text{mol mol}^{-1}$ or parts-per-million (ppm), β is the plant-specific sensitivity parameter (Huang et al. 2017).

3.3.6 Numerical method for determining leaf water potential

The water transport through the plant from soil to root, from root to xylem, through the xylem, and finally, from leaf stomata to air is a closed-problem once the leaf water potential is known. The leaf water potential is determined from the following constraint:

$$G_{v,leaf}(\psi_L) = G_{v,root}(\psi_L) \quad (3.100)$$

or as an optimization problem, it is defined as:

$$\arg \min_{\psi_L} \mathcal{G}(\psi_L) = |G_{v,leaf} - G_{v,root}| \quad (3.101)$$

As this is a non-linear closure problem (Manoli et al. 2014), a secant method is employed to iteratively converge to the leaf water potential. The $j + 1^{\text{th}}$ leaf water potential estimate is determined as:

$$\psi_L^{j+1} = \psi_L^j - G(\psi_L^j) \frac{\psi_L^j - \psi_L^{j-1}}{G(\psi_L^j) - G(\psi_L^{j-1})} \quad (3.102)$$

where the initial estimate of $\psi_L^{j=0} = 0 \text{ MPa}$ and $\psi_L^{j=1} = -10 \text{ MPa}$ and with the additional constraint that $-10 \leq \psi_L \leq 0 \text{ MPa}$, enforcing that leaf water potential is negative and not larger than -10 MPa (typically known to lower). The detailed solution strategy for determining for coupling all the models is detailed in next section.

3.3.7 Solution strategy for coupling

The numerical model for air domain, solid domains (soil, ground, building), the radiation model and the vegetation model is implemented into OpenFOAM. The solid and air domains are coupled at regular intervals t^m defined as exchange timesteps or air time steps (Kubilay et al. 2018; Saneinejad et al. 2014). The fluxes between air and solid domain consisting for thermal, moisture and radiative transfers are coupled at this step, chosen to be 10 min. At each t^m , the air domain is assumed to the quasi-steady and solving using steady-state RANS approach converged when residuals of $\rho, \mathbf{u}, h, k, \epsilon$ are below threshold. During the steady-state computation, the leaf energy balance is evaluated periodically to correct the heat and mass fluxes, $q_{sen,leaf}$ and $g_{v,leaf}$, respectively.

The algorithm of the air domain $t^m \rightarrow t^{m+1}$ with Δt^m the air domain pseudo-timesteps of 10 min, is as follows:

1. Update the radiation fields in the air domain using q_{rad} from building surfaces and determined q_{rlw} and q_{rsw} .
2. Solve the energy balance at the leaf surface:

- a) Determine the radiative flux $q_{rad,leaf}$ using Eq. (1.50).
 - b) Calculate the stomatal and aerodynamic resistances r_a and r_s using Eq. (1.38) and Eq. (1.43), respectively. Note that $r_s = (k_{st,v})^{-1}$ and $\lambda(\psi_L)$ is constant. Therefore, r_s is only dependent on assimilation rate f_c , and the VPD.
 - c) Perform an initial estimate of leaf temperature $T_{leaf} = T$.
 - d) Calculate the saturated vapor pressure at the leaf surface $p_{vsat,leaf} = f(T_{leaf})$.
 - e) Calculate the latent heat flux $q_{lat,leaf}$ using Eq. (1.39).
 - f) Correct the leaf temperature T_{leaf} using Eq. (1.46).
 - g) Repeat steps (d) to (f) until the leaf temperature has converged with a convergence criterion of 10^{-8} .
3. Calculate all vegetation source terms s_ρ , s_u , s_T , s_w , s_k and s_e using Eqs. Eqs. (1.30) to (1.35).
 4. Solve for the steady-state flow field for t^{m+1} , Eqs. (1.21) to (1.26).
 5. Repeat steps (2) to (4) until residuals of Eqs. (1.21) to (1.26) have reached the convergence limit of 10^{-8} , $\delta f^{m+1} \leq \varepsilon$

For every m exchange timesteps, the solid domains are solved using a transient approach with n adaptive solid timesteps (Janssen 2002; Kubilay et al. 2018). The solution from the air domain consisting of thermal and moisture fluxes are taken as boundary conditions for the solid domain equations. For each internal n iterations, the thermal and radiative fluxes from solid domain are corrected until converges. For each of n solid timesteps, the linearized heat and mass transport equation are solved using k Picard iterations. Finally, for each k Picard iteration, the root water uptake is determined through j secant iterations minimizing the cost function \mathcal{G} .

The algorithm of the solid domain $t^m \leq t^n \leq t^{m+1}$, for $n \in 0, \dots, N$ with $t^{n=0} = t^m$ and $t^N = t^{m+1}$ such that $\Delta t^n < \Delta t^m$, is as follows:

1. Solve the linearized heat and mass transport transport equation using k Picard iteration such that $t^n \leq t^{n,k} \leq t^{n+1}$ with $k \in \{0, \dots, K\}$ where $t^{n,k=0} = t^n$ and $t^{n,k=K} = t^{n+1}$.
 - (a) Determine marginal WUE $\lambda(\langle \psi_L \rangle_{24h})$. As ψ_L is assumed to be slowly varying, λ is constant in secant iteration.
 - (b) Determine the stomatal conductance k_{st} , constant in the secant iteration.
 - (c) Determine the assimilation rate f_c and transpiration rate f_v , constant in the secant iteration.
 - (d) Determine the net transpiration rate $G_{v,leaf}$.
 - (e) Determine the effective soil-root conductance k_{sr}^* , constant in the secant iteration.
 - (f) Solve for leaf water potential $\psi_L^{n,k}$ of the k^{th} Picard iteration using $j \in \{0, \dots, J\}$ secant iterations.
 - (a) Initial guess of leaf water potential, $\psi_L^{j=0} = 0 \text{ MPa}$, $\psi_L^{j=1} = -10 \text{ MPa}$.
 - (b) Calculate the effective xylem conductance k_x^* .

- (c) Calculate root water potential ψ_R^j .
 - (d) Calculate the root uptake $g_{v,root}$ and the net root uptake $G_{v,root}$.
 - (e) Determine the cost function \mathcal{G} .
 - (f) Correct the leaf water potential using secant method $\psi_L^j \rightarrow \psi_L^{j+1}$.
 - (g) Repeat till leaf water potential converged, $\delta\psi_L \leq \varepsilon$.
 - (g) Calculate the sink in soil moisture due to root water uptake s_r .
 - (h) Solve linearized form of heat and mass equation using PCG until $\delta p_c = \delta T = 10^{-2}$, repeating steps before.
2. Use the final surface temperature T_s^N to update the radiation model updating $q_{r,lw}$ fluxes from all surfaces.
3. Final surface temperature T_s^N and moisture fluxes g_v^N are boundary condition for the air domain for $t^m \rightarrow t^{m+1}$.

BIBLIOGRAPHY

- Fatnassi, H., T. Boulard, C. Poncet, and M. Chave (2006). "Optimisation of greenhouse insect screening with computational fluid dynamics." In: *Biosyst. Eng.* 93.3, pp. 301–312.
- Fiala, D., K. J. Lomas, and M. Stohrer (2001). "Computer prediction of human thermoregulatory and temperature responses to a wide range of environmental conditions." In: *Int J Biometeorol* 45.3, pp. 143–159.
- Franke, J., A. Hellsten, H. Schluenzen, and B. Carissimo (2007). *Best practice guideline for the CFD simulation of flows in the urban environment: COST action 732 quality assurance and improvement of microscale meteorological models*. July 2016.
- Gorlé, C., C. Garcia-Sánchez, and G. Iaccarino (Sept. 2015). "Quantifying inflow and RANS turbulence model form uncertainties for wind engineering flows." In: *J. Wind Eng. Ind. Aerodyn.* 144.2015, pp. 202–212.
- Gromke, C. (2011). "A vegetation modeling concept for building and environmental aerodynamics wind tunnel tests and its application in pollutant dispersion studies." In: *Environ. Pollut.* 159.8-9, pp. 2094–2099.
- Hiraoka, H. (2005). "An investigation of the effect of environmental factors on the budgets of heat, water vapor, and carbon dioxide within a tree." In: *Energy* 30.2-4 SPEC. ISS. Pp. 281–298.
- Huang, C.-W., J.-C. Domec, E. J. Ward, T. Duman, G. Manoli, A. J. Parolari, and G. G. Katul (2017). "The effect of plant water storage on water fluxes within the coupled soil-plant system." In: *New Phytol.* 213.3, pp. 1093–1106.
- Idso, S. B. (1977). *An Introduction to Environmental Biophysics*. Vol. 6. 4, p. 474.
- Janssen, H. (2002). *The influence of soil moisture transfer on building heat loss via the ground*. Vol. 39. 7, pp. 825–836.
- Jendritzky, G., R. de Dear, and G. Havenith (2012). "UTCI-Why another thermal index?" In: *Int. J. Biometeorol.* 56.3, pp. 421–428.
- Judd, M., M. Raupach, and J. Finnigan (1996). "A wind tunnel study of turbulent flow around single and multiple windbreaks, part I: velocity fields." In: *Boundary-Layer Meteorol.* 1974, pp. 127–165.
- Katul, G. G., L. Mahrt, D. Poggi, and C. Sanz (2004). "One- and two-equation models for canopy turbulence." In: *Boundary-Layer Meteorol.* 113.1, pp. 81–109.
- Katul, G., S. Manzoni, S. Palmroth, and R. Oren (Mar. 2010). "A stomatal optimization theory to describe the effects of atmospheric CO₂ on leaf photosynthesis and transpiration." In: *Ann. Bot.* 105.3, pp. 431–442.
- Kenjereš, S. and B. Ter Kuile (2013). "Modelling and simulations of turbulent flows in urban areas with vegetation." In: *J. Wind Eng. Ind. Aerodyn.* 123.PA, pp. 43–55.
- Kichah, A., P. E. Bourret, C. Migeon, and T. Boulard (2012). "Measurement and CFD simulation of microclimate characteristics and transpiration of an Impatiens pot plant crop in a greenhouse." In: *Biosyst. Eng.* 112.1, pp. 22–34.
- Kubilay, A., D. Derome, and J. Carmeliet (June 2018). "Coupling of physical phenomena in urban microclimate: A model integrating air flow, wind-driven rain, radiation and transport in building materials." In: *Urban Clim.* 24, pp. 398–418.
- Kubilay, A. (2014). "Numerical simulations and field experiments of wetting of building facades due to wind-driven rain in urban areas." PhD thesis, p. 319.

- Kurn, D. M., S. E. Bretz, B. Huang, and H. Akbari (1994). “The Potential for Reducing Air Temperature and Energy Consumption Through Vegetative Cooling.” In: *Energy Environ.*
- Launiainen, S., G. G. Katul, A. Lauren, and P. Kolari (2015). “Coupling boreal forest CO₂, H₂O and energy flows by a vertically structured forest canopy – Soil model with separate bryophyte layer.” In: *Ecol. Model.* 312, pp. 385–405.
- Letts, M. G., J. Rodríguez-Calcerrada, V. Rolo, and S. Rambal (Apr. 2012). “Long-term physiological and morphological acclimation by the evergreen shrub *Buxus sempervirens* L. to understory and canopy gap light intensities.” In: *Trees* 26.2, pp. 479–491.
- Leuning, R., F. M. Kelliher, D. G. G. de Pury, and E. D. Schulze (1995). “Leaf nitrogen, photosynthesis, conductance and transpiration: Scaling from leaves to canopies.” In: *Plant, Cell Environ.* 18.10, pp. 1183–1200.
- Leuzinger, S. and C. Körner (2007). “Tree species diversity affects canopy leaf temperatures in a mature temperate forest.” In: *Agric. For. Meteorol.* 146.1-2, pp. 29–37.
- Leuzinger, S., R. Vogt, and C. Körner (2010). “Tree surface temperature in an urban environment.” In: *Agric. For. Meteorol.* 150.1, pp. 56–62.
- Li, Z., J. D. Lin, and D. R. Miller (1990). “Air flow over and through a forest edge: A steady-state numerical simulation.” In: *Boundary-Layer Meteorol.* 51.1-2, pp. 179–197.
- Liang, L., L. Xiaofeng, L. Borong, and Z. Yingxin (2006). “Improved k-ε two-equation turbulence model for canopy flow.” In: *Atmos. Environ.* 40.4, pp. 762–770.
- Liu, J., J. M. Chen, T. a. Black, and M. D. Novak (1996). “E-ε modelling of turbulent air flow downwind of a model forest edge.” In: *Boundary-Layer Meteorol.* 77.1, pp. 21–44.
- Liu, X. (2012). “suGWFoam : An Open Source Saturated-Unsaturated GroundWater Flow Solver based on OpenFOAM.” In: *Report* 01, pp. 1–54.
- Lucor, D., J. Meyers, and P. Sagaut (2007). “Sensitivity analysis of large-eddy simulations to subgrid-scale-model parametric uncertainty using polynomial chaos.” In: *J. Fluid Mech.* 585, pp. 255–279.
- Majdoubi, H., T. Boulard, H. Fatnassi, and L. Bouirden (2009). “Airflow and microclimate patterns in a one-hectare Canary type greenhouse: An experimental and CFD assisted study.” In: *Agric. For. Meteorol.* 149.6, pp. 1050–1062.
- Manickathan, L., T. Defraeye, J. Allegrini, D. Derome, and J. Carmeliet (2018). “Parametric study of the influence of environmental factors and tree properties on the transpirative cooling effect of trees.” In: *Agric. For. Meteorol.* 248, pp. 259–274.
- Manoli, G., S. Bonetti, J. C. Domec, M. Putti, G. Katul, and M. Marani (2014). “Tree root systems competing for soil moisture in a 3D soil-plant model.” In: *Adv. Water Resour.* 66, pp. 32–42.
- Manzoni, S., G. Vico, G. Katul, P. A. Fay, W. Polley, S. Palmroth, and A. Porporato (2011). “Optimizing stomatal conductance for maximum carbon gain under water stress: A meta-analysis across plant functional types and climates.” In: *Funct. Ecol.* 25.3, pp. 456–467.
- Margheri, L., M. Meldi, M. V. Salvetti, and P. Sagaut (2014). “Epistemic uncertainties in RANS model free coefficients.” In: *Comput. Fluids* 102, pp. 315–335.
- Marshall, B. Y. J. M. (1987). “Glossary of terms for thermal physiology.” In: *Pflugers Arch. Eur. J. Physiol.* 410.6, pp. 567–587.
- Medlyn, B. E., R. A. Duursma, D. Eamus, D. S. Ellsworth, I. C. Prentice, C. V. Barton, K. Y. Crous, P. De Angelis, M. Freeman, and L. Wingate (2011). “Reconciling the optimal and em-

- pirical approaches to modelling stomatal conductance.” In: *Glob. Chang. Biol.* 17.6, pp. 2134–2144.
- Najm, H. N. (2009). “Uncertainty Quantification and Polynomial Chaos Techniques in Computational Fluid Dynamics.” In: *Annu. Rev. Fluid Mech.* 41.1, pp. 35–52.
- Nobel, P. S. (2009). *Physicochemical and Environmental Plant Physiology*. Elsevier Science.
- Oke, T. R., G. Mills, A. Christen, and J. A. Voogt (2017). *Urban Climates*. Cambridge: Cambridge University Press.
- Richards, P. and R. Hoxey (1993). “Appropriate boundary conditions for computational wind engineering models using the k- ϵ turbulence model.” In: *J. Wind Eng. Ind. Aerodyn.* 46-47, pp. 145–153.
- Robitu, M., M. Musy, C. Inard, and D. Groleau (Apr. 2006). “Modeling the influence of vegetation and water pond on urban microclimate.” In: *Sol. Energy* 80.4, pp. 435–447.
- Rodriguez-Calcerrada, J., M. G. Letts, V. Rolo, S. Roset, and S. Rambal (2013). “Multiyear impacts of partial throughfall exclusion on *Buxus sempervirens* in a Mediterranean forest.” In: *For. Syst.* 22.2, pp. 202–213.
- Saneinejad, S. (2013). “The influence of evaporative cooling on the micro-climate and thermal comfort in a street canyon.” PhD thesis, p. 201.
- Saneinejad, S., P. Moonen, and J. Carmeliet (2014). “Coupled CFD, radiation and porous media model for evaluating the micro-climate in an urban environment.” In: *J. Wind Eng. Ind. Aerodyn.* 128, pp. 1–11.
- Santiago, J. L., F. Martín, a. Cuerva, N. Bezdenejnykh, and A. Sanz-Andrés (2007). “Experimental and numerical study of wind flow behind windbreaks.” In: *Atmos. Environ.* 41.30, pp. 6406–6420.
- Sanz, C. (2003). “A note on k- ϵ modeling of vegetation canopy air-flows.” In: *Boundary-Layer Meteorol.* 108.1992, pp. 191–197.
- Shih, T.-H., W. W. Liou, A. Shabbir, Z. Yang, and J. Zhu (1995). “A new k- ϵ eddy viscosity model for high reynolds number turbulent flows.” In: *Comput. Fluids* 24.3, pp. 227–238.
- Taha, H. (1997). “Urban climates and heat islands: albedo, evapotranspiration, and anthropogenic heat.” In: *Energy Build.* 25.2, pp. 99–103. arXiv: [LBL-38251PreprintERNEST](#).
- Tominaga, Y., A. Mochida, R. Yoshie, H. Kataoka, T. Nozu, M. Yoshikawa, and T. Shirasawa (2008). “AIJ guidelines for practical applications of CFD to pedestrian wind environment around buildings.” In: *J. Wind Eng. Ind. Aerodyn.* 96.10-11, pp. 1749–1761.
- Vogel, S. (1989). “Drag and reconfiguration of broadleaves in high winds.” In: *J. Exp. Bot.* 40.217, pp. 941–948.
- Volpe, V., M. Marani, J. D. Albertson, and G. Katul (2013). “Root controls on water redistribution and carbon uptake in the soil-plant system under current and future climate.” In: *Adv. Water Resour.* 60, pp. 110–120.
- Weller, H. G., G. Tabor, H. Jasak, and C. Fureby (1998). “A tensorial approach to computational continuum mechanics using object-oriented techniques.” In: *Comput. Phys.* 12.6, p. 620.
- Wilson, R. and R. Shaw (1977). “A Higher Order Closure Model for Canopy Flow.” In: *J. Appl. Meteorol.* 16.11, pp. 1197–1205.
- Wong, N. H., Y. Chen, C. L. Ong, and A. Sia (2003). “Investigation of thermal benefits of rooftop garden in the tropical environment.” In: *Build. Environ.* 38.2, pp. 261–270.

COLOPHON

This document was typeset in \LaTeX using the typographical look-and-feel `classicthesis`. The bibliography is typeset using `biblatex` with `natbib`.